UNDERSTANDING AND CONTROLLING BEHAVIOR OF POLYMERS IN POROUS MEDIA

Tian Ren

A DISSERTATION

in
Chemical and Biomolecular Engineering

Presented to the Faculties of the University of Pennsylvania

In

Partial Fulfillment of the Requirements for the

Degree of Doctor of Philosophy

2023

Supervisor of Dissertation
Dr. Daeyeon Lee, Dr. Raymond J. Gorte
Professor, Chemical and Biomolecular Engineering

Graduate Group Chairperson
Dr. John C. Crocker
Professor, Chemical and Biomolecular Engineering

Dissertation Committee
Dr. John M. Vohs (committee chair), Carl V.S. Patterson Professor, Chemical and Biomolecular Engineering
Dr. Daeyeon Lee, Russell Pearce and Elizabeth Crimian Heuer Professor, Chemical and Biomolecular Engineering
Dr. Raymond J. Gorte, Russell Pearce and Elizabeth Crimian Heuer Professor Emeritus, Chemical and Biomolecular Engineering
Dr. Karen I. Winey, Harold Pender Professor of Engineering and Applied Science, Materials Science and Engineering

UNDERSTANDING AND CONTROLLING BEHAVIOR OF POLYMERS IN POROUS MEDIA

COPYRIGHT

2023

Tian Ren

ACKNOWLEDGMENTS

First, I particularly extend my greatest gratitude to my both advisors, Dr. Daeyeon Lee and Dr. Raymond J. Gorte as my academic babysitters for mentoring me up to be a good researcher in the fast 5.5 years. I was first luckily to become the first and the last joint student in both labs, bridging the polymer world and the catalysis world because I helped to close Ray's lab after his retirement. I was firstly advised by Daeyeon and then become coadvised with Ray at my 2nd year. I especially thanks for Daeyeon's patience and Ray's carefulness, which benefit me forever throughout my life.

I am also deeply grateful to all my thesis committee members, Dr. John M. Vohs (committee chair), Dr. Karen I. Winey and my advisors, Dr. Daeyeon Lee and Dr. Raymond J. Gorte for giving me that chance to complete the thesis and oral dissertation and accomplish my PhD. John's positive attitude towards anything and Karen's careful spirit impress me a lot.

I also thank for all the wonderful advice and comments from Dr. Daeyeon Lee's Lab and Dr. Raymond. J. Gorte's Lab. I get support a lot from all our Lee families and I especially thank Coach Dr Tiancheng Arthur Wang, GAPSA-ex-President Joe Rummaneethorn (Renfa Huang), Dr. Yijiang Mu, Dr Bharath Venkatesh. Dr. Yiwei Qiang, Dr. Jinpei Huang, Dr Joseph Rosenfeild, Kaiwen Wang, Dr. Zhuo Chen, CaRI-Godmother Dr. Jyo Lyn Hor, Dr. Hong-Huy Tran, Dr. Jaehyun Kim, Dr. Siwon Lee, Dr. Wilfredo Mendez Ortiz, Anirban Majumder, CK

Yeh, Shizhao Lu, Yuxuan Dai, Dr. Hyejoong Jeong, Dr. Min Jun Oh, Dr. Baekmin Q. Kim, Dr. Katie Rose, Dr. Neha Manohar, Dr. Jiyu Li, Dr. Sean Choe, Dr. Yitian Zhou, Dr. Minchul Sung, Dr. Sagar Yadavali, Dr. Zhe Gong, Dr. Zhiwei Liao, Hoang Dinh, Jiwon Kim, Minjeong Kim, Dr. Uiseok Hwang, Dr. Joao Victor Mattioni, Magic-painter Siddharth Sharma, Dr, Taeyoung Heo, Sohyun Kim, Dr. Jingyu Wu, Prof Jonghoon Choi, Lilia Escobedo, Anatasia Neuman, Trevor Devine, Dr Jaekyoung Kim, Dr. Seyeon Park, Dr. Yoon-Ho Hwang, Dr. Woojin Jung, Jessica O' Callaghan, Emery Hsu, Stuti Dureja, Dr. Fuquan Tu, Ryan Tu, Dr. Jisung Park, Dr. Sunghee Lee, and Danielle Sclafani. And I would like to thank for the help from Ray and John's lab and specially thanks to Dr Jian Chang, Dr. Renjing Huang, future-Nobel-Prize-winner Kai Shen, Mengjie Fan, Ching-Yu Wang, Zhuoming Feng, Dr. Julian Paige, and Dr. Tianyu Cao.

I should also thank for all the collaborations who help me a lot and extend my skill levels. Thanks for the kind support and help from Dr. Zhenting Xiang, Dr. (soon be Prof.) Yuan Liu, Dr. Ranhui Xi, Dr. Beibei Gao, and Dr. Zhongshu Ren in Penn Dental School. Thanks, Dr. Jiahao Zhang in Prof. Andrew Rappe's lab for carrying me in many ways. Thank Dr. Chien-Hua Tu in Prof Karen I. Winey Group for helping me construct the viscosity models. I have learned a lot from Chien-Hua, and I believe we both will become great researchers someday. Thank Weiwei Kong in Prof Russell Composto Group for conducting SAXS and WAXS experiments for me. Weiwei is a kind and nice friend, and I am looking forward to her early graduation due to her excellent work on science and our collaboration on our business in the future. Thank Zhe Liu,

Ruiqi Dong, Dr. Yang Zhao from Prof. Osuji Chinedum Lab. Zhe and Ruiqi is my most closet same-year cohort while Yang always stayed up late with me for lab work. Thank Jacky Qixing Zhang and Zhijian Zhou in Prof. Kathleen Stebe lab. Thank Dongqi Zhao in Prof. Rob Riggleman's lab for carrying me to meet more friends who can potentially give fundings to our business.

I want to thank all my friends nearby, some of whom has been working and studying in other places. There are so many people to thank to. Thank Yixing Cao, Junhan Chen, and Muyang Zhang for carrying me a lot, who takes me to experience American traditional Kungfu: self-defense practice. Thank Anyuan Ji, Shuqing Jiang, Zhile Yu, Yuming Gu, Yinda Zhang, Litao Yan, Tao Luo, Li Yuan, Peihao Luo, Ke Wang and many other friends for enjoying good time together in my heart forever.

I also appreciated all the resources provided by the Department of Chemical and Biomolecular Engineering (CBE) in University of Pennsylvania (UPenn) and all the other abundant support from UPenn. After 5.5 years, I have deeply fall in love with our school.

I would like to thank for the support from the Center for Plastics Innovation (CPI) center in UDel. The joint collaborations have broadened my insight into polymer upcycling. I have learned a lot from all the researchers and thanks Dr. Zachary Hinton for HT-GPT experiments, thanks Prof. Thomas Epps, III and Prof. LaShanda Korley for supporting our experiments, and

thanks Dr. Shawn Najmi for exploring the QCM together. Thanks Dr. Yinan Xu and Dr. Chuting Deng for the simulation collaboration on DFT and MD from Juan de Pablo Group in UChicago.

I would like to thank all the chairs at Catalysis Club of Philadelphia (CCPhilly). As an arrangement chair in 2022, I have learned a lot when communicating with hotel, professors, managers, and research scientists in industry. Thank Udayshankar Singh, Thomas Yeh, Angela Zheng, Steve Hardwick, Prof. Weijian Diao, Leo DeRita, Donghua Zuo, Donna Liu, Dang Nguyen, and Michael Smith for helping me a lot and impressing me with a big catalysis world.

I would like to thank all the chairs at Tsinghua University Alumni Association of Great Philadelphia (THAAGP). As a vice president, I have made many friends from Tsinghua University and other universities when organizing the activities. Thank Gang Ren, Ran Chen, Wenchao Qian, Shuning Ge, Weidong Zhou, Yu Zhang, Zhiping Zhang, Shuming Zhang, Xiaoan Li, and Yulai Weng for having fun together.

My most thanked persons are my parents, Changzhong Ren and Chunli Wu, and my grandmother, Guizhi Xu. I haven't been back home to China because of the difficulties in visa renewal to USA. However, they continuously believe me and support me. I miss all my families and hope I can return some day in my postdoc life. Here I should also thank Dr. Xianbin Yang and Dr. Aoyi Luo for helping me when interviewing professors. I would like to thank Prof. Rong

Yang from Cornell University and Prof. Jingguang Chen from Columbia University who helps me so much in that process.

I would like to specially thank my postdoc advisor, Prof. Matteo Cargnello from Stanford University for offering me a chance to study and improve myself in the following year. I will work hard and try me best to enhance myself comprehensively to become a more and more qualified researcher when exploring the catalysis world.

The ChatGPT 4.0 from *OpenAI Inc*. is greatly appreciated for its help in revision and outlining. The continuously enhanced Large Language Model of Artificial Intelligence has greatly improved our working efficiency. I am dedicated to utilizing this powerful tool to enhance my knowledge and skills but remain in control of its use only for my personal and professional growth. One of my ambitions is to integrating AI technology into wet lab to create a 'LabGPT'—a more automated, AI-enhanced laboratory system, and to revolutionize how wet research is maintained currently in wet lab, which I call it as “Dewetting Revolution”.

In my life, I aim to develop myself well into an academic professor. I will continuously work hard to pursue it in my next postdoc period. Besides, my broader ambition is to promote a more peaceful and prosperous world from the aspect of science and engineering.

ABSTRACT

UNDERSTANDING AND CONTROLLING BEHAVIOR OF POLYMERS IN POROUS MEDIA

Tian Ren

Daeyeon Lee

Raymond Gorte

Despite key advances in demonstrating the feasibility of catalytic conversion of plastic wastes into high value-added chemicals, fundamental understanding on the interactions of polymers and catalytic materials is currently lacking. To enable highly efficient catalytic processes, it is critical to understand and engineer polymer-porous solid interactions. This thesis addresses this knowledge gap. There has not been a general approach to characterize polymer-solid interfacial properties quantitively. Although contact angle measurement is a powerful technique to quantify the polymer-surface interactions, the traditional sessile droplet method for a normal liquid cannot be easily applied to polymers. In our research, capillary rise infiltration of polymer into nanoparticle packing is used to study the polymer dynamics and polymer-solid interactions. We measure the rates for capillary infiltration of polymer, such as polystyrene (PS) and polyethylene (PE), into disordered packings of silica nanoparticles that are modified by atomic layer deposition (ALD) with sub-monolayer and monolayer coverages of TiO_2, WO_3, and $CaCO_3$.

Infiltration times depend strongly on the size and surface composition of nanoparticles. The confined infiltration rates measured as a function of surface-chemistry composition are used to calculate contact angles and interfacial energies for PS and PE via the Lucas-Washburn model. To understand the effect of composition, we perform microcalorimetry measurements with n-hexane and benzene on ALD-modified SBA-15. Our results have shown a strong inverse correlation between n-hexane adsorption and PE-solid interfacial energies and between benzene and PS-solid interfacial energies. Molecular dynamics and density functional theory calculations performed by our collaborators show strong agreement with our experimental results. Confinement of polymers in nanopores also affect the polymer properties. Prior research in this area has been limited to pore that are greater than the typical size of polymers, ~ 20 nm. In our research, the confined viscosities of polymers are determined from the infiltration times via the Lucas-Washburn equation. The effective viscosity is proportional to 1/pore size in the range from 2 to 20 nm. Based on our observation on the effective viscosity of polyethylene in extreme nanoconfinement, we have proposed a generalized formalism to describe polymer transport dynamics in nanopores. Another important physical property of polymers that may be significantly impacted by confinement is their phase transition temperatures such as melting points of PE. The melting point of PE decreases as the pore size decreases and reaches a saturated value at ~20 C below the bulk melting point. At this point, the pore size is smaller than the minimum crystalline domain of PE. The thesis also introduces an outlook on the investigation of hydrogen solubility in polyethylene within porous material, which is crucial in

many catalytic reactions involved with hydrogen using quartz crystal microbalance. Overall, this thesis contributes substantially to the field of polymer physics in porous media, paving the way for future innovations in material science and engineering of nanocomposites and polymer upcycling.

TABLE OF CONTENTS

LIST OF TABLES

LIST OF ILLUSTRATIONS

CHAPTER 1. INTRODUCTION

1.1 Catalytic Recycling of Polymer

These days, plastic waste is produced globally at a rate of ~380 tonnes per year, while only 20% are recycled. [1]By 2050, there will be ~ 12 billion tonnes of plastic waste in landfills and the environment. [2] To combat these wastes, chemical reactions, such as pyrolysis or cracking, is considered as one of the most promising way for recycling and upcycling. [3–7] During these processes, polymers firstly infiltrate into the porous catalysts and then contact with the metal sites where hydrogenation dehydrogenation happens. The intermediate products have to diffuse to the solid acid supports, where cracking and isomerization undergo.[8–10] The infiltration and transport of polymer chains in nanoscale pores is of significant importance as slow infiltration could potentially lead to unnecessary cracking and generate useless gaseous products. While many recent studies investigate the cracking of polymers on different catalysts, the catalytic performance is normally attributed to the reactivity of the active sites, and the infiltration process is neglected.

Although hydrocracking of polymer is a new topic in the field, hydrocracking of shorter-chain carbon could be dated back decades ago, for example, petroleum residues [11], gas oil [12], crude oil [13], and more recently biomass [14].Considering that the catalysts used in these C-C bond cleavage are similar and the polymer diffusivity is several orders of magnitude lower, understanding the polymer-solid surface interaction and correlating the macromolecules to the micromolecules

could potentially transfer our knowledge from the short-chain hydrocarbon to the polymer processing.

Thus, it is important to study polymer-catalyst interactions and transport of polymers in nanopores, which could have a significant influence on the depolymerization of polymers using heterogeneous porous catalysts. The first step of that objective is to study the surface chemistry of possible porous surface and the polymer physics under confinement via our CaRI model system.

1.2 Polymer-Porous Solid Interactions: Motivations

Polymers are ubiquitously applied in modern sciences and industries including packages, coatings, and other multitude applications.[15–17] The polymer-solid interactions are essential in understanding and controlling polymer-filled nanocomposites and polymer diffusion in polymer-involved reactions such as hydrogenolysis in polymer upcycling reactions.[18–20] These interactions, crucial in determining the overall material performance, extend from affecting mechanical strength to influencing thermal and chemical reactivity and stability.[21–25] However, the surface energies associated with the interface between the polymer and the inorganic solid have not been widely studied[18,26] and the effects of these interactions on the nature of the polymer composite and dynamics is not well understood.[26–30]

The polymer-solid interactions affect polymer diffusion dynamics in both positive and negative ways.[31] Stronger interactions increase the viscous force but also increase the contact friction.[31–33]

The quantification of interactions is not clear and is expressed as weak and strong interactions in different papers.[27,34–37] The contact angle of polymer melt on a solid surface is a natural choice. However, the contact angle cannot be measured precisely by a sessile droplet method because the polymer cannot form a distinct blob when melting like water or other liquids. Therefore, delving into the interfacial energy between polymer melts and solid surfaces, as described by Young's relation, offers a more intrinsic approach to characterizing these interactions. [38,39] As Figure 1.1, the contact angle shows the relationship of the surface tension between liquid, solid, and gas with Young's relation[40] as **Eq (1)**.

$$\gamma_{S-L} = \gamma_{S-G} - \gamma_{L-G} \cdot \cos(\theta) \quad (1)$$

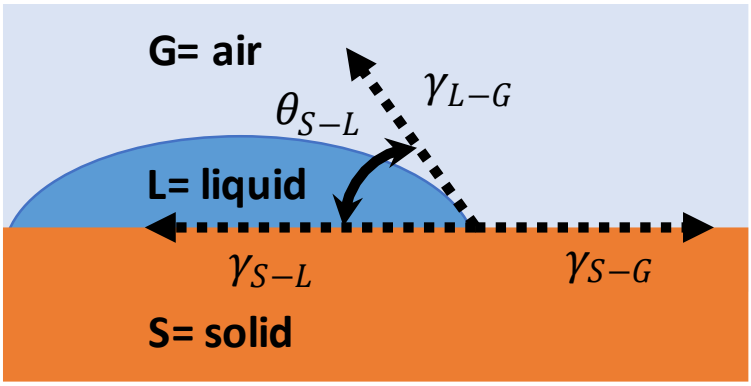

Figure 1.1 The sketch of contact angle and surface tension.

γ_{S-L}=surface tension between liquid and solid;

γ_{S-G}=surface tension between solid and gas;

γ_{L-G}=surface tension between liquid and gas.

In conclusion, the challenge of measuring polymer contact angles on solid surfaces motivates me to develop a novel approach focused on characterizing these angles through the dynamics of polymer diffusion. Additionally, the limited quantitative understanding of polymer-solid interactions inspires me to explore this relationship further by examining the interfacial energy between polymers and solid surfaces.

1.3 Capillary Rise Infiltration(CaRI)：a Paradigm for Studying Polymer Diffusion Dynamics[30,41]

The infiltration and transport of polymer chains in nanoscale pores depend strongly on the wetting characteristics of the polymer on the pore surface as well as on the polymer-pore surface interactions.[30,42–44] Molecular dynamics simulations, for example[45,46], have shown that the dynamics of polymer infiltration into nanopores as well as the final structure and mechanical properties of the composite prepared using such a process depend strongly on the polymer-surface interactions. The typical PINF is the structure of nacre which is a nanocomposite of protein and carbonate. However, it is difficult for us to fabricate highly-loaded-NP NCs by melt-mixing them with more than fifty percent of volume fraction. Different components in high concentration tend to aggregate each other themselves and result into unacceptable nonuniformity. However, CaRI can synthesize high-loading PINFs by polymer diffusion into the fabricated matrix of nanoparticle packings.

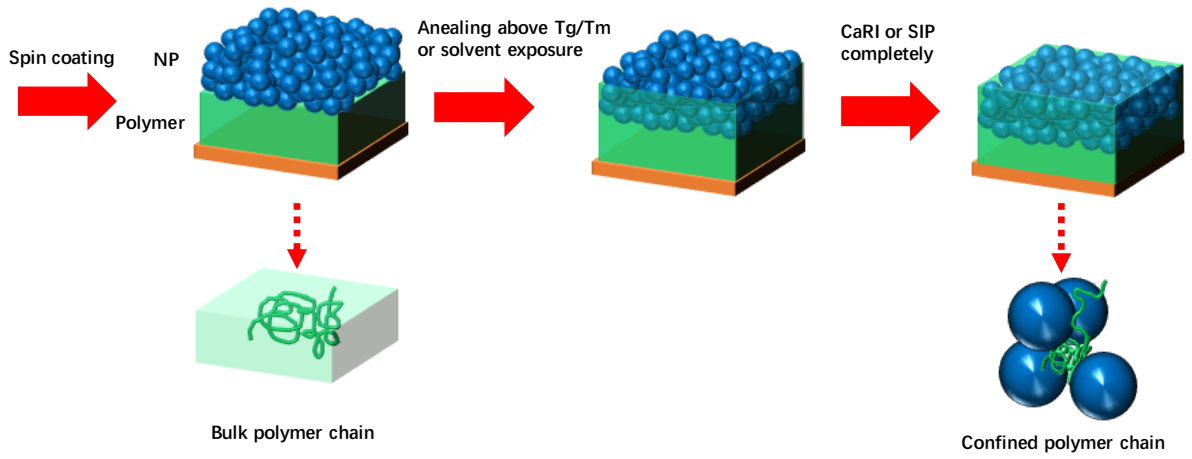

Figure 1.2 The sketch of CaRI.[27,47]

Our typical model CaRI shown in Figure 1.2 starts from the preparation of polymer and NP bilayer. Then the bilayer is annealed above the glass transition temperature or the melting point of the polymer to make the polymer infiltrate into the nanovoids between the NPs by the capillary force.

The capillary rise infiltration (CaRI) process serves as a model system for examining polymers under nanoconfinement.[30,41,48] This mechanism provides a versatile platform for investigating how confined environments impact polymer properties and also offers a promising pathway to fabricate high-loading polymer-infiltrated nanoparticle films (PINFs).[25,26,41]

It is widely applied to various fields including catalysts, multifunctional materials and energy storage with PINFs. Infiltration and motion of molten polymers in nanoporous solids have important implications in several important phenomena and processes.[49] A particularly important

example involves nanoparticle(NP)-polymer composite films and membranes with extremely high filler fractions of NPs.[30,47] These polymer-infiltrated NP films possess superb mechanical[50,51], anti-corrosion[52] and thermal transport properties[45,53,54].

1.4 The Nanoconfinement Effect on Polymer Behavior

Inside the PINFs, there is sometimes a nanoconfinement effect for the polymer. Nanoconfinement imposes a physical state in which a polymer's dimensions are comparable to its molecular size, often resulting in modified properties due to spatial constraints. The polymer size is characterized by the chain length while the polymeric chain length is described by the radius of gyration (R_g), the average square distance of monomers to the mass center of certain polymer chains. The nanovoid size R_{pore} is measured from the nanoparticle skeleton with various kinds of characterizations. For example, the spin-coated nanoparticle layer has a random packing model and its nanovoid size can be calculated as 0.289 of the nanoparticle size. The comparison between the gyration radius of the polymer and the nanovoid radius is demonstrated as R_g/ R_{pore}, which defines the confinement ratio (CR). When CR is over the threshold of 1, it indicates that the polymer can be confined into the nanovoid. When the combination has a CR over 1, all the changed properties confirm the existence of the nanoconfinement.

R_g of different polystyrene (PS) can be calculated according to equation (2)[55]. The nanovoid size is obtained from the random packing of NPs with porosity of 35 vol% for silica NPs and the radius is described as 0.289 of the radius of NPs. R_{pore} of different NPs can be calculated according to equation (3)[56]. The comparison between R_g of polymer and R_{pore} is demonstrated as

R_g/ R_{void}, which defines the confinement ratio (CR). When CR is over the threshold of 1, it indicates that the polymer can be confined into the nanovoid. Different combinations of PS and silica NP have different confinement environments according to the calculation from the Eq (4)[47]. When the combination has a CR over 1, it confirms the existence of the nanoconfinement.[27]

$$R_g = \frac{0.1}{\sqrt{6}} \cdot \left(\frac{Mw}{720}\right)^{0.5} \cdot 18 \text{ (nm, polystyrene)} \qquad (2)[55]$$

$$\frac{R_{void}}{R_{sphere}} = 0.289 \text{ (Gaussian PSD, random packing)} \qquad (3)[56]$$

$$CR = \frac{R_g}{R_{void}} = 0.289 \text{ (Confinement ratio)} \qquad (4)[47]$$

In my previous research system, polystyrene with a molecule weight of 80,000 g/mol and 61nm-diameter silica NP is studied in the infiltration process.[38] The CR of this nanocomposite in my system is 0.89 below 1 which indicates that PS is not confined in the nanovoids statistically. This system is chosen because other variables like the interface chemistry between polymer and nanoparticle wall is focused. However, the next step is to change the nanovoid sizes by varying the nanoparticle sizes and resulting in an environment of nanoconfinement. The nanoconfinement is applied to the system when the CR is below one when the 25nm and 7nm diameter nanoparticle is fabricated into the system.

This phenomenon of confinement effect is not only of academic interest but is also crucial for engineering advanced materials with specific, desired functionalities. It has broad implications for the design of next-generation materials in various fields, including nanotechnology and biomedicine. The study of confined polymers has a rich history. Over time, researchers have explored how constraints affect polymer dynamics, glass transition temperatures, and crystallinity. The interaction of polymers with porous solids, particularly under conditions of nanoconfinement, represents a frontier in polymer research with implications for catalysis, medical technology, and beyond.[31,34,53,57] Advances in analytical methods have brought new precision to these investigations, leading to insights that reshape our understanding of polymer physics.

1.5 Research Gaps and Current Challenges

While significant strides have been made, our understanding of polymers in extreme nanoconfinement, especially concerning crystallinity and melting behavior, remains incomplete. The development of predictive models to capture the essence of polymer behavior in various confined conditions remains a challenge and an area of active research.

Polymer-solid interaction could be quantitively characterized by the interfacial energies between the two materials or the contact angle of the molten polymers on the solid surface. [34,58–60]

However, conventional techniques such as the sessile drop measurement on solid surface is

difficult to perform because the operational temperature of the whole system has to be well above the melting point or glass-transition temperature of the polymers. [27,30,54] Moreover, it is uncertain whether the confinement effect from nanopores could affect the polymer-solid surface interaction similar to the effect on the viscosity. [38] The polymer-solid surface interaction measured in nanopores structure could provide us the direct information without the concern above. Our study of the polymer-solid interactions and confined polymer properties can assist in improving the reactivity and selectivity of polymer upcycling reactions.

1.6 Aims of the Current Investigation

The central goal of this thesis is to shed light on polymer interaction with porous media and its physics of the viscosity and melting point under nanoconfinement within nanoporous media. The research endeavors to:

- Characterize and quantify the polymer-solid interactions by studying the impact of pore surface chemistry.
- Understand and control polymer-solid interactions by relating to the adsorption energy of small molecules.

- Quantify the influence of pore dimensions on polyethylene's effective viscosity.
- Examine shifts in polyethylene's melting behavior due to nanoconfinement.
- Refine theoretical models to accurately describe these effects.

1.7 Structure Outline of the Thesis

Organized into seven chapters, this thesis systematically addresses various aspects of polymer confinement and interactions with porous solids. Subsequent chapters will provide in-depth analysis based on the author’s published and pre-published works, leading to a synthesized understanding of polymer-solid interactions and confined polymer properties. The final chapter will summarize the findings and propose future research directions:

In Chapter 2, the study delves into the nuanced control and quantitative analysis of the interactions between molten polystyrene and porous solids, facilitated by the precision of Atomic Layer Deposition (ALD) techniques. It provides insights into how modifying surface chemistry at the nanoscale can influence polymer behavior.

The focus of Chapter 3 shifts to understanding the subtleties of polymer-porous solid interactions through the lens of small gas molecule adsorption. The chapter discusses how adsorption behavior can reveal underlying interaction mechanisms and influence polymer dynamics.

Chapter 4 investigates the increased effective viscosity of polyethylene when subjected to extreme nanoconfinement. It explores the development of a generalized formalism to describe

the translational dynamics of polymers, offering a theoretical framework for understanding these phenomena.

Chapter 5 elucidates the factors leading to the decreased melting point of polyethylene in extremely confined spaces. It examines the role of confinement on crystalline structure and phase transitions, contributing to a deeper understanding of polymer thermodynamics under spatial constraints.

In Chapter 6, a preliminary study on hydrogen solubility in polyethylene is presented, employing a custom-built Quartz Crystal Microbalance (QCM). This investigation provides a novel perspective on how confinement affects the solubility and diffusion of small molecules in polymers.

Chapter 7 of the summary and outlook concluding chapter synthesizes the research findings from the preceding chapters, providing a cohesive summary of the quantification and controlling of polymer-solid interactions and the impact of nanoconfinement on polymer properties. It also outlines potential future research directions, drawing from the gaps and questions unearthed during this study.

This thesis enriches our fundamental understanding of polymer behavior under nanoconfinement and its interaction with porous media. By elucidating the relationship between polymer characteristics and confinement, it guides the synthesis of materials with tailored properties and offers valuable insights for future research endeavors.

CHAPTER 2. QUANTITATIVE CHARACTERIZING AND CONTROLLING THE INTERACTIONS BETWEEN MOLTEN POLYSTYRENE AND POROUS SOLIDS USING ATOMIC LAYER DEPOSITION (ALD)

Reproduced from Ren, T.; Huang, R.; J. Gorte, R.; Lee, D. Modulating Interactions between Molten Polystyrene and Porous Solids Using Atomic Layer Deposition. *Langmuir 2021, 37* (49), 14520–14526. https://doi.org/10.1021/acs.langmuir.1c02604.

2.1. Introduction

Infiltration and motion of molten polymers in nanoporous solids have important implications in several important phenomena and processes.[49] A particularly important example involves nanoparticle(NP)-polymer composite films and membranes with extremely high filler fractions of NPs prepared via capillary rise infiltration of polymer into packings of NPs.[30,41] These polymer-infiltrated NP films possess superb mechanical[50,51], anti-corrosion[52] and thermal transport properties[45,53,54]. Diffusion of polymer chains into porous solids can also play an important role in the catalytic reactions involved in polymer upcycling.[18,61,62] The infiltration and

transport of polymer chains in nanoscale pores depend strongly on the wetting characteristics of the polymer on the pore surface as well as on the polymer-pore surface interactions.[30,42–44] Molecular dynamics simulations, for example[45,46], have shown that the dynamics of polymer infiltration into nanopores, as well as the final structure and mechanical properties of the composite prepared using such a process, depend strongly on the polymer-surface interactions. It is, however, difficult to change the surface composition of the solid without also changing the size and shape of the pores. In this regard, atomic layer deposition (ALD) is ideal for modifying the surface composition of porous solids because deposition is uniform and typical growth rates are less than a monolayer per cycle.[63–65]

Although a number of studies[63,64,66–68] have demonstrated that changing the surface composition by ALD can affect the physicochemical properties of solid surfaces, few studies have systematically varied the surface composition to determine how this influences the interactions of a molten polymer and the porous material. Polymer-solid surface interactions can be quantitatively characterized by measuring the contact angle of the molten polymer on the solid surface or determining the interfacial energy between the two materials.[69–72] However, it is difficult to perform conventional techniques such as contact angle analysis using sessile droplets on a solid surface because such measurements must be performed above the melting or glass transition temperatures of the polymer.[27,30,54] Determining the contact angle of a molten polymer on the surface of nanopores is even more challenging.[69] Contact angle measurement on planar substrates may not be relevant because of the potential curvature effect on the polymer wetting on the pore surface. Also such a measurement is not trivial to perform for polymers because the

entire system including the vapor phase has to be kept at the target temperature. The ability to engineer polymer-surface interactions in porous solids and to quantify such interactions will be important for understanding transport of the polymer into the solid and catalytic processes involving molten polymers in porous media.[30,42,43] ALD modification of porous materials could also enable fabrication of nanocomposite films and membranes with tailored interactions between the solid and polymer, which has important implications for their mechanical and transport properties.[43,50,51]

In this work, we take advantage of capillary rise infiltration of polymers into a disordered packing of NPs to quantitatively characterize the effect of surface composition on the interactions between polystyrene (PS) and surface of the packing. Successful deposition of TiO_2, WO_3, $CaCO_3$ in the interstices of SiO_2 NP packings is confirmed by directly measuring the mass uptake and by characterizing the changes in the refractive index of the NP packing.[67,68,73] We find that the contact angle of PS depends strongly on the surface compositions. The contact angle of PS changes gradually from that on pure SiO_2 to that of the added material as the surface coverage is increased, saturating once a complete monolayer is achieved. $CaCO_3$ exhibits the lowest interfacial energy of the materials we study, indicating highly favorable interactions with PS, whereas WO_3 has the least favorable interactions with PS. Interestingly, water contact angles on these ALD-modified surfaces are not an accurate predictor of the interfacial energy between PS and ALD-modified surfaces, emphasizing the importance of determining the contact angle and interfacial energy using the method introduced in this work. [69,74]

2.2. Experimental

2.2.1 Materials

Polystyrene (PS) with a molecule weight of 88,000 g/mol (polydispersity index = 1.1) is purchased from Polymer Source Inc. 60 nm silica (SiO_2) NP suspension (ST-YL, 30 wt% suspension in water) is generously provided by Nissan Chemical. Titanium chloride ($TiCl_4$), tungsten hexacarbonyl ($W(CO)_6$) and bis(2,2,6,6-tetramethyl-3,5-heptanedionato) calcium ($Ca(TMHD)_2$) are purchased from STREM Chemicals, Inc.

2.2.2 Fabrication of Polymer-NP Packing Bilayer

NP suspension is made by mixing 2 mL 30 wt% dispersion of 60 nm SiO_2 NPs and 2 mL (~15 wt%) deionized (DI) water, which is sonicated for 3 hours. The suspension is filtered with a hydrophilic syringe filter (0.45 μm pore size, Fischer Scientific) to remove aggregates. A silicon (Si) wafer is cut into 10×10 mm^2 pieces. 227±3-nm-thickness NP layer is spin-coated onto the plasma-treated silicon wafers at 6,500 rpm for 60 sec with a spin coater (Model WS-400BZ-6NPP Lite, Laurell Technologies Corporation). All the NP layers are dried under vacuum overnight. Before ALD, they are heated at 773 K for one hour to remove water. Subsequently, these NP layers are ALD-treated (see ALD method for details).

The PS solution is made at 2.5 wt% with toluene and sonicated for 3 hours. The solution is filtered with a PTFE filter (0.22 μm pore size, Thermo Scientific) to remove the undissolved

impurities. 175±3-nm -thickness PS layer is also spin-coated onto a plasma-treated (oxygen plasma for 6 minutes at 250 mTorr) Si wafers at 3,000 rpm for 60 s with the spin coater.

Bilayer preparation takes advantage of the hydrophobicity of PS. The newly spin-coated PS thin film is scored along the edges and then immersed into DI water. The PS film delaminates from the scored edges due to its high hydrophobicity and floats onto the water surface as a free-standing film. This PS layer is loaded onto the NP film on a Si wafer by immersing and raising the NP film through the water surface. The bilayer is subsequently dried in the ambient condition. The polymer film conformally adheres to the nanoparticle film due to strong capillarity that results from drying of water in the interstices of nanoparticles. To confirm that there are no voids that could impact the infiltration time measurement, we confirm that the thickness of each bilayer is equal to the sum of the thicknesses of the nanoparticle and the polymer films measured separately on silicon wafers. We also confirm that the infiltration time measured using a bilayer with a SiO_2 nanoparticle packing on top of a PS film is equal to the infiltration time measured using the bilayer prepared using the method used in this study; these results confirm that there are no voids between the polymer and the nanoparticle packing.

2.2.3 ALD Method

ALD is performed in a homebuilt, static system using procedures that have been described in detail[67,68,73,75]. A schematic of the sample holder used to prepare the NP films is shown in Figure 2.1.

(a)

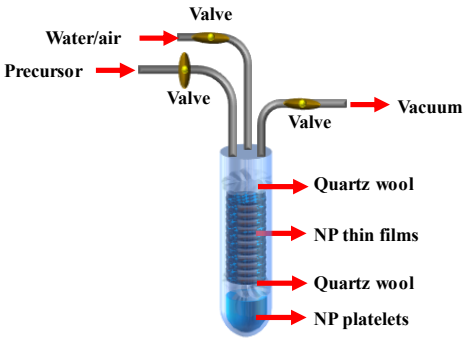

(b)

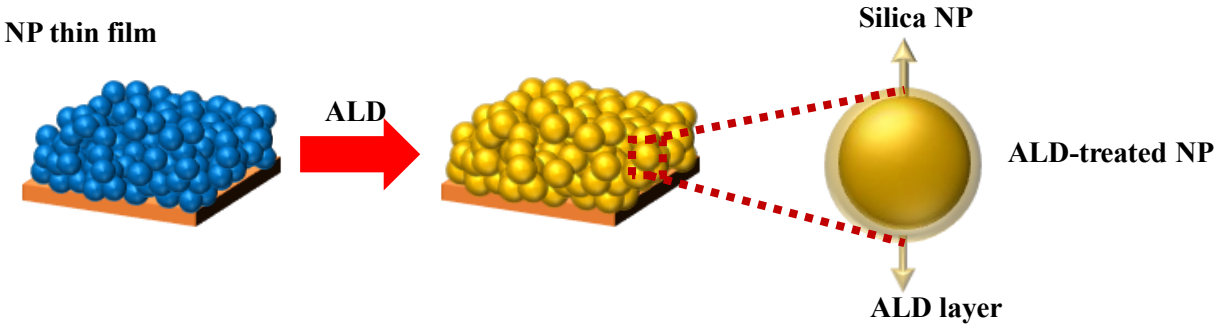

Figure 2.1 Schematic illustration of (a) ALD chamber and sample holder and (b) ALD modification of a disordered packing of NPs.

The precursors for CaO, WO_3, and TiO_2 are $Ca(TMHD)_2$ (TMHD = 2,2,6,6-tetramethyl-3,5-heptanedionato), $W(CO)_6$, and $TiCl_4$. (Note: CaO converts to $CaCO_3$ in the presence of CO_2 [28].) Briefly, the evacuated substrates are exposed for 5 min to a few Torr of the precursor of interest. The exposure temperatures are 573 K for $Ca(TMHD)_2$ and 473 K for $W(CO)_6$ and $TiCl_4$. The samples are then evacuated to remove excess precursor. For $W(CO)_6$, the carbonyl groups is

removed by exposure to air at 473 K[67]; for $TiCl_4$, exposure to water vapor at 473K is sufficient to convert the precursor to TiO_2[68]. However, with $Ca(TMHD)_2$, the sample is evacuated, removed from the system, and then calcined in a muffle furnace for 10 min at 873 K to remove the TMHD ligands[73]. One ALD cycle consists of an exposure to the precursor, evacuation, and removal of the ligands. Growth rates are monitored using two methods. First, the weight gains are measured after each ALD cycle on a bed of SiO_2 NP using a microbalance with the precision of 1 mg. Separately, the refractive index of thin NP films is measured via ellipsometry with the precision of 0.001. For ALD on NP thin films, 11 NP-film samples are prepared simultaneously in the same static system. The refractive index of thin films is measured via spectroscopic ellipsometry which enables estimation of ALD growth as discussed later.

2.2.4 Characterization of Capillary Rise Infiltration of Polymer into ALD-Modified NP Packed Films

The infiltration time measurements are performed at 423 K (150 ºC) on a Linkam THMS350 V heating stage. It takes 4 minutes to increase the temperature from room temperature to the target temperature then the temperature is held constant for one hour. We choose 423 K (150 ºC) as the annealing temperature because this temperature provides the most appropriate range of infiltration times (100 – 1,000 sec). *In situ* ellipsometry is performed to monitor the polymer infiltration process; the amplitude ratio (Ψ) and phase difference (Δ) of the polarization between the incident and reflected light are measured as a function of time. The infiltration process is observed to be completed when the dynamic data stop changing. The infiltration time is defined by measuring the time between time point when the Δ and Ψ start changing and the time point

when changes are no longer observed. After infiltration process, there is a residual PS layer atop the PS-filled nanoparticle film after infiltration process. Our ellipsometry modeling accounts for this residual PS layer. The thickness of the residual PS layer matches what would be expected based on the loss of PS to fill the interstices of the underlying nanoparticle layer. Our prior publications have provided SEM images of such bilayers after infiltration.[27,30,41]

2.2.5 Contact Angle Determination on ALD-Treated Samples

The contact angles of both water and diiodomethane on ALD-treated Si wafers are measured using a goniometer [74] to infer the interfacial energy between PS and ALD modified surfaces.

2.3 Results and Discussions

2.3.1 ALD Modification of SiO_2 NP Packings

Atomic layer deposition (ALD) is used to modify the surface of the interstitial pores in random packing of 60 nm ($2 \cdot R_{NP}$) SiO_2 NPs. Deposition of different materials on the surface of SiO_2 NPs (see Experimental Section for details) is characterized by measuring the mass uptake of bulk samples of SiO_2 NP packing as well as the changes in the refractive index of SiO_2 NP films using spectroscopic ellipsometry. We choose to modify the SiO_2 surfaces with TiO_2, WO_3 and $CaCO_3$ because these inorganic solids possess widely varying properties. The thickness of each ALD deposition (Δh) is calculated from the mass uptake (Δm) of the bulk SiO_2 NP packings (m) by using Eq (1), which assumes that the surface area (S) of the packing stays constant through the deposition process (see SI for derivation):

$$\Delta h = \frac{\Delta m}{\rho_{ALD} \cdot v_{NP} \cdot S} = \frac{\Delta m \cdot \rho_{NP} \cdot R_{NP}}{3 \rho_{ALD} \cdot m} \quad (1)$$

where ρ_{NP}, ρ_{ALD}, v_{NP} and v_{ALD} are the density and volume fraction of NPs and ALD material, respectively. The ALD thickness inferred from the mass uptake increases linearly with the number of cycles for the three materials studied in this work. Likewise, the thickness of each ALD on the pore surface of the densely packed SiO_2 NP films is estimated by converting the change in the refractive index of the film (Δn), which depends on the void fraction of the NP packing, to the thickness increase ($\Delta h'$) using:

$$\Delta h' = \frac{m}{\rho_{NP} \cdot S} \cdot \frac{v_{ALD}}{v_{NP}} = \frac{R_{NP}}{3} \cdot v_{ALD} = \frac{R_{NP}}{3} \cdot \frac{\Delta n}{(n_{ALD} - n_{air})} \quad (2)$$

where n_{ALD} and n_{air} are the refractive indices of the material deposited via ALD and air, respectively. Then the deviation is shown as following paragraphs.

The thickness of ALD layer on the surface of SiO_2 NPs ($\Delta h'$) is estimated from the refractive index increase at the range of 632.8 nm, Δn, using the mixing rule. The total refractive index n_{total} of ALD-treated NP packing is the summation of the product of every component' s refractive index n_i and its volume fraction v_i as shown in Eq (3):

$$n_{total} = \sum n_i \cdot v_i = n_{NP} \cdot v_{NP} + n_{ALD} \cdot v_{ALD} + n_{air} \cdot v_{air}$$

$$= n_{NP} \cdot v_{NP} + n_{ALD} \cdot v_{ALD} + n_{air} \cdot (1 - v_{NP} - v_{ALD})$$

$$= (n_{ALD} - n_{air}) \cdot v_{ALD} + n_{NP} \cdot v_{NP} + n_{air} \cdot (1 - v_{NP})$$

$$= (n_{ALD} - n_{air}) \cdot v_{ALD} + n_{total\ with\ no\ ALD}. \qquad (4)$$

Using Eq (2), the refractive index increase Δn can be expressed as $(n_{ALD} - n_{air}) \cdot v_{ALD}$. The thickness increase $\Delta h'$ can be calculated from the volume fraction of material deposited via ALD, v_{ALD}, with Eq (5):

$$\Delta h' = \frac{m}{\rho_{NP} \cdot S} \cdot \frac{v_{ALD}}{v_{NP}} = \frac{R_{NP}}{3} \cdot v_{ALD} = \frac{R_{NP}}{3} \cdot \frac{\Delta n}{(n_{ALD} - n_{air})} \qquad (5)$$

where S is the surface area and can be expressed as:

$$S = \frac{m}{\rho_{NP} \cdot v_{NP} \cdot \frac{4}{3}\pi {R_{NP}}^3} \cdot 4\pi {R_{NP}}^2 = \frac{3m}{\rho_{NP} \cdot v_{NP} \cdot R_{NP}} \qquad (6)$$

where the ρ_{NP} is the density of silica and R_{NP} is the radius of silica NP.

The thickness determined from ellipsometry of NP films also show a linear increase and is in good agreement with the results based on the mass uptake shown in Figure 2.2, indicating that ALD is able to successfully modify the surface of the SiO_2 NPs uniformly in the dense packings of SiO_2 NPs. The growth rates of TiO_2, WO_3 and $CaCO_3$ ALD are 0.7 Å, 0.8 Å and 0.5 Å per ALD cycle, respectively. On the atomic basis, the growth rates for three precursors are calculated to be 8.6×10^{13} Ca/cm^2-cycle, 1.6×10^{14} W/cm^2-cycle, and 2.1×10^{14} Ti/cm^2-cycle in reasonable agreement with previous literature values. As a comparison, a previous work for ALD on high-surface-area $MgAl_2O_4$ showed the growth rates for the precursors used in this study to be 6.9×10^{13} Ca/cm^2-cycle[73], 8.6×10^{13} W/cm^2-cycle[67], and 9.8×10^{13} Ti/cm^2-cycle.[68]

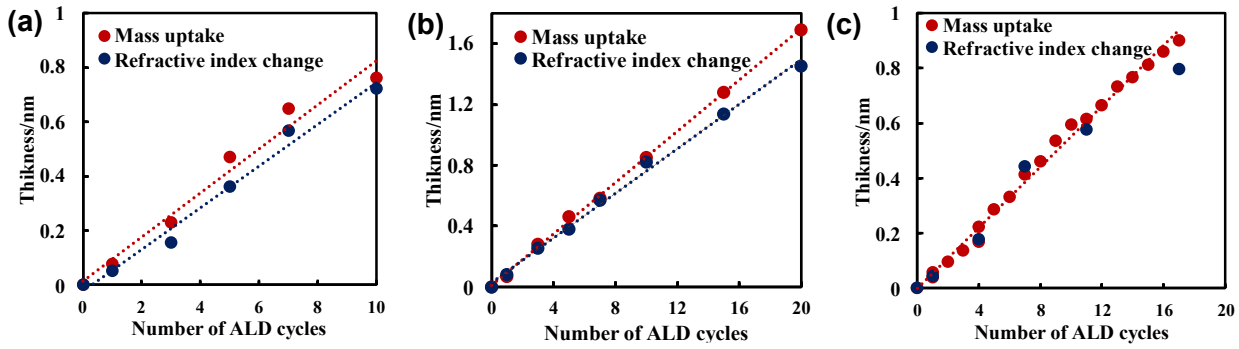

Figure 2.2 Thickness increase for (a) TiO_2, (b) WO_3 and (c) $CaCO_3$ ALD on packings of silica NPs as a function of ALD cycles.

2.3.2 Determination of Contact Angle and Interfacial Energy

To investigate the effect of ALD on the wetting of PS on the interstitial pores of SiO_2 NP packings, a bilayer of ALD-modified SiO_2 NP layer and PS (MW = 88,000 g/mol) is prepared. Because ALD involves a high temperature oxidation treatment at 773 K, it is necessary to prepare the ALD-modified NP layer first and then deposit the polymer layer on top as schematically illustrated in Figure 2.3. Such a bilayer is prepared by transferring a free-standing 175±3 nm thick PS film on the water surface onto an ALD modified SiO_2 NP film (227±3 nm in thickness) (see Experimental Section for details). The bilayer is heated to 423 K to induce capillary rise infiltration of PS into the interstices of ALD-modified SiO_2 NP film. The infiltration time is measured by monitoring the changes in the amplitude ratio (Ψ) and phase difference (Δ) of the polarization between the incident and reflected light as a function of time using a spectroscopic ellipsometer.

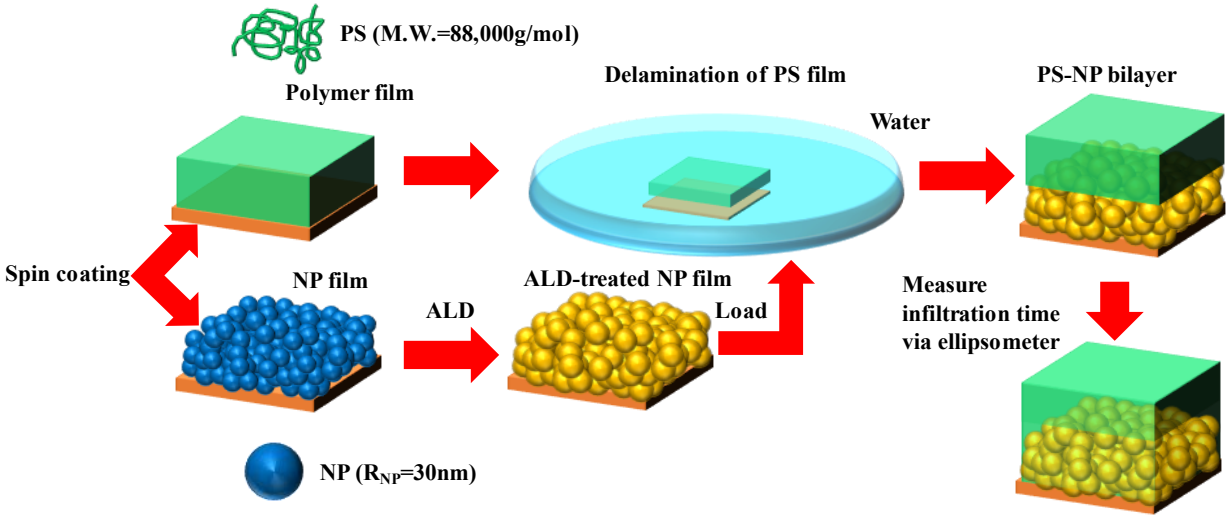

Figure 2.3 Schematic illustration of preparation of a PS-NP packing bilayer for contact angle determination.

The contact angle of PS on the ALD-modified pores of SiO_2 NP films is inferred by using the Lucas-Washburn equation[41,76,77] which describes the dependence of the height of capillary rise of a liquid in a porous medium (h) on the surface tension (γ_{PS-G}), pore size (R_{pore}), contact angle (θ), liquid viscosity (μ), tortuosity (τ) and time (t):

$$h^2 = \frac{\gamma_{PS-G} \cdot R_{pore,SiO_2} \cdot cos\theta}{4 \cdot \tau^2 \cdot \mu} t \qquad (7)$$

The polymer surface tension $\boldsymbol{\sigma}$ and polymer size (molecular weight) can affect the infiltration time. Our prior work has focused on the effect of molecular weight on the infiltration dynamics[26,30,44,78] In our study, this PS is chosen as a model to investigate how the surface chemistry of the nanopore impacts the infiltration process and thus the contact angle between the ALD-modified surface and polymers.

The Lucas-Washburn model is often modified with a tortuosity factor $\boldsymbol{\tau}$ to account for the meandering path of the pores to describe the infiltration of polymers in nanoporous media.[27,30,41,76,79,80] Because the tortuosity does not change upon ALD modification without changing the pore geometry, the exact value of τ is not necessary to determine the contact angle.

The Washburn model can be expressed as $\boldsymbol{h^2 = \frac{\sigma R_h cos\theta}{2\tau^2 \mu} t}$ [80] where the $\boldsymbol{R_h}$ is hydraulic radius which is the ratio of the fluid volume filled in pores to the wetted surface area of pores. The average pore size $\boldsymbol{R_{pore}}$ in the wick volume is $\boldsymbol{2R_h}$ by equating the pore volume in the wick with the total volume of the cylindrical tubes.[80] In this way, the Lucas-Washburn equation is expressed as $\boldsymbol{h^2 = \frac{\sigma R_{pore} cos\theta}{4\tau^2 \mu} t}$ [76,79,80].

The parameters that are used for the Lucas-Washburn equation are summarized in Table 2.1.

Table 2.1 Parameters used in the Lucas-Washburn model (Eq (1)).

NP radius, R_{NP} (nm)	Average pore size, R_{pore} (nm) [42,56]	Tortuosity, τ[42]	PS molecular weight, M.W. (g/mol)	PS surface tension, γ_{PS-G} $(mN \cdot m^{-1})$ [81]	PS contact angle on SiO_2 surface, θ (°)[41,43]	Height of capillary rise, h (nm)

30	8.7	1.95	88,000	31.3 (at 423K)	20	220-230

We use the infiltration time of PS in an untreated silica NP packing as a reference to calculate contact angles of ALD modified packings using as Eq (3). The infiltration time (t) is measured based on spectroscopic ellipsometry as described in the main manuscript; a representative dynamic data of infiltration into a SiO_2 NP packing modified with 5 cycles of TiO_2 ALD is shown in Figure 2.4. A bilayer of PS atop ALD-modified NP layer is annealed on the heating stage for 1 hour. In the Figure 2.4, the start of infiltration is the first point that is different by 1% from the 5 preceding data points. The end of infiltration is the first point smaller that is different by less than 1% than the 5 preceding data points. It takes ~ 3 min for the sample to reach the target temperature to observe the changes in the ellipsometry signals (ψ and Δ), indicating the initiation of PS infiltration. The capillary rise infiltration of PS is observed to be completed when ψ and Δ reach asymptotic values around ~14.3 min. In the example Figure 2.4, the infiltration time is 698 sec.

(a)

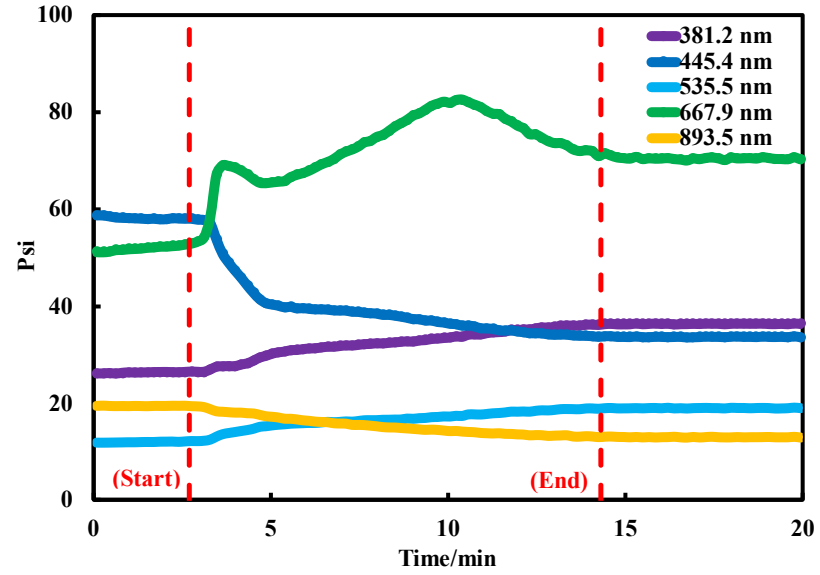

(b)

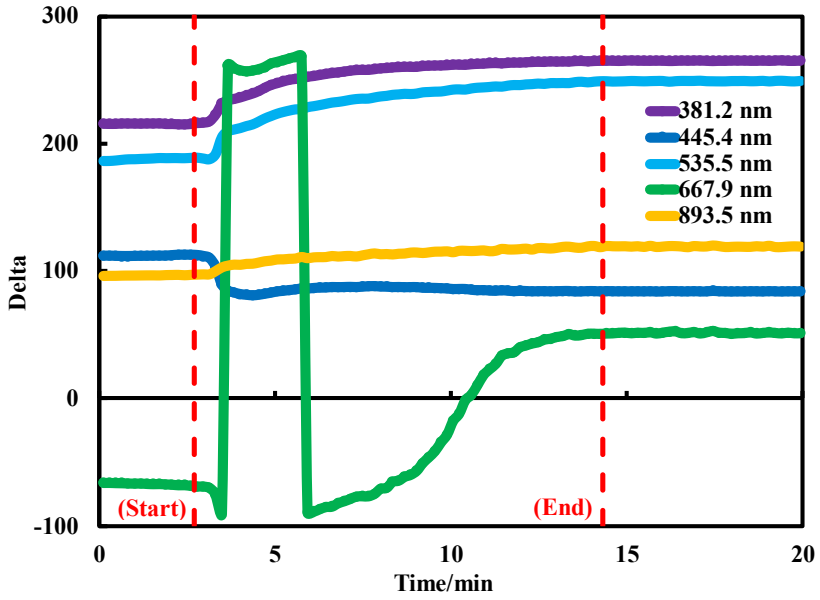

Figure 2.4 Representative data showing the changes in dynamic data as a function of time for infiltration of PS into 5-cycle TiO_2-ALD NP layer: (a) ψ; (b) Δ.

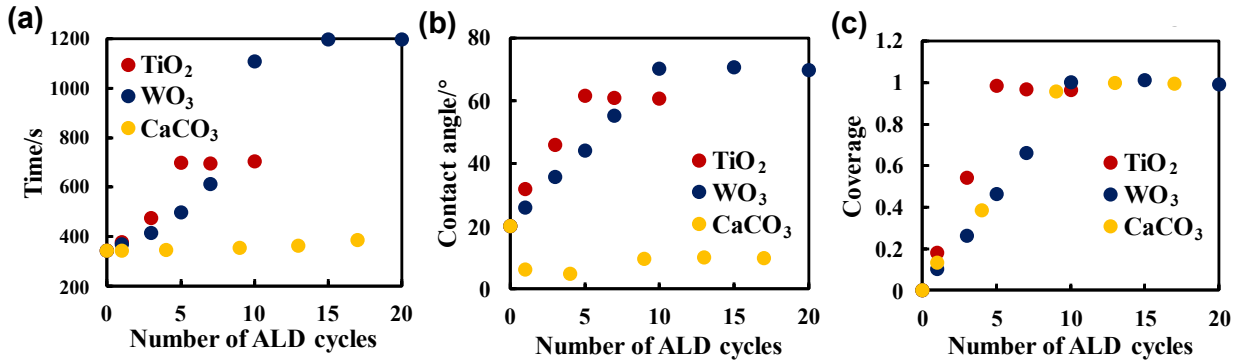

Figure 2.5 (a) Infiltration time; (b) contact angle of PS on ALD-modified surfaces; (c) degree of surface coverage of ALD materials as a function of ALD cycles. The thickness of the SiO_2 NP film is 227±3 nm.

The average pore size in random packings of spheres is known to be ~ 30% of the size of the particles, thus $R_{pore,SiO_2} \approx 9$ nm**.** To infer the contact angle of PS on ALD-treated pore surfaces, we use the reported value of 20 ^{0} for the contact angle of PS on untreated SiO_2 NP (θ_{SiO_2} in Eq (3)) [41,44,82]. The change in the pore size ($R_{pore,ALD}$) induced by ALD is less than 1 nm, which is less than 10% of the average pore radius in the NP packing. Contact angle (θ_{ALD}) of PS on the ALD modified pore surface of NP films is inferred by measuring the time of infiltration (t_{ALD}) while taking into account the change in the size of the pore due to ALD.

For each of the three materials examined in this study, the infiltration time changes gradually from its initial value to a saturation value as the number of ALD cycles is increased as shown in Figure 2.5**.** For example, the infiltration time (t_{ALD}) for PS in the TiO_2 ALD-treated NP films increases with the number of ALD cycles, indicating that the wetting of PS on the modified

surface becomes less favourable on TiO_2 surface. More importantly, the infiltration time saturates at ~700 sec after 5 cycles of ALD deposition indicating that TiO_2 completely covering the SiO_2 surface. This result is consistent with our prior studies that showed that a complete layer of TiO_2 is formed after 5 cycles of ALD as confirmed by using transmission electron microscopy (TEM) and scanning transmission electron microscope (STEM).[75] The thickness of TiO_2 ALD after 5 cycles based on the growth rate of 0.7 Å/cycle is 0.35 nm, remarkably consistent with the previously reported value for a monolayer of TiO_2 layer of 0.35 nm[83]. The contact angle of PS on TiO_2 ALD-modified SiO_2 NP films increases from that of PS on unmodified SiO_2 NP films to ~62 ^{0} as shown in Figure 2.5. The infiltration time of untreated silica NP is used as reference t_{SiO_2} at 342 sec.

Using the same approach, the contact angles of PS on the pore surface of SiO_2 NP films fully covered with WO_3 and $CaCO_3$ are estimated to be 70° and 10^0, respectively. The thickness at which the contact angle shows saturation for each material is again in excellent agreement with the reported value of a monolayer of the respective material (0.77 nm and 0.40 nm for WO_3 and $CaCO_3$, respectively[84,85]).

The surface coverage (φ_{ALD}) of each material deposited via ALD on SiO_2 NP surface estimated by assuming that the composite infiltration time is a linear combination of the two surfaces using:

$$\varphi_{ALD} = \frac{R_{pore,SiO_2} \cdot \cos(\theta_{SiO_2}) \cdot (1 - \frac{t_{SiO_2}}{t_{ALD}}) h_{ALD}^2}{R_{pore,SiO_2} \cdot cos(\theta_{SiO_2}) \cdot h_{ALD}^2 - R_{pore,ALD} \cdot cos(\theta_{ALD}) \cdot h_{SiO_2}^2} \qquad (8)$$

, increases linearly with the number of ALD cycles until the SiO_2 surface is completely covered with the correspond material. We show how the contact angle of PS on ALD-modified surface can be inferred. Based on the Eq (7), the infiltration time for PS into un-modified SiO_2 NP packing can be expressed as:

$$t_{SiO_2} = \frac{4\tau^2 \cdot \mu \cdot {h_{SiO_2}}^2}{\cos(\theta_{SiO_2}) \cdot \gamma_{PS-G} \cdot R_{pore,SiO_2}} \qquad (9)^{41,76}$$

The subscript of each parameter represents the surface composition of the pore surface. The infiltration time of PS into NP packing that is modified with a monolayer of TiO_2 can be expressed as:

$$t_{TiO_2} = \frac{4\tau^2 \cdot \mu \cdot {h_{TiO_2}}^2}{\cos(\theta_{TiO_2}) \cdot \gamma_{PS-G} \cdot R_{pore,ALD}} = \frac{\cos(\theta_{SiO_2}) \cdot R_{pore,SiO_2} \cdot {h_{TiO_2}}^2}{\cos(\theta_{TiO_2}) \cdot R_{pore,TiO_2} \cdot {h_{SiO_2}}^2} \cdot t_{SiO_2} \qquad (10)$$

The infiltration time of PS in TiO_2 ALD-treated surface, t_{TiO_2}, is the summation of the product of every component' s surface coverage (φ_i) on SiO_2 NP surface and corresponding infiltration time (t_i):

$$t_{ALD} = \varphi_{TiO_2} \cdot t_{TiO_2} + \varphi_{SiO_2} \cdot t_{SiO_2}$$

$$= \varphi_{ALD} \cdot t_{TiO_2} + (1 - \varphi_{ALD}) \cdot t_{SiO_2} = \left(t_{TiO_2} - t_{SiO_2}\right) \cdot \varphi_{ALD} + t_{SiO_2}$$

$$= \left(\frac{\cos(\theta_{SiO_2}) \cdot R_{pore,SiO_2} \cdot {h_{ALD}}^2}{\cos(\theta_{TiO_2}) \cdot R_{pore,TiO_2} \cdot {h_{SiO_2}}^2} - 1\right) \cdot t_{SiO_2} \cdot \varphi_{ALD} + t_{SiO_2} \qquad (11)$$

The surface coverage of ALD material (φ_{ALD}) can be expressed as:

$$\varphi_{TiO_2} = \frac{R_{pore,SiO_2} \cdot \cos(\theta_{SiO_2}) \cdot (1 - \frac{t_{SiO_2}}{t_{TiO_2}}) h_{ALD}^2}{R_{pore,SiO_2} \cdot cos(\theta_{SiO_2}) \cdot h_{DTiO_2}^2 - R_{pore,ALD} \cdot cos(\theta_{TiO_2}) \cdot h_{SiO_2}^2} \qquad (12)$$

which can be generalized for other species as shown in Eq (8).

These results convincingly show that the surface chemistry, and thus their wetting properties, is significantly changed by the surface composition, modified by ALD. These measurements indicate that the wettability of PS on WO_3 is even less favourable than that on TiO_2 and SiO_2 with the saturation contact angle of 70^0, whereas PS favourably wets on the $CaCO_3$ surface with the contact angle of 10^0.

Contact angle of PS on ALD-modified surface provides an important insight into the strength of interactions between the polymer and the surface. Another important parameter that can be inferred from the contact angle is the interfacial energy between PS and ALD-treated surface. While the contact angle provides a convoluted measure of the strength of interactions that balances three interfacial tensions based on the Young's relation, the interfacial tension is a direct measure of the strength of interactions. To estimate the interfacial energy between PS and the ALD-modified surface, the surface energy of the solid surface as well as the surface tension between PS are needed. We estimate the interfacial energy of the solid surfaces by using the method introduced by Owens and Wendt.[69,71,74,86,87] This method gives an estimation of the surface energy of a solid surface by measuring the contact angle of two well-characterized probe liquids, water, and diiodomethane on the surface. The contact angles of water and diiodomethane

on the ALD-modified surfaces are summarized in Table 2.2. Using the Young's equation, the interfacial energy between PS and pore surfaces studied in this work can be estimated as shown in Figure 2.6.

Table 2.2 Contact angles (º) of water, diiodomethane and PS on solid surfaces prepared via ALD.

Material	$CaCO_3$	SiO_2	TiO_2	WO_3
Water	38	20	18	16
Diiodomethane	53	43	33	28
PS	10	20	62	70

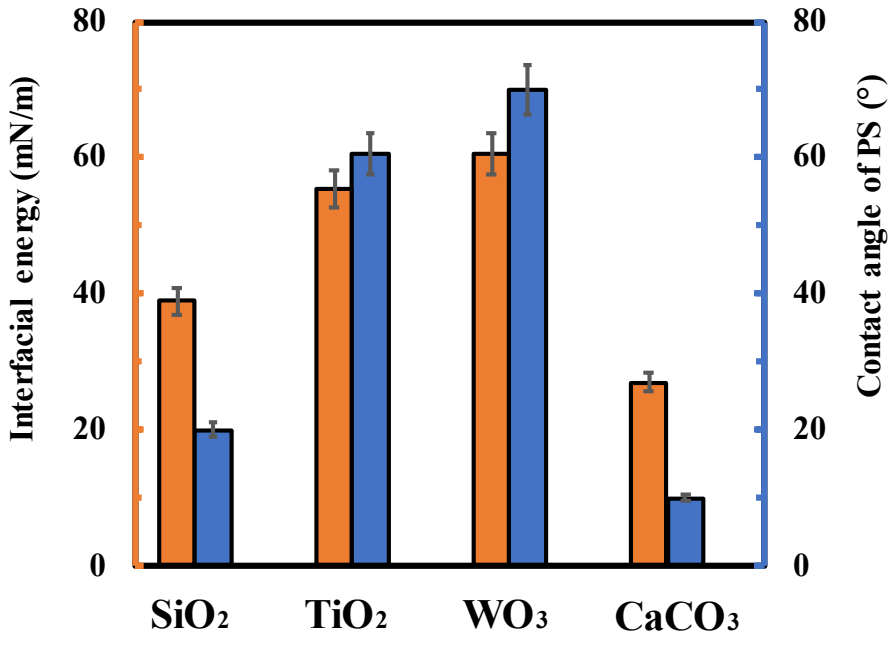

Figure 2.6 Contact angle and interfacial energy of different surfaces prepared via ALD. The interfacial energy between PS and solid is plotted in orange, whereas the contact angle of PS on solid is presented in blue.

As shown in Figure 2.7, the contact angle of a liquid droplet on a solid surface depends on the three interfacial tensions involved following the Young's equation[40]:

$$\gamma_{S-L} = \gamma_{S-G} - \gamma_{L-G} \cdot \cos(\theta_{S-L}) \quad (13)$$

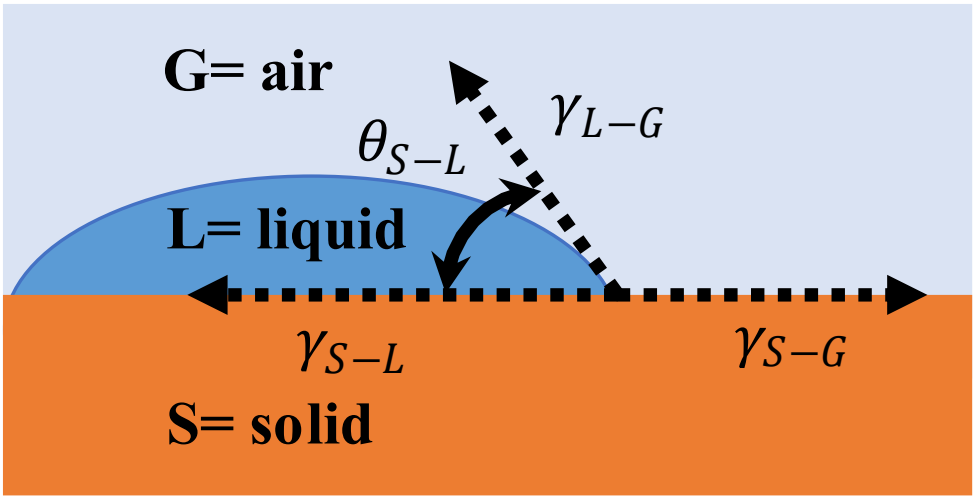

Figure 2.7 Schematic illustration of contact angle and interfacial tensions. $\gamma_{S-L}, \gamma_{S-G}$ *and* γ_{L-G} are interfacial energy between liquid and solid, surface energy of the solid and surface tension of the liquid, respectively.

To estimate the surface energy of ALD-modified surfaces, we measure the contact angles of two different liquids, water and diiodomethane, and infer the surface energy from such data.

[71,74,86,88]Fowkes showed that the dispersive interactions between the solid and liquid are stronger than all other forces.[74,88] Based on Owens and Wendt method with Fowkes' finding, the surface energy of a solid surface can be calculated using:[71,74]

$$2\sqrt{\gamma_{S-G}^{d} \cdot \gamma_{L-G}^{d}} + 2\sqrt{\gamma_{S-G}^{nd} \cdot \gamma_{L-G}^{nd}} = \gamma_{L-G} \cdot (1 + cos\theta_{S-L}) \qquad (14)^{71,74}$$

where γ_{L-G} and γ_{S-G} are the surface tension of the liquid and the surface energy of the soild, respectively. γ_{S-G}^{d} and γ_{L-G}^{d} are dispersive components whereas γ_{S-G}^{nd} and γ_{L-G}^{nd} are non-dispersive ones.

Table 2.3 Surface tension and their components of water, and diiodomethane at 293 K from reference.[71,74,88]

Liquid	$\gamma_{L-G}(mN \cdot m^{-1})$	$\gamma_{L-G}^{d}(mN \cdot m^{-1})$	$\gamma_{L-G}^{nd}(mN \cdot m^{-1})$
Water	72.8	21.8	51.0
Diiodomethane	50.8	49.0	1.8

Using **Eq (14),** contact angles of water and diiodomethane from Table 2.2 and surface tensions from Table 2.3, the dispersive (γ_{S-G}^{d}) and non-dispersive components (γ_{S-G}^{nd}) of each solid

surface energy can be calculated. The surface energy is the summation of γ_{S-G}^{d} and γ_{S-G}^{nd}. The results of surface energies are summarized in Table 2.4**.**

Table 2.4 Surface energy and dispersive and non-dispersive components of different solid surfaces.

Solid	$\gamma_{S-G}(mN \cdot m^{-1})$	$\gamma_{S-G}^{d}(mN \cdot m^{-1})$	$\gamma_{S-G}^{nd}(mN \cdot m^{-1})$
$CaCO_3$	58.5	21.6	36.9
SiO_2	68.8	25.2	43.7
TiO_2	70.4	29.7	40.7
WO_3	71.6	31.6	40.0

According to Reference [89], the surface tension of solid metal oxide is not very sensitive to temperature and changes less than 5 $mN \cdot m^{-1}$ from 293 K to 423 K. Using **Eq (13)**, surface energies solid surfaces (γ_{S-G}) in Table 2.4 and contact angle of PS on the corresponding solid (θ_{S-L}) in Table 2.2, the interfacial energies between PS and ALD-modified surfaces are calculated and the results are plotted in Figure 2.6**.**

As seen, the interfacial energy between PS and the four different surfaces shows a strong correlation with the PS contact angles; WO_3 and PS has the least favorable interaction whereas that between $CaCO_3$ and PS is the most favorable among the four surfaces examined in this work. Interestingly, the water contact angle of these surfaces, which is often used to characterize their hydrophilicity, is an imperfect predictor for the PS contact angle and the PS-surface interfacial energy. These results indicate that caution must be exercised when predicting or estimating the strength of interactions between polymer and solid surface solely based on its reported hydrophilicity.

2.4 Conclusions

In this work we quantitatively characterize the strength of interactions between PS and ALD-modified pore surfaces by analyzing the capillary rise of PS into a disordered packing of 60 nm SiO_2 NPs using spectroscopic ellipsometry. Our study shows that ALD is a powerful technique to drastically change the wetting characteristics of nanoscale pores while minimizing the changes in the pore dimensions and structures. Sub-nanometer ALD layers can drastically convert the surface wetting characteristics and even sub-monolayer coverage can result in gradual changes in the wetting of PS on the pore surface. Among the four types of solid surfaces characterized in this work, $CaCO_3$ shows the strongest interactions with PS, whereas WO_3 exhibits least favorable interactions with PS. The contact angles of PS on solid surfaces and in turn the

interfacial energy between PS and ALD-modified pore surfaces provide important insights into how to control interactions between a molten polymer and a solid surface of porous media which have significant implications for fabricating nanocomposite films as well as for controlling transport and molecular contact between polymer and catalytic materials. Notably, the water contact angle on a surface is not a strong predictor of the strength of interactions between PS and the ALD-modified surfaces, thus caution must be exercised in deducing how polymers would wet solid surfaces and infiltrate pores merely based on the known hydrophilicity of the surface. The method introduced in this work also provides a robust method to characterize the interfacial tension between polymer and surfaces with complex compositions, and potentially will enable controlling the interactions between polymer and porous media for the fabrication of functional composites as well as controlling the catalytic conversion of polymers into useful chemicals.

CHAPTER 3. UNDERSTANDING POLYMER-POROUS SOLID INTERACTIONS BASED ON SMALL GAS MOLECULE ADSORPTION BEHAVIOR

Reproduced from Ren, T.; Wang, C. Y.; Huang, R.; Deng, C.; Xu, Y.; Majumder, A.; Ra, J.; Shen, K.; Vohs, J. M.; de Pablo, J. J.; Gorte, R. J.; Lee, D. Understanding Polymer-Porous Solid Interactions Based on Small Gas Molecule Adsorption Behavior. *Chem. Eng. J. 2023, 473* (August), 145220. https://doi.org/10.1016/j.cej.2023.145220.

3.1. Introduction

Understanding and controlling the interactions between molten polymers and porous inorganic solids bears significant importance for a number of processes and phenomena. For example, heterogeneously catalyzed reactions of polymers, such as hydrogenolysis of polyethylene, is considered to be a promising way to recycle and upcycle plastic wastes. [3–7] During such a process, polymer chains infiltrate into porous catalysts and subsequently undergo hydrogenolysis in contact with catalytically active sites. [8–10] The infiltration and transport of polymer chains in

nanoscale pores of catalysts likely play an important role in determining the reaction rate, reactivity and selectivity; slow infiltration could potentially lead to unnecessary side reactions and generate undesirable products such as gaseous molecules of low value. Infiltration of polymers into the pores of nanoparticle packings also has proven to be a versatile method of producing highly filled nanocomposite films with superb mechanical, thermal transport, and optical properties.[50,51,53,54,90] The strength of interactions between the polymer and nanoparticles plays a critical role in determining the infiltration rate as well as the fracture toughness of the resulting nanocomposite films.

Several techniques have been developed to measure and quantify the interactions between polymers and inorganic surfaces. One such method is the AFM-based single-molecule force spectroscopy (SMFS), which directly measures van der Waals (vdW) forces between a single polymer chain and a solid surface under high vacuum conditions.[91] The magnitude of the observed vdW forces is found to be dependent on the substrate species and the size of the repeat unit of the polymer, in agreement with theoretical predictions.[92] Another technique that has been used to determine the adhesion strength between a polymer and an inorganic surface is the Johnson-Kendall-Roberts (JKR) contact mechanics method. This method provides a way to infer the interfacial energy from the adhesion strength between the two materials. For polymers with low glass transition temperature (i.e., below room temperature), the sessile droplet contact angle measurement can be used to determine interfacial energy based on Young's equation. However, using these techniques to study the interactions between polymers and porous solids presents a challenge since most of these methods rely on planar surfaces for characterization. This

limitation highlights the need for new methods that can be employed to study the interactions between polymers and porous solids.

A recent study by some of us has shown that the contact angle and interfacial energy between molten polystyrene and various porous inorganic materials can be determined by measuring the time of capillary rise infiltration (CaRI) of the polymer into nanoporous packings of nanoparticles.[38] The surface of nanoparticles was modified using atomic layer deposition (ALD), which allows precise modification of pore surface without significantly affecting the pore geometry and size. Our work showed that the interactions between polystyrene and nanoporous solids can be changed dramatically by depositing sub-nanometer thick oxide layers via ALD. Although this previous study suggests that ALD is a powerful method of modifying the high surface materials to control the interactions between polymers and porous solids, the origin of such differences remains unclear. In fact, it remains unknown how to predict the strength of interactions between the two species based on the chemical structure of the polymer (or its repeat unit) and the surface chemistry of the porous inorganic solid.

In this study, we investigate the relationship between polymer-solid interfacial energy and the strength of interactions between small molecules and the porous solid. Given that a polymer chain consists of a large number of repeat units, we hypothesize that the interactions between a polymer and a porous solid will depend strongly on the strength of interactions between the solid surface and small molecules that resemble the repeat unit of the polymer. This approach can be particularly insightful given that the interactions between small molecules and high-surface-area porous solids can be readily characterized. However, it is also possible that the polymer-solid

interactions may be dominated by the entropic effect of large molecules whereas the small molecule-surface interactions by the enthalpic effects; and, thus, there may not exist a strong relationship between these two characteristics. We quantitively characterize the interactions between polymers and different porous solids using CaRI of two types of common polymers, polyethylene (PE) and polystyrene (PS), into a disordered packing of SiO_2 nanoparticles (NP) that is modified with atomic layer deposition (ALD). N-hexane and benzene are chosen as the representative small molecules for PE and PS, respectively. To accurately measure the strength of interactions of these small molecules with various oxide surfaces, we perform calorimetric measurements of the small molecules on the mesoporous SiO_2, SBA-15, before and after ALD modification. We find that the strong interaction between a polymer and different oxide surfaces (i.e., lower interfacial energy) correlates well with strong adsorption strength (i.e., higher heat of adsorption) of the representative small molecule. Our work provides a path to understanding polymer-solid interactions from a microscopic point of view based on the interactions between small gas molecules that bear a structural resemblance to the polymer and a solid surface. These findings have strong implications for designing catalysts that will favorably interact with polymer chains, potentially enabling enhanced reactivity or selectivity in polymer upcycling.

3.2. Material and Methods

3.2.1 Polymer Infiltration Study

Polystyrene (PS, molecular weight (MW) = 88,000 g/mol and polydispersity index (PDI) = 1.1) and polyethylene (PE, MW = 50,000 g/mol, PDI = 1.07) are purchased from Polymer Source

Inc. 61 nm silica (SiO_2) nanoparticle (NP) suspension (ST-YL, 30 wt % suspension in water) is generously provided by Nissan Chemical. A 2.2 wt% PE solution is made with decalin (Decahydronaphthalene, mixture of cis + trans, Sigma-Aldrich) and stirred for 2 hours at 443 K. A silicon wafer is cut into 10×10 mm^2 pieces and heated on a hot plate at 443 K for 2 minutes. A PE film is prepared by placing a drop of the heated PE solution and spin coating at 7,000 rpm for 30s. The thickness of PE films, determined using ellipsometry, is 115 ± 7 nm. PS films of 175 ± 3 nm; SiO_2 NP films of 223 ± 8 nm are prepared in the same way as described in our previous paper.[38] SiO_2 NP packings are subsequently modified with SiO_2, WO_3, TiO_2 and $CaCO_3$ using ALD. To deposit a polymer atop the NP layer, a polymer film is floated at an air-water interface by submerging a spin-coated film on a silicon wafer into water. The polymer film is transferred onto an ALD-treated silica nanoparticle film, which gives a very well-defined bilayer structure to perform the infiltration dynamics study.[38]

3.2.2 Atomic Layer Deposition (ALD)

Atomic layer deposition (ALD) of SiO_2, TiO_2, WO_3, and $CaCO_3$ on SiO_2 NP packings is performed using a home-built ALD system as described in detail previously. [38,93] TEOS, titanium tetrachloride ($TiCl_4$, Sigma-Aldrich, 99%), tungsten carbonyl ($W(CO)_6$, Strem Chemicals, 99 %), and bis(2,2,6,6-tetramethyl-3,5-heptanedionato)calcium ($Ca(TMHD)_2$, Strem Chemicals, 97%) are used as the Si, Ti, W, and Ca precursors, respectively. In a SiO_2 ALD cycle, the sample is evacuated then exposed to TEOS vapor at 523 K for 3 min, followed by oxidation at 773 K in air for 10 min. In a TiO_2 ALD cycle, the evacuated sample is exposed to $TiCl_4$ vapor at 423 K for 3 min, followed by evacuation and oxidation in humid air containing 10 % water at the same

temperature for 9 min. In a WO_3 ALD cycle, the evacuated sample is exposed to $W(CO)_6$ vapor at 473 K for 3 min, followed by evacuation and then oxidation at the same temperature in air for 6 min. In a $CaCO_3$ ALD cycle, the evacuated sample is exposed to $Ca(TMHD)_2$ vapor at 523 K for 10 min, followed by oxidation at 773 K in air for 10 min. ALD growth rates are measured using two methods: the mass gain of the bulk sample and the refractive index change of the NP films via spectroscopic ellipsometer. [38]

The ALD growth (Δh) can be estimated based on both the mass uptake (Δm) of the NP pellets and the refractive index increase (Δn) of NP thin films as our previous paper showed using Eq. (15) and Eq. (16):[38]

$$\Delta h = \frac{\Delta m \cdot \rho_{NP} \cdot R_{NP}}{3\rho_{ALD} \cdot m} \quad (15)$$

$$\Delta h' = \frac{R_{NP}}{3} \cdot \frac{\Delta n}{(n_{ALD} - n_{air})} \quad (16)$$

where ρ_{NP} is the density of silica; R_{NP} is the radius of silica NP; m is the mass of NP pellets; n_{ALD} and n_{air} are the refractive indices of the ALD-deposited material and air in room temperature, respectively.

3.2.3 High-Resolution Transmission Electron Microscopy and the Scanning Transmission Electron Microscope with Energy-Dispersive X-Ray Spectra Maps

The high-resolution transmission electron microscopy (HR-TEM) and the scanning transmission electron microscope (STEM) with energy dispersive X-ray spectra (EDS) maps are collected using a JEOL JEM-F200, operated at 200kV. The sample for microscopy study is first grounded to powder, then dispersed in ethanol and deposited on the carbon support on a copper grid from Electron Microscopy Sciences.

3.2.4 Capillary Rise Infiltration (CaRI)

Capillary rise infiltration (CaRI) is conducted at 423 K on a Linkam THMS350 V heating stage and monitored *in situ* using a J.A. Woollam Alpha-SE spectroscopic ellipsometry under N_2 environment. The analysis of the infiltration time is similar to our previous study.[38]

The infiltration time can be inferred by the change of refractive index of the NP film. The dynamic data of amplitude (Ψ) and phase difference (Δ) are fitted with a two-layer Cauchy model to obtain the refractive index. Figure 3.1 is an example of the dynamic data of PE infiltration into a 5-cycle TiO_2-ALD NP film. With an annealing rate of 30 K/min from room temperature at 293 K, it takes about 2.8 mins to reach the melting point of PE at 377 K where the infiltration starts. The 5-cycle TiO_2-ALD NP layer should have a refractive index of 1.38 but the initial fitting is 1.47 possibly due to the inhomogeneous interface between the PE film and the

NP film. After annealing to the melting point of PE at 377 K, the NP refractive index returns to 1.38. This is the point at which the infiltration of polymer into the pores of the NP packing starts. According to the change of the refractive index, it takes 56 mins (3,378 s) to finish the infiltration. The ending point for polymer infiltration is defined as a point that is different by less than 1% compared to the previous 5 data points.

All the infiltration times are obtained using the same method.

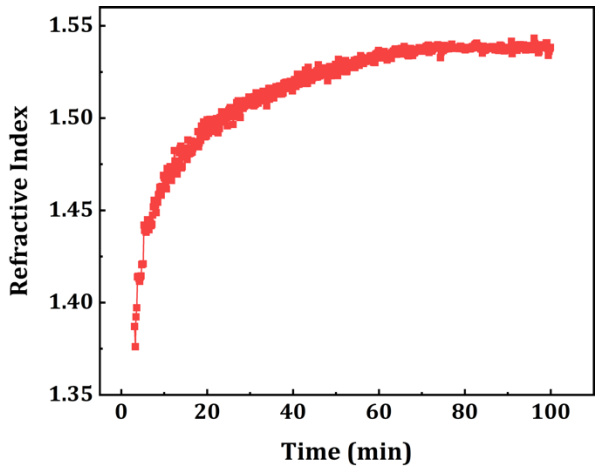

Figure 3.1 Representative data showing the changes of refractive index of NP film as a function of time for infiltration of PE into TiO2-ALD NP layer with a ALD thickness of 3.6 Å.

The contact angle and the interfacial energy of polymers on different solids are calculated based on the infiltration time.

The infiltration behavior is described by the Lucas-Washburn model (**Eq. (17)**) and the parameters are listed in the Table 3.1. [38]

$$h^2 = \frac{\gamma_{Polymer-G} \cdot R_{pore,SiO2} \cdot cos\theta}{4 \cdot \tau^2 \cdot \mu} t \quad (17)$$ [41,76]

Table 3.1 Parameters for Lucas-Washburn model.(Eq (17))

Polymer	NP radius, R_{NP} (nm)	Average pore size, R_{pore} (nm) [42,56]	Tortuosity, τ [42]	Molecular weight, M.W. (g/mol)	Polymer surface tension, $\gamma_{Polymer-G}$ ($mN \cdot m^{-1}$)	Polymer contact angle on SiO_2 surface, θ (°)	Height of capillary rise, h (nm)
PS	30	8.7	1.95	88,000	31.3 (423 K) [81]	20	220-230

PE	30	8.7	1.95	50,000(quoted as 82kDa but measured as 50kDa by HT-GPC)	28 (423 K) [94]	21	220-230

The average pore size is estimated as 0.289 of R_{NP} according to dense random packings [42]**.** The contact angle of PS (θ in **Eq. (17)**) on silica is regarded as 20 º based on different references [41,44]. The contact angle of PE (θ in **Eq. (17)**) on silica is measured in following method to be 21.2±4.8 º.

Spherical silica nanoparticles with very low dispersity are synthesized using the Stober solution method.[95] These nanoparticles have an average size of 135 ± 6 nm, verified via scanning electron microscopy (SEM) and dynamic light scattering (DLS). To measure the contact angle of polyethylene in silica, a previously reported method that determines the three-phase contact angle of nanoparticles trapped at the air-polymer interface is used.[96] Briefly, a sparse coating of the silica nanoparticles is made on a thin film (~450 nm in thickness) of polyethylene on a silicon substrate. Then the sample is heated at 323 K on a Linkam THMSEL350V heating stage for at least 48 h and up to 236 h to reach saturation value under N_2 purge. The heated sample is quickly quenched in liquid nitrogen. Then, the height, h, of the nanoparticle above the polymer-

air interface is measured by Bruker Icon atomic force microscopy (AFM) for 20+ nanoparticles. Finally, the polymer-silica contact angle is obtained by **Eq. (18)**:

$$\cos\theta = 1 - \frac{h}{R} \quad (18)$$

where R is the radius of the nanoparticle and θ is the polymer-solid equilibrium contact angle. The average particle size from DLS is slightly higher than the average size from SEM because DLS also measures an additional hydration layer around the particle. It is assumed that all particles have an average diameter of 135 nm and sensitivity analyses show negligible variation in contact angle for the two extremes of the size distribution obtained from SEM. The sample was heated on a heating stage at 150 ^{0}C inside a chamber for different amounts of time while constantly purging the chamber with N_2 gas. After almost 10 days of heating, the PE-SiO_2 contact angle equilibrates to a value of 21.2 ± 4.8°.

The infiltration data of the SiO_2 is used to calculate the viscosity of polymer μ under confinements. The ALD does not change the pore structure because the maximum coating thickness is all below 1 nm which is less than 10 % of the average pore size (R_{pore}). The contact angle (θ_{ALD}) of PS or PE on the ALD-coated surface is calculated using **Eq. (17)** from the infiltration time (t_{ALD}) obtained in by infiltration analysis and the parameters in Table 3.2.

Our previous paper reported the solid surface energies at 293 K by using the probe liquids of water and diiodomethane based on the Owens and Wendt method [38], and the surface energy of

the solid are listed in Table 3.2, column γ_{S-G}. The surface energy of solid metal oxide is not very sensitive to temperature and changes less than 5 mN·m^{-1} from 293 K to 423 K. [89]

Table 3.2 Surface energy for different solids.

Solid	γ_{S-G}**(mN·m^{-1}) at 293 K**
SiO_2	68.8
TiO_2	70.4
WO_3	71.6
$CaCO_3$	58.5

$$\gamma_{S-L} = \gamma_{S-G} - \gamma_{L-G} \cdot \cos(\theta_{S-L}) \quad (19)$$

With Young's equation (**Eq. (19)**), the interfacial energy between polymer and solids γ_{S-L} can be calculated with the γ_{S-L} in Table 3.2, $\gamma_{Polymer-G}$ in Table 3.1, and θ_{S-L} obtained from **Eq. (19)**.

Sensitivity analysis shows that the contact angle of PE on SiO_2 ranging from 0 to 30 º changes less than 1 % of the calculated values of contact angle and interfacial energy on other solids.

3.2.5 SBA-15 Synthesis and Characterization

SBA-15 is synthesized following a process reported in the literature.[97] 4.0 g of Pluronic P-123 is initially dissolved in 120 g of 2 M HCl solution and 30 g of deionized water with stirring at 298 K. 8.5 g of tetraethoxysilane (TEOS, Sigma-Aldrich, 99%) is then added dropwise with stirring at 308 K, followed by stirring at this temperature for 20 h. The solution is then maintained at 373 K for hydrothermal treatment for 24 h. The resulting sample is filtered, washed with deionized water, and dried at 353 K for 8 h in air. To remove P-123, the sample is calcined in flowing air at 773 K for 6 h with a ramping rate of 1 K/min. Our previous results demonstrated that metal oxides can be uniformly deposited on SBA-15 support.[98] ALD of SiO_2, TiO_2, and $CaCO_3$ on SBA-15 is performed using the same ALD equipment and procedures as described above for the SiO_2 NP films. For ALD of WO_3, SBA-15 is first treated with piranha solution (H_2SO_4:H_2O_2=3:1) for 30 min to form silanol groups for anchoring of WO_3 in the pores of SBA-15. N_2 adsorption-desorption isotherms are measured at 78 K using a Micromeritics, TriStar II Plus surface area and porosity analyzer. For these measurements, the samples are pretreated at 573 K under evacuation. Surface areas are determined using the BET method and pore-size distributions are determined from the adsorption isotherms using the Barrett-Joyner-Halenda (BJH) method.

3.2.6 Heat of Adsorption Measurement Using Calorimetry

A home-built Calvet calorimeter is used to measure the heats of adsorption of hexane and benzene on solid surfaces and has been described in detail elsewhere.[99,100] A schematic diagram of the calorimeter is shown in Figure 3.2.

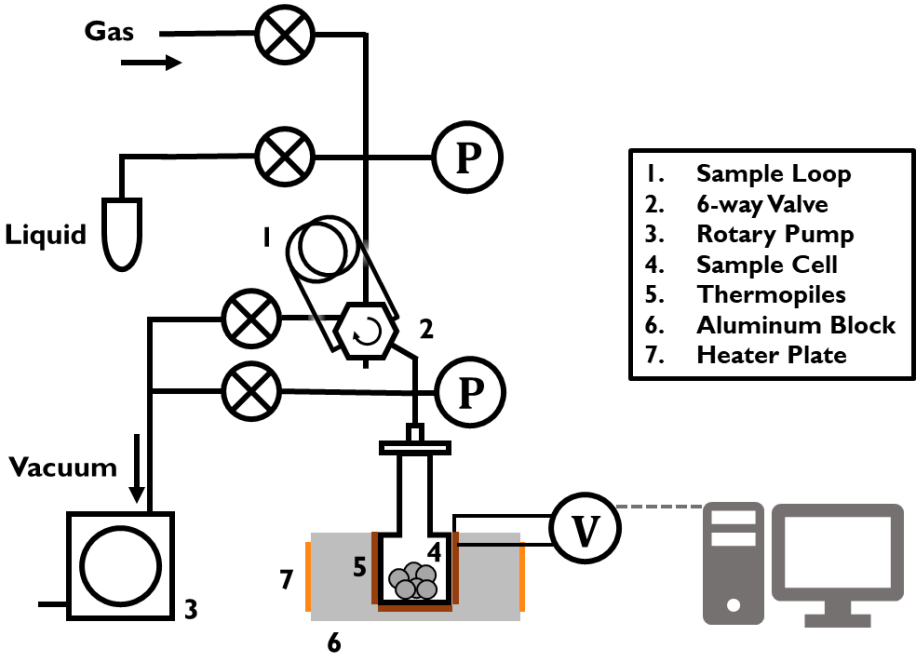

Figure 3.2 A schematic diagram of the home-built Calvet calorimeter.

The calorimeter consists of two parts, dosing section and heat flow section. The dosing section is constructed using valves, pressure transducers and a vacuum pump. A 6-way valve is used to introduce the adsorbate molecules from the gas chromatography (GC) sample loop to the sample cell. The amount adsorbed is determined by the difference between the number of molecules admitted and the number of molecules remaining in the gas phase in the dead volume of the

sample cell at equilibrium. The heat flow section is used to measure the heat flux from the sample cell made of a Pyrex glass cube. Five, 2.54 cm^2, thermal flux meters/thermopiles (International Thermal Instrument Company, INC, Del Mar, CA, USA) connected in series are placed between the sample cell and a large aluminum block which serves as a heat sink for rapid heat dissipation and small temperature changes. The aluminum block is placed in a Styrofoam container. Thermally conductive compound (DOWSIL340 silicone heat sink compound, the Dow Chemical Company, USA) is pasted onto the surfaces of the sample cell, thermopiles and the aluminum block to facilitate heat transfer. Six heating plates (Icstation, Guangdong, China) are attached to the outside walls of the aluminum block to heat up the aluminum block. The power is provided by a controllable DC power supply (Model 1688B, B&K Precision, Yorba Linda, CA, USA). The aluminum block temperature is measured by an adhesive K-Type surface thermocouple that is attached on the center of the top surface of the aluminum block. The voltage signal from the thermopiles, which is proportional to the heat flux, is recorded by a computer. The total heat released during the adsorption process is obtained by numerical integration with respect to time.

In a typical measurement, a sample of ~ 0.5 g, pressed into pellets, is loaded to the sample cell through the 0.5-inch-OD glass tube. Next, a layer of quartz chip is loaded to cover the sample to prevent heat losses from radiation. The sample is evacuated by a mechanical pump and heated at 573 K for 1 h to remove adsorbed water. After cooling to room temperature, the sample cell is inserted into the aluminum block, with a copper box as the lid. The sample cell, thermopiles, aluminum block, and copper box are all located in the Styrofoam container. The aluminum block

is heated to 358 ± 1 K by the heater plates. The experimental temperature is chosen at 358K to obtain reasonable adsorbate coverages at the atmosphere pressure. Furthermore, since adsorption enthalpies are weakly dependent on temperature, the discrepancy in measurement temperatures would not vary our conclusions.

After the temperature is stabilized, the samples are exposed to the gas from the GC sample loop and the heat flux is recorded. n-Hexane and benzene-are used as the adsorbates in this study. After collecting the data in an adsorption process, the sample is evacuated and the next set of data is collected, which ensures both the reversibility of the adsorption and the reproducibility of the data.

The calibration constant for the instrument was measured previously by passing current through a Pt wire placed between the sample cell and the thermopiles.[101] The calibration was confirmed in the present work by measuring the isosteric heat of adsorption for propane on H-ZSM5(280), which previous studies have shown is 40 kJ/mol and essentially independent of coverage.[99] To avoid chromatographic adsorption and to ensure adsorbates are able to approach all possible sites, all the calorimetric measurements are performed at an elevated temperature where adsorption is reversible by evacuation.

H-ZSM-5 is used for the calibration of calorimetry. The commercial ZSM-5 samples (CBV 28014, Si/Al_2 molar ratio = 280, Zeolyst International) in the ammonium-ion form is calcined in air at 773 K for 4 hours and converted to the acidic form as H-ZSM-5. The surface area of H-ZSM-5 is not well defined, so the surface area of 400 m^2/g given by the company is used.

3.2.7 Coarse-Grained (CG) Simulation of Solid-Liquid Interfaces: CG Model and Interaction Parameters

The solid substrate and the simple liquid are represented by spherical beads, denoted as type S and type L, respectively. The mass of each bead, m_S and m_L, is 1.0 in dimensionless units. The polymer chain connectivity is modeled using the bead spring model[102], where the type L beads within a polymer chain are connected by the finitely extensible nonlinear elastic (FENE) bonds. The parameters for the FENE bond potential are $R_0 = 1.50\ \sigma$, K = 30, $\varepsilon_b = 1.0$, and $\sigma_b = 1.0\ \sigma$, where σ is the dimensionless length unit. Chain stiffness is controlled by the harmonic bond-bending potential. While the bond angle is maintained at 180°, the bending spring constant k_a is set to 2 to represent a flexible chain, and 10 to represent a relatively rigid chain. The beads interact with one another through the Lennard-Jones potential with a cutoff radius of 2.5σ and a smooth decay starting at 2.4 σ. As summarized in Table 3.3, the LJ parameters are σ_{SS}=1.0 σ and ε_{SS}=2.0 for two type S beads, σ_{LL}=1.0 σ and ε_{LL}=1.0 for two type L beads. For the LJ interaction between type S and type L beads, σ_{SL} is maintained at 1.0 σ, while ε_{SL} is varied from 0.4 to 0.9 in increments of 0.1 to model the different adsorption strength. The LJ nonbonded potential is turned off for beads connected by one or two consecutive bonds. The simulation is performed using the Large-Scale Atomic/Molecular Massively Parallel Simulator (LAMMPS) package[103]

The pairwise Lennard-Jones (LJ) nonbonded interaction is in the form:

$$E(r_{ij}) = 4\varepsilon_{ij}\left[\left(\frac{\sigma_{ij}}{r_{ij}}\right)^{12} - \left(\frac{\sigma_{ij}}{r_{ij}}\right)^{6}\right], \quad (20)$$

where r_{ij} is the separation distance between atoms i and j, σ_{ij} is the Lennard-Jones diameter, and ε_{ij} is the Lennard-Jones interaction strength. See below for the LJ parameters.

Table 3.3 Nonbonded interaction potential parameters for polymer atoms.

Pair	σ_{ij}	ϵ_{ij}
S-S	1.0	2.0
S-L	1.0	0.4, 0.5, 0.6, 0.7, 0.8, 0.9
L-L	1.0	1.0

The finitely extensible nonlinear elastic (FENE) bonds[102] takes the form

$$E = -0.5KR_0^2 \ln\left[1 - \left(\frac{r}{R_0}\right)^2\right] + 4\varepsilon_b\left[\left(\frac{\sigma_b}{r_{ij}}\right)^{12} - \left(\frac{\sigma_b}{r_{ij}}\right)^{6}\right] + \varepsilon_b, \quad (21)$$

where K=30, R_0=1.5, σ_b=1 σ, and ε_b=1. R_0 is the maximum extensible bond distance. The first attractive term is balanced by the second LJ repulsive term, giving an equilibrium bond distance of 1 σ, which equals the LJ diameter of the type L bead. A harmonic bending potential is applied to 1-2-3 bonded beads in the form:

$$E_{bend}(\theta_{ijk}) = k_a(\theta_{ijk} - {\theta_{ijk}}^{(0)})^2, \quad (22)$$

Where k_a is the spring constant, θ_{ijk} is the angle between beads i, j, and k, and ${\theta_{ijk}}^{(0)}$=180° is the equilibrium bond angle. Chain stiffness increases with k_a.

3.2.8 Coarse-Grained (CG) Simulation Protocol

The simulation is performed using the Large-Scale Atomic/Molecular Massively Parallel Simulator (LAMMPS) package[103]. For each simulation, an empty, elongated simulation box is first initiated with a dimension 16 σ × 16 σ in the plane of the substrate (x̂–ŷ) and 36 σ along the substrate normal ($\hat{z}$). Then, substrate beads and the liquid molecules are inserted into the bottom and top halves of the simulation box, respectively. Each system contains 1000 substrate beads and 2000 liquid beads. This means that for chain molecules of length N = 20, the system contains 100 chains. The system first undergoes a short relaxation under the NVT ensemble for 5×10^4 steps at T=1.0, t_{damp} = 100 timesteps. The system is then equilibrated under the NPT ensemble for 2×10^6 at T=1.0 to ensure that the equilibrium density is achieved. The barostat is applied along $\hat{z}$ direction at $P_{\hat{z}}$ = 0.05, t_{damp} = 1000 timesteps. The production run is carried out under the NVT ensembled at T= 1.0 for 5×10^6 timesteps. The simulations are integrated using the velocity-Verlet algorithm with the integration time step is 0.001 τ, where τ is the derived LJ unit for time.

3.2.9 Coarse-Grained (CG) Calculation of Interfacial Tension

This study employs the test-area (TA) perturbation method[104,105] to determine the interfacial tension. This method applies test changes in the interfacial area, then derives the interfacial tension from the free-energy perturbations caused by the area change. Relevant equations and details are described in the following paragraphs. The magnitude of the perturbation is expressed as $\Delta A^* = \Delta A/A_0$, where ΔA is the area change, and A_0 is the interfacial area. To check for hysteresis and robustness, each calculation is repeated at three different perturbation magnitudes in both directions of perturbation: $\Delta A^* = \pm 0.001, \pm 0.004$, and ± 0.005. Figure 3.3 shows that the collected trajectory is sufficient for the calculation to converge.

The interfacial tension is estimated by **Eq(21)**.

$$\gamma = \lim_{\Delta A \to 0} \left(\frac{\Delta F_{0\to 1}}{\Delta A}\right)_{N,V,T} = -\frac{kT}{\Delta A} \ln\langle \exp\left(-\Delta U/kT\right)\rangle_0, \quad (21)$$

where ΔA is the test area change. $\Delta F_{0\to 1}$ is the perturbation in Helmholtz free energy of the system due to the area change. $(\ldots)_{N,V,T}$ denotes that the calculation is performed under the NVT ensemble. ΔU is the change in potential energy due to the area change. $\langle \ldots \rangle_0$ denotes that an ensemble average of the excess Boltzmann factor over the configuration space of the initial trajectory. In LJ unit, kT=1.

Running estimates of interfacial tension are plotted below a function of integration time, using the flexible chain (N=20, ka=2) as an example. As indicated by the legend in Figure 3.3, the calculation at each ε_{SL} is repeated at three different perturbation magnitudes in both directions of

perturbation: $\Delta A^* = \pm 0.001, \pm 0.004$, and ± 0.005. The overlapped result indicate that the running estimates stabilize by the first half of the simulation time and are invariant of the direction and magnitude of the perturbation.

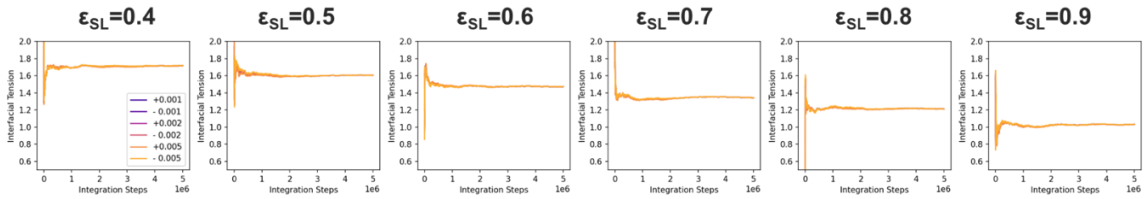

Figure 3.3 Running estimates of interfacial tension as a function of integration steps for ε_{SL} ranging between 0.4 and 0.9.

3.2.10 Density Functional Theory (DFT) Calculation of Adsorption Energies

Periodic $CaCO_3$ and amorphous silica models are used in the analysis of the adsorption energy of benzene and alkane molecules. A gaseous ethane molecule is chosen to represent the alkane molecules. The unit cell of the $CaCO_3(100)$ slab model has an area of 10.0 Å × 16.2 Å and contains 24 $CaCO_3$ units shown in Figure 3.4 (a). Given the pristine $CaCO_3(100)$ model, a defected slab is also considered, where a $CaCO_3$ unit is eliminated, and the surface is optimized using DFT, resulting in an undercoordinated Ca^{2+} ion shown in Figure 3.4 (b).

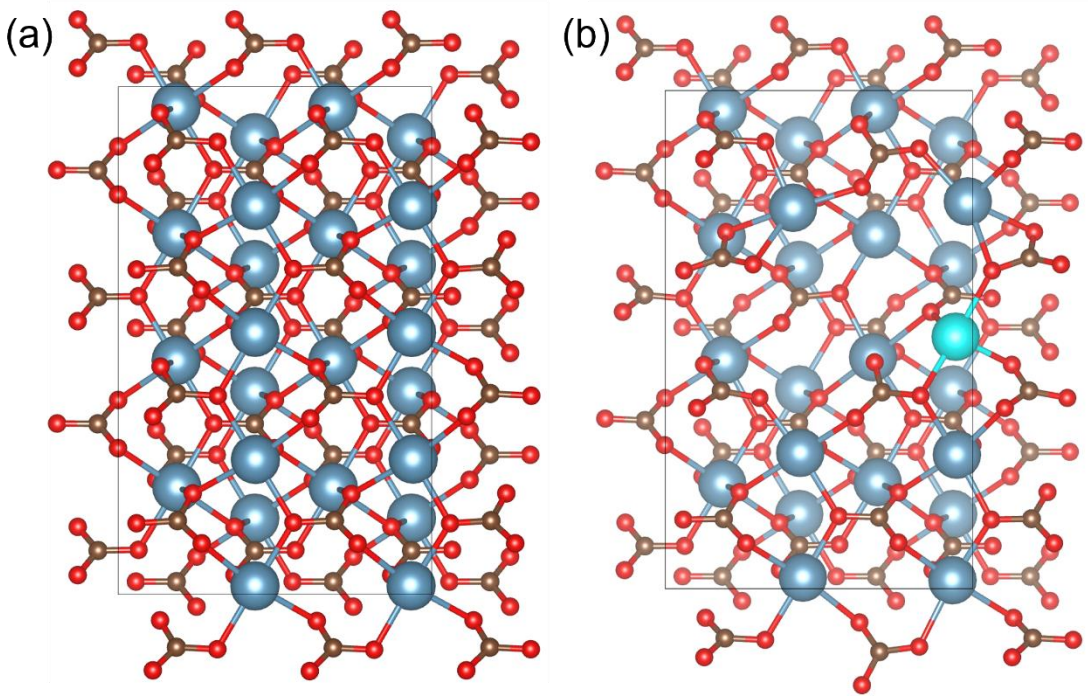

Figure 3.4 Top view of the $CaCO_3$ slab models: (a) a pristine $CaCO_3$(100) surface and (b) a defected $CaCO_3$(100) surface where a $CaCO_3$ unit is eliminated, followed by the DFT optimization; such treatment results in an undercoordinated Ca ion. (marked as light blue) (

The amorphous silica model was originally generated by Comas-Vives and coworkers,[106] which has been employed in multiple computational catalysis works.[107–109] The model contains 106 SiO_2 units with a unit cell size of 21.4 Å × 21.4 Å × 34.2 Å shown in Figure 3.5**.** The amorphous property originates from an annealing process, followed by dehydration steps to produce a silanol density consistent with the environmental temperature and partial pressure of water (1.1 OH nm^{-2}). As seen in Figure 3.5**.**, various surface features are found on the amorphous

silica model, including hydroxyl (Si-OH) moieties and siloxane rings forming cavities with various sizes. Given the surface models, we place the gaseous molecules on the surfaces of both $CaCO_3$ and silica and perform DFT optimizations to determine the adsorption energy (E_{ads}). E_{ads} is obtained through the equation: $E_{ads} = E_{total} - E_{surface} - E_{gas}$, where E_{total}, $E_{surface}$, and E_{gas} are the total energy, the energy of empty surface, and the energy of a gaseous molecule, respectively.

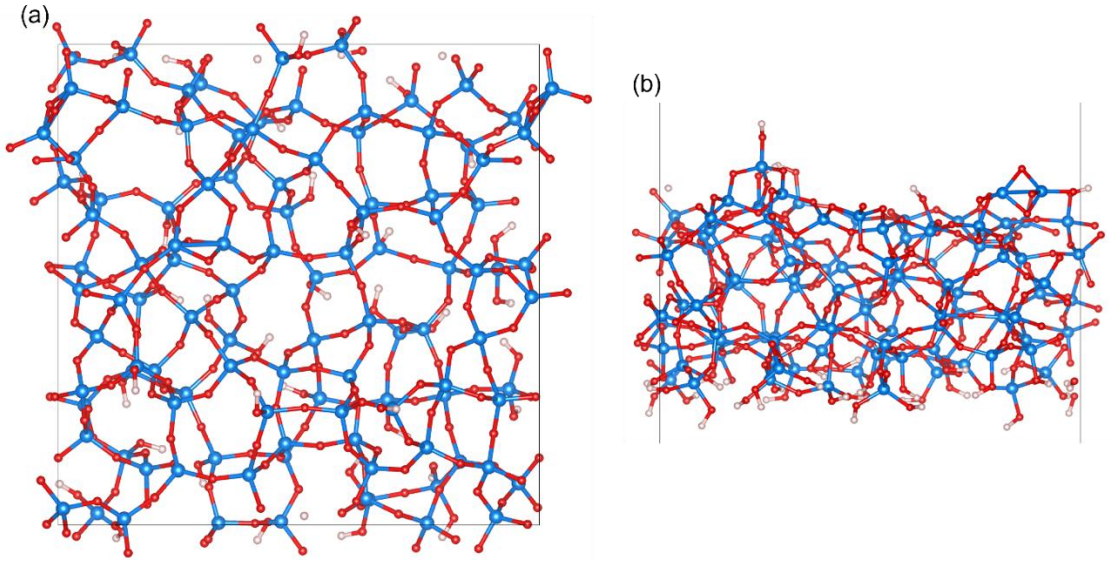

Figure 3.5 Top (a) and side view (b) of the amorphous silica slab model. (Si: blue, O: red, H: white)

All periodic DFT calculations are performed using Vienna Ab-initio Simulation Package (VASP, 6.2.1),[110–113] where planewave basis sets describe the Kohn-Sham orbitals, and the Kahn-Sham equations are solved self-consistently. The BEEF-vdw exchange-correlation functional using projector augmented wave (PAW) pseudopotentials was employed in all DFT calculations.[114–116]

The *k* point grids of 2 × 2 × 1 and 3 × 2 × 1 are used in the calculations of silica and $CaCO_3$ surfaces, respectively, and a cutoff energy of 400 eV are used in all simulations. The energy convergence criterion for completing a geometric step is 10^{-4} eV, and the force convergence criterion of 0.02 eV $Å^{-1}$ is considered.

3.3. Results

3.3.1 Determination of Polymer-Porous Solid Interfacial Energy

To characterize the interactions between polymers and porous solids, we measure the time of infiltration of polymers into the packing of silica nanoparticles. In our recent study, we have shown that the interfacial energy as well as the contact angle between a molten polymer and a porous solid can be inferred from the infiltration time. Polystyrene (PS) and polyethylene (PE), common polymers with different structures and properties, are chosen as the model polymers. To study the effect of surface chemistry, we measure the time of infiltration to fully fill the ~225 nm thick disordered packings of 61 nm SiO_2 nanoparticles that are modified via atomic layer deposition (ALD) using spectroscopic ellipsometry as shown in Figure 3.6. The infiltration time increases gradually to an asymptotic value as the thickness of the ALD metal oxide layer is increased. For example, the infiltration time for PE into TiO_2 ALD-treated NP (Figure 3.6 (a), □) films increases with the ALD thickness of TiO_2. This indicates that PE wets the TiO_2 surface less favorably compared to the SiO_2 surface. The infiltration time reaches a saturated value of ~350 s after depositing 0.35 nm TiO_2, which is consistent with the previously reported value 0.35 nm for a TiO_2 monolayer. [83] The thickness at which the infiltration time shows saturation for WO_3 and

$CaCO_3$ are 0.75 nm and 0.43 nm respectively, which also agree with the reported values for the thickness of WO_3 and $CaCO_3$ monolayers (0.8 nm and 0.4 nm). [84,117] HR-TEM and STEM coupled with EDS are used to characterize the growth of TiO_2, WO_3, $CaCO_3$, and SiO_2 on SiO_2 NPs, as shown in Figure 3.7. The observations reveal the occurrence of a ring localized at the periphery of each individual NP and no distinct signal is identified at the central region of the NPs. This suggests the application of ALD yields an ultrathin and uniform coating, characterized by the absence of prominent crystalline features.

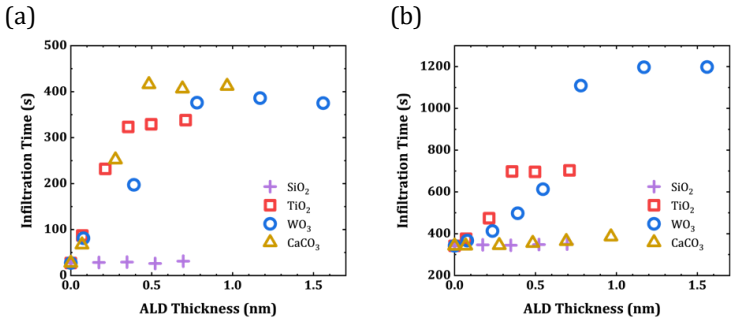

Figure 3.6 Infiltration time of (a) PE, and (b) PS at 423K on ALD-modified surfaces as a function of the ALD thickness.

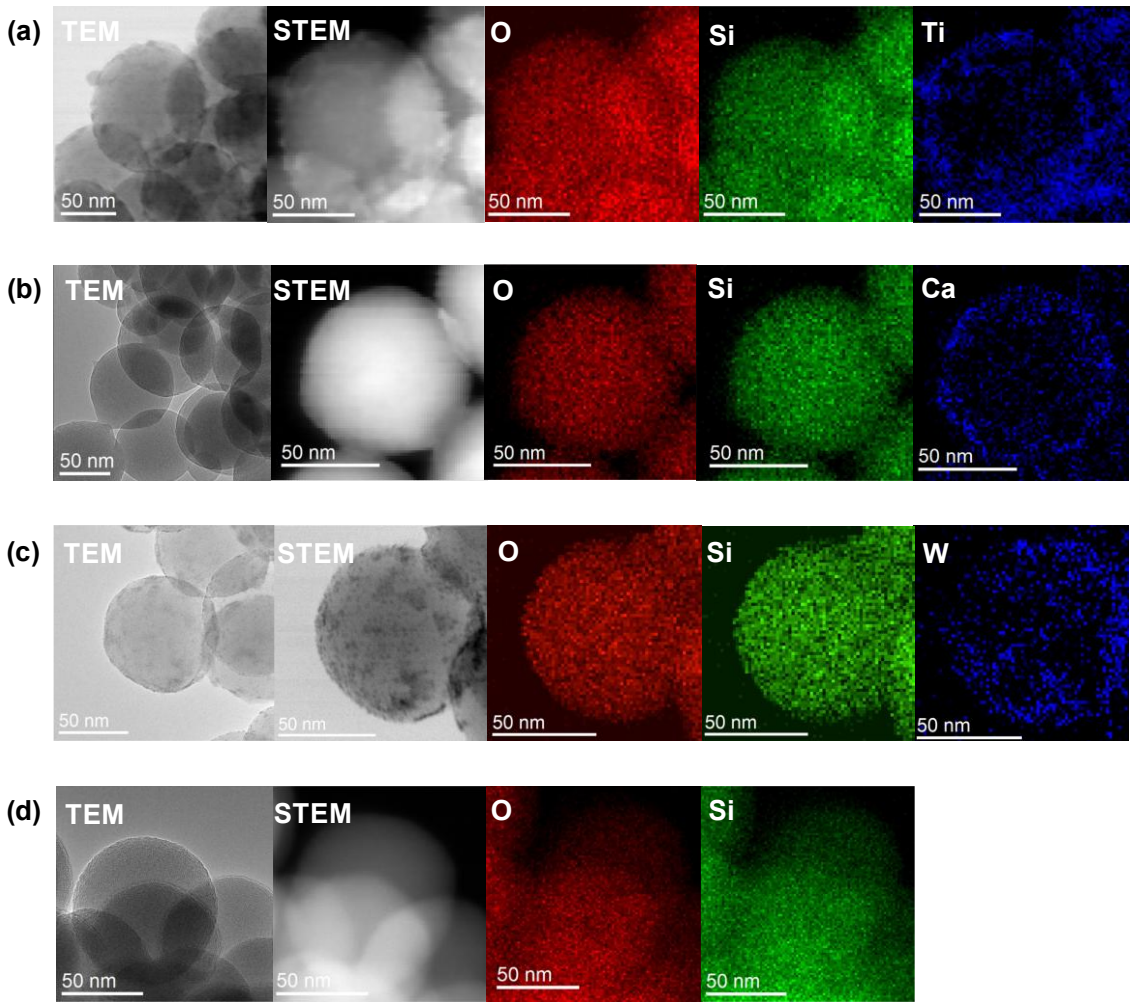

Figure 3.7 Representative TEM, STEM, and EDS maps of (a) TiO_2, (b) $CaCO_3$, (c) WO_3, and (d) SiO_2 on SiO_2 NP.

As shown in Figure 3.6 (b), the infiltration of PS shows similar patterns. The fact that the infiltration time of PS saturates at the same ALD thickness as PE confirms that the SiO_2 surface is completely covered with the oxide layer via ALD at these thicknesses. It is worth mentioning that depositing SiO_2 onto the SiO_2 NP packing does not change the infiltration time of PE or PS (Figure 3.6, +). Considering a monolayer of SiO_2 is ~0.25 nm, the SiO_2 NP packings modified

with 3 monolayers of SiO_2 show the same infiltration time as the pristine NP film. [118] This implies that the SiO_2 layer prepared via ALD has similar wetting properties as pristine SiO_2 nanoparticles.

The infiltration time provides an important insight into the strength of interactions between polymers and the oxide surfaces. For a given polymer, more favorable wetting leads to a faster infiltration rate and thus a shorter infiltration time. While the infiltration time provides a qualitative measure of the interactions between polymer and solid, the interfacial energy is a direct measure of the strength of the polymer-solid surface interactions. The interfacial energies (γ), calculated from the infiltration time in Figure 3.6 using the method we have previously reported, are displayed in Figure 3.8**.** For PE, SiO_2 shows the lowest interfacial energy, which is consistent with the shortest infiltration time as shown in Figure 3.6 (a). TiO_2, WO_3, and $CaCO_3$ show similar interfacial energies with PE. Although $\gamma_{PE\text{-}CaCO3}$ is the smallest among these three, the infiltration time of PE in $CaCO_3$ is not the shortest because $CaCO_3$ has a lower solid-air interfacial energy among the four materials including SiO_2 as shown in Table 3.2 [38]. It is interesting that for all four types of surfaces we investigate, PS has lower interfacial energies than PE, implying that PS wets these surfaces more favorably than PE.

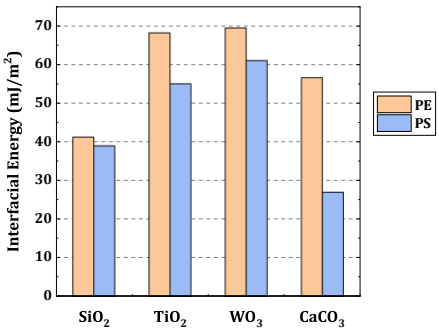

Figure 3.8 Interfacial energies between different surfaces prepared via ALD and polymer: PE is plotted in orange, and PS is in blue.

3.3.2 Determination of Heat of Adsorption of Small Molecules on Porous Solids

To test how the interactions of small molecules and porous solids correlate with the polymer-solid surface interactions, we measure the heat of adsorption of hexane and benzene in mesoporous silica. While it is straightforward to produce disordered films of SiO_2 nanoparticles via spin coating, producing bulk samples of SiO_2 nanoparticle packings is challenging due to cracks and defects that form during preparation. Therefore, the silica NP packing for the polymer infiltration measurements has a range of pore sizes. Because SBA-15 has uniform well-defined pores, we use this material for our calorimetry measurements. To prepare porous silica with well-defined nanopores, we produce SBA-15 mesoporous materials and modify their surfaces via ALD. The amount of TiO_2, WO_3, $CaCO_3$, and SiO_2 deposited on the SBA-15 support is determined gravimetrically. The growth rates are in reasonable agreement with the previous literature values of ALD growth rate on SBA-15, where the sample masses increase linearly with the number of ALD cycles for all oxides deposited. Based on the mass changes, the growth rates are calculated to be 5.2×10^{17} Ti atoms$\cdot m^{-2}\cdot cycle^{-1}$, 1.8×10^{17} W atoms$\cdot m^{-2}\cdot cycle^{-1}$, 3.1×10^{17} Ca atoms$\cdot m^{-2}\cdot cycle^{-1}$, and 4.2×10^{17} Si atoms$\cdot m^{-2}\cdot cycle^{-1}$ shown in Figure 3.9.[67,73,97,119] Physical properties of SBA-15 modified with ALD are summarized in Table 3.4.

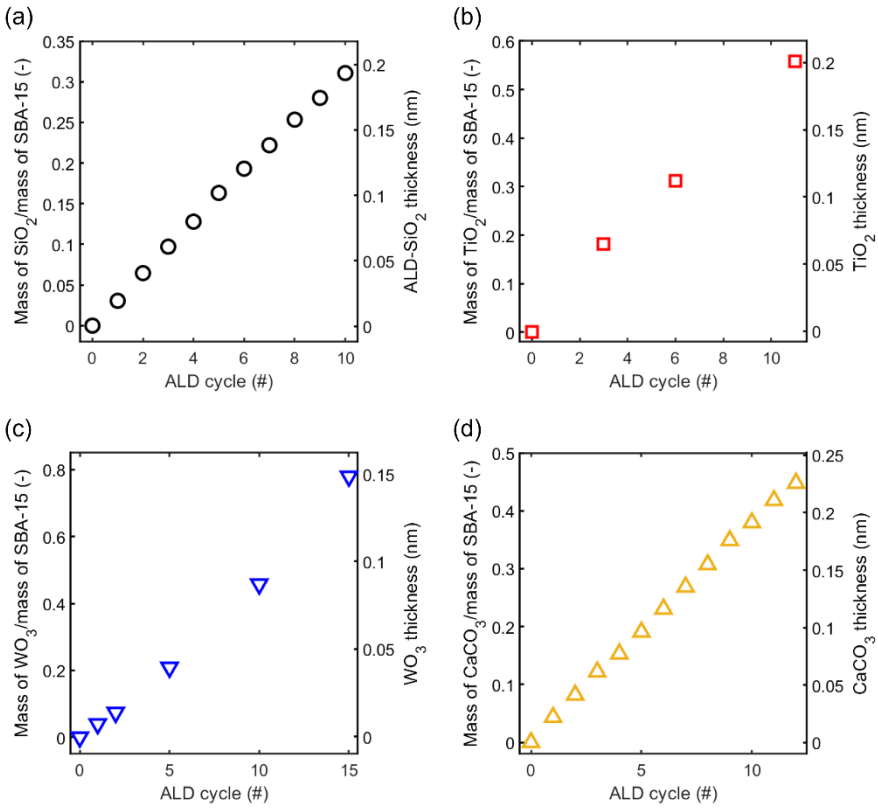

Figure 3.9 Mass and film thickness growth of (a) SiO_2, (b) TiO_2, (c) WO_3, and (d) $CaCO_3$ as a function of ALD cycles on SBA-15.

Table 3.4 Properties of SBA-15 modified with ALD. The film thickness of oxides is calculated based on the bulk density of the oxides.

Samples	**BET Surface Area (m^2/g)**	**Film Thickness (nm)**	**Composition by Weight**	**Surface Density ($atom/m^2$)**	**# of ALD cycles**

SBA-15	733	-	-	-	-
SiO_2/SBA-15	457	0.19	ALD-SiO_2: 24%	-	10
TiO_2/SBA-15	466	0.20	TiO_2: 35%	5.8×10^{18} Ti	11
WO_3/SBA-15	326	0.15	WO_3: 44%	2.8×10^{18} W	15
$CaCO_3$/SBA-15	255	0.23	$CaCO_3$: 32%	3.7×10^{18} Ca	12

Figure 3.10 (a) and Figure 3.10 (b) show the N_2 adsorption-desorption isotherms and the pore size distributions of the ALD-modified SBA-15. The SBA-15 presents a hysteresis loop in the isotherm and has a unimodal pore size distribution centered at 9.5 nm which is comparable to the average pore size of the SiO_2 nanoparticle packings used in this study. The hysteresis loop indicates the predominance of well-defined cylindrical pores. After ALD of SiO_2, TiO_2, and $CaCO_3$, similar hysteresis loops are observed in the isotherms, implying that SiO_2, TiO_2, and $CaCO_3$ deposited as conformal films in SBA-15, decreasing the pore size but without changing the cylindrical pore structure. As shown in Figure 3.10 (b), the pore sizes decrease from 9.5 nm to 8.5 nm for SiO_2/SBA-15, 8.7 nm for TiO_2/SBA-15, 9.2 nm for WO_3/SBA-15, and 8.1 nm for $CaCO_3$/SBA-15.

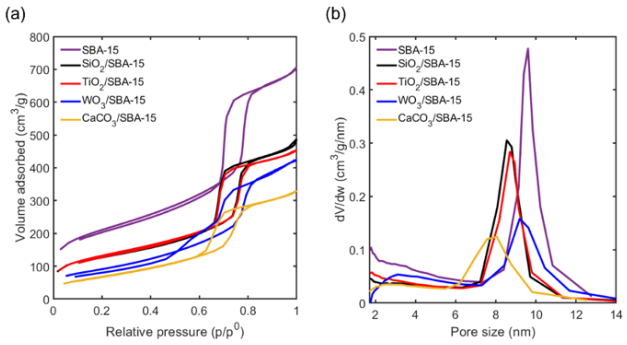

Figure 3.10 (a) N_2 adsorption-desorption isotherms and (b) pore size distributions for SBA-15, SiO_2/SBA-15, TiO_2/SBA-15, WO_3/SBA-15, and $CaCO_3$/SBA-15.

Hexane is chosen as the representative small molecule for PE. The differential heats of adsorption of hexane on pristine SBA-15, and ALD-modified SBA-15 are shown in Figure 3.11. In all four types of materials examined in this study, the heat of adsorption decreases with increasing adsorbate coverage.

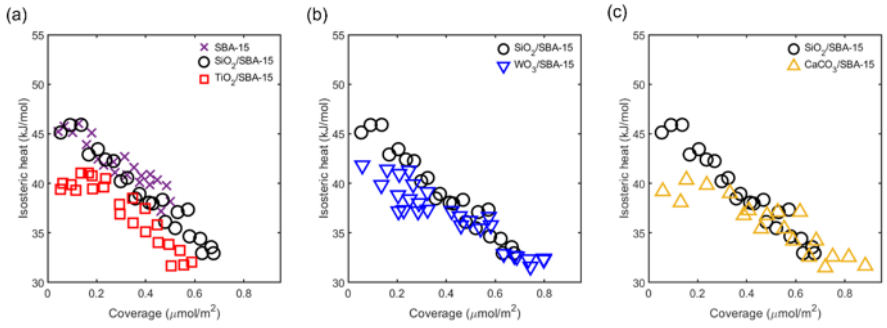

Figure 3.11 Differential heats of adsorption of n-hexane on (a) SBA-15, SiO_2/SBA-15, and TiO_2/SBA-15, (b) WO_3/SBA-15, and (c) $CaCO_3$/SBA-15.

The temperature-programmed desorption shown in Figure 3.12 of 2-propnaol on SBA-15 before and after piranha solution treatment and sample of WO_3/SBA-15 show change of surface chemistry. Since differential heats for propane adsorption on ZSM-5(280) were constant shown in Figure 3.13, the decreasing heats reflect the energetically heterogeneous nature of the solid surfaces and are not an artifact of the experimental technique.

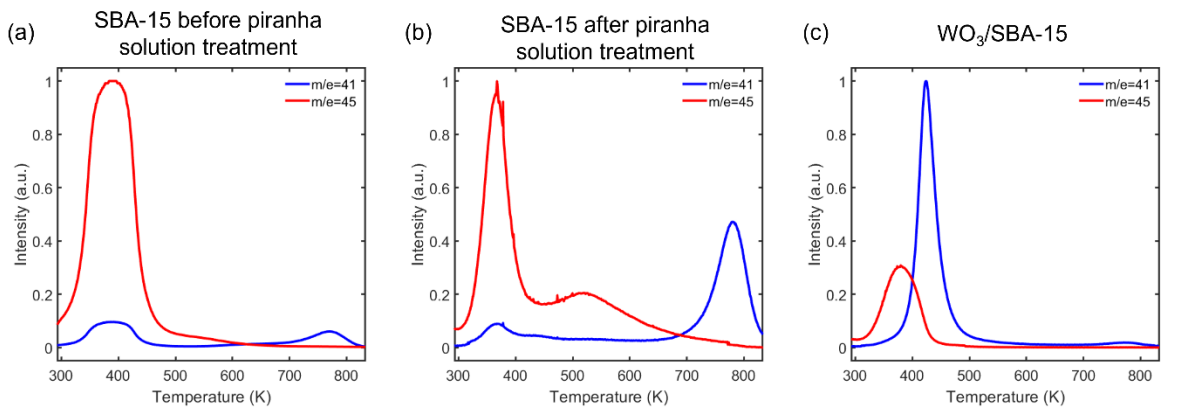

Figure 3.12 Temperature-programmed desorption of 2-propnaol on SBA-15 before and after piranha solution treatment and WO_3/SBA-15. m/e=41: propene; m/e=45: 2-propanol.

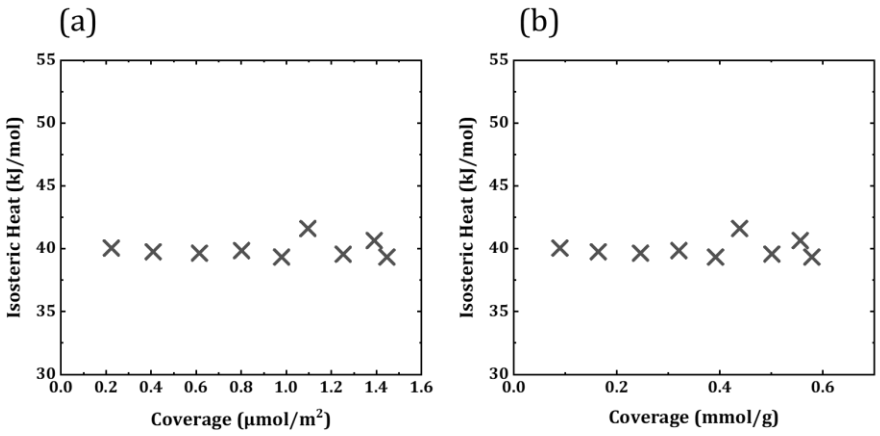

Figure 3.13 Differential heats of adsorption of propane on H-ZSM5.

The curves of SBA-15 and SiO_2/SBA-15, as shown in Figure 3.11 (a), overlap, implying that the pore-size changes from ALD have little effect on the heat of adsorption. In contrast, the heats of adsorption on the TiO_2-modified SBA-15 are reduced by ~ 5 kJ/mol compared to that on SiO_2, indicating that hexane has weaker interactions with TiO_2 compared to SiO_2. Results for WO_3/SBA-15, displayed in Figure 3.11 (b), show the heat of adsorption is ~ 5 kJ/mol lower compared to that for SiO_2/SBA-15. The isosteric heat of $CaCO_3$/SBA-15 is ~ 6 kJ/mol lower compared to that for SiO_2 in the low coverage region (< 0.2 μmol n-hexane/m^2), while overlapping with the SiO_2 at higher coverage, as shown in Figure 3.11 (c).

The heats of adsorption for n-hexane agree well with the polymer infiltration times shown in Figure 3.6 and the polymer-solid interfacial energies shown in Figure 3.8. Additional ALD modification beyond the complete monolayer coverage does not change the heat of adsorption and the infiltration time. These observations indicate that the heat of adsorption[101,120,121] and the polymer infiltration[44] are not strongly affected by small differences in the pore size. TiO_2, WO_3, and $CaCO_3$ show a lower heat of adsorption for n-hexane than SiO_2 implying that interactions between n-hexane and these three ALD materials is weaker than that between n-hexane and SiO_2. More importantly, these trends are consistent with the interfacial energy between the polymer and solids. The interfacial energy between PE and TiO_2, WO_3, or $CaCO_3$ is greater than that between PE and SiO_2.

Benzene is chosen as the representative small molecule for PS, which has a phenyl group in each repeat unit. As shown in Figure 3.14 (a), the heats of adsorption for benzene in SiO_2/SBA-15 overlap with that in SBA-15, confirming again that the addition of SiO_2 by ALD does not affect benzene adsorption in SBA-15. Moreover, the heats of adsorption for benzene on TiO_2 films are lower than that on SiO_2 (~ 5 kJ/mol). Figure 3.14 (b) shows that the heat of adsorption on WO_3 films is 8 kJ/mol lower than that on the unmodified SBA-15, while SBA-15 coated with $CaCO_3$ films show a heat of adsorption significantly larger (> 10 kJ/mol).

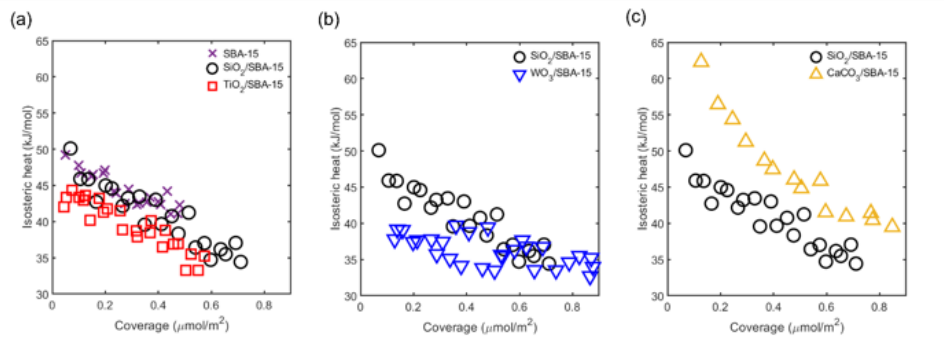

Figure 3.14 Differential heats of adsorption of benzene on (a) SBA-15, SiO_2/SBA-15, and TiO_2/SBA-15, (b) WO_3/SBA-15, and (c) $CaCO_3$/SBA-15.

Although the experiments convincingly show that surface chemistry has a profound impact on the strength of gas-surface interactions, the molecular origin of such difference is not evident. We perform DFT calculations to estimate adsorption energy which agrees well with the experimental heat of adsorption. As shown in Figure 3.15 and Figure 3.16, benzene exhibits a significantly stronger binding to the defected $CaCO_3$ surface than ethane molecules (0.70 eV difference).

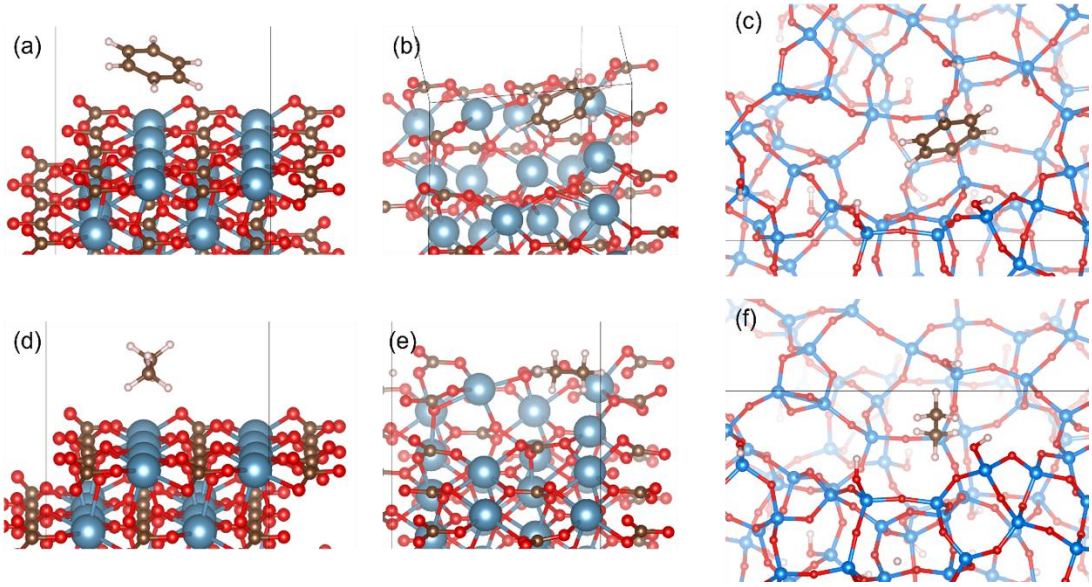

Figure 3.15 Schematics of benzene and ethane physisorption on (a, d) $CaCO_3$(100), (b, e) defected $CaCO_3$(100), and (c, f) amorphous silica surfaces, respectively.

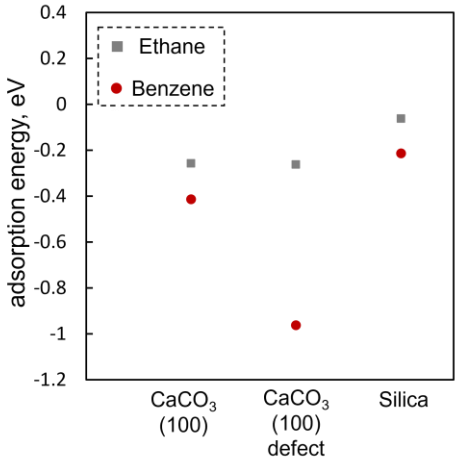

Figure 3.16 Adsorption results of benzene and ethane on $CaCO_3$ and amorphous silica surfaces.

We find that the adsorption of benzene is markedly more sensitive to the surface defects of $CaCO_3$ than alkane, where an under-coordinated Ca^{2+} ion exhibits strong interaction with

benzene, leading to a binding energy of 0.6 eV higher than that on the planar $CaCO_3$ surface. Notably, such sensitivity is absent on SiO_2 surfaces, where both molecules are physisorbed on a cavity moiety formed by siloxane rings (Figure 3.16) and exhibit nearly the same adsorption strengths. The DFT results suggest that the $CaCO_3$ defects, present as steps and kinks, enable a stronger cation−π interaction between Ca^{2+} and aromatic hydrocarbons. Further, this difference in the heat of adsorption agrees well with the lower interfacial energy between PS and $CaCO_3$ surface compared to that between SiO_2 for PS. This consistency between the high adsorption heats for benzene and the low interfacial energy for polystyrene on $CaCO_3$ films indicates that the phenyl group has a strong influence on the interactions of PS and benzene on $CaCO_3$ surface.

3.4. Discussion

Our results show a strong correlation between the heat of adsorption of small molecules and the interfacial energy between molten polymer and solid surface. The heats of adsorption (Figure 3.11 and Figure 3.14) and the interfacial energies (Figure 3.8) are compared in Table 3.5. Using the n-hexane as the representative molecules for PE and the benzene as the ones for PS, ~ 4 kJ/mol heat of adsorption difference leads to a ~30 mJ/m^2 difference of interfacial energy for both polymers. Another interesting observation is that while the interfacial energy of PE on $CaCO_3$ is higher than the one on SiO_2 and lower than TiO_2 and WO_3, the interfacial energy for PS on $CaCO_3$ is less than SiO_2, TiO_2 and $CaCO_3$. The WO_3 has the highest interfacial energy for both PS and PE. We attribute such difference to the strong interaction between the phenyl group and the $CaCO_3$ surface, which is validated by the much larger heat of adsorption of benzene on

$CaCO_3$ (≥ 13 kJ/mol above that on SiO_2 and TiO_2). This strong interaction could also be seen from the fact that the phenyl functional group helps PS infiltrate faster than PE.

Table 3.5 The heat of adsorption for small molecules and interfacial energy of polymers on different oxides.

Samples	**Heat of Adsorption[1] (kJ/mol)**		**Interfacial Energy[2] (mJ/m^2)**	
	Hexane	Benzene	PE	PS
SiO_2	44.8±1.2	47.2±1.0	42.71±0.00	39±2
TiO_2	40.1±0.7	42.6±1.3	68.27±0.14	55±3
WO3	40.0±1.8	38.4±0.9	69.53±0.11	61±3
$CaCO_3$	39.2±1.1	59.4±4.1	56.68±0.06	27±1

[1] Average value of coverage smaller than 0.2 μmol/m^2.

[2] Interfacial energies in Figure 3.8.

To probe whether a more quantitative relationship could be gleaned from the correlation between polymer-solid interactions and gas-solid interactions, we plot the interfacial energy between a polymer and a surface vs. the heat of adsorption for a respective small molecule-surface pair. The heat of adsorption is calculated as the average value obtained for coverage smaller than 0.2 $\mu mol/m^2$ in Figure 3.14. The selection of this range for averaging does not affect the overarching conclusion or the trends. The fact that the interfacial energy estimation based on the interaction between molten/condensed polymer and inorganic solid surface correlates well with the gas phase experiment at low concentrations is one of the most important findings of this work. As Figure 3.17 shows, the polymer-solid interfacial energies are negatively correlated with the adsorption heat of small molecules. We believe the high polarity of the benzene ring due to the presence of delocalized electrons induces stronger interactions with $CaCO_3$ and in turn causes a more dramatic change in the heat of adsorption for benzene. Moreover, our DFT calculations show that the non-crystalline structure of $CaCO_3$ is responsible for increasing the strength of interactions with benzene as shown in Figure 3.16. This trend indicates that interactions between polymers and solid surfaces are dominated by the enthalpic interactions between each repeat unit and the solid surface even if there are no polar functional groups that may undergo specific interactions with the surface chemistry of the solid. Our results indicate that characterizing gas adsorption is a powerful approach to predict interaction strength between polymers and solids. Moreover, the information from this study could inform how to design surfaces to favor interactions with one species over another to facilitate catalysis or separations.

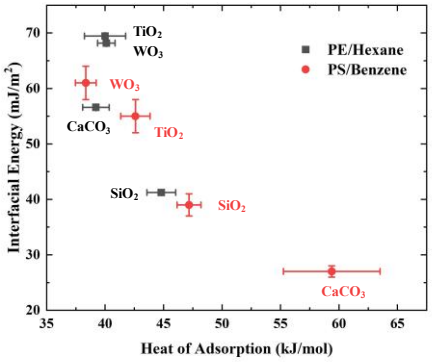

Figure 3.17 Interfacial energy of polymer (PE/PS) as a function of the heat of adsorption (hexane, benzene). Square symbols (□) use the data of Figure 3.8 (PE) and Table 3.5. Circle symbols (○) use the data of Figure 3.8 (PS) and Table 3.5 and Figure 3.14. (The heat of adsorption data is based on the average value obtained for coverage smaller than 0.2 μmol/m^2.)

To corroborate the observed monotonic trend between the solid-melt interfacial tension (γ) and the solid-gas adsorption heat, we use coarse-grained (CG) simulations combined with the test-area perturbation method[104] to evaluate γ at the solid-liquid interfaces under a broad range of conditions. The simulations use the bead spring model[122] to describe the polymer, whose chain length and stiffness are specified by N and k_a, respectively. The heat of adsorption of the gas-phase small molecules is described by the LJ parameter, ε_{SL}, which controls the interaction strength between a substrate bead and a polymer bead. In this work, we construct the relationship between γ and ε_{SL} by scanning across a wide range of ε_{SL}, then investigate how chain length and stiffness affect the γ-ε_{SL} relationship.

The simulation results agree well with the experimental trend. Figure 3.18 compares the calculated γ as a function of ε_{SL} for a simple liquid and those for polymer melts. These simulation results show a monotonically decreasing relationship between γ and ε_{SL} for the simple liquid. The trend is preserved as monomers connect into chain molecules, which corroborates the experimentally observed trend between interfacial energy and heat of adsorption. The results indicate that γ increases with chain length and chain flexibility. The increase in γ with chain length has been reported for *pure* chain-molecule fluid at the *vapor-liquid* coexistence[123,124], and is attributed to an increase in the cohesive energy of the liquid phase as chain length increases. Chain flexibility, however, is found to decrease surface tension, for the relatively short chains (N<5) studied in that work[124]. Although further simulation and theoretical work would be necessary to extend these theoretical models to heterogenous interfaces involving chain molecules, such a study is beyond the scope of this work.

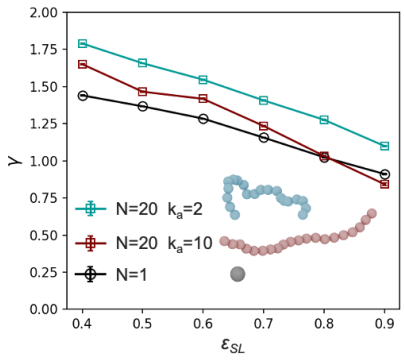

Figure 3.18 Interfacial tension (γ) of different liquids as a function of solid-liquid interaction strength (ε_{SL}) at T=1.0. The monomer (black) represents a simple liquid. The red and blue chain molecules represent inflexible and flexible polymers, respectively. While the factor of five

difference in stiffness may not necessarily apply to PS and PE, we believe such a generalized knowledge is valuable and can be applied when comparing many other polymers. The error bars, which are smaller than the size of the symbols, arise from averaging over different choices of area perturbation (ΔA^*).

In this work, we investigate the relationship between polymer-solid interfacial energy and heat of adsorption of small molecules onto solid surfaces. Our results, combining the experimental and computational efforts, show that the wetting characteristics of molten polymers on solids is highly correlated with the heat of adsorption of small gas molecules that bear structural similarity to the repeat unit of the polymer. The trends uncovered in this work shed light on the relationship between interactions of small hydrocarbon molecules and large macromolecules/polymers with solid surfaces. These concepts will enable the prediction of interactions of polymers with various surfaces via small molecule-based measurements and vice versa, which could be vital for designing porous solids and/or polymers that have desirable interactions for applications in gas separation membranes and polymer upcycling reactions. For example, the strength of interactions between the polymer and solid support can potentially influence the conformation of polymer chains or provide selective contact between a polymer and the surface, consequently affecting the reactivity and selectivity of polymer upcycling reactions. Our work primarily focused on a restricted set of polymer-surface pairs, with specific emphasis on non-polar polymers. To gain a more comprehensive understanding of solid-polymer interactions, it is crucial to conduct additional investigations exploring the influence of polar functional groups

and varying molecular weights of polymers. These aspects present promising avenues for future research.

CHAPTER 4. INVESTIGATING THE INCREASE IN THE EFFECTIVE VISCOSITY OF POLYETHYLENE UNDER EXTREME NANOCONFINEMENT: DEVELOPING A GENERALIZED FORMALISM TO UNDERSTAND CONFINEMENT EFFECT ON TRANSLATIONAL DYNAMICS OF POLYMERS

Reproduced from a manuscript accepted for publication on 12/12/2023 in the Journal of Chemical Physics (Special topic: Polymer nanoconfinement):

Manuscript Number: JCP23-AR-POLY2023-03872

Title: Increase in the Effective Viscosity of Polyethylene Under Extreme Nanoconfinement

Authors: Tian Ren, Zachary Hinton, Renjing Huang, Thomas H. Epps, III, LaShanda Korley, Raymond J. Gorte, and Daeyeon Lee

4.1 Introduction

Understanding the dynamics of polymers in nanoscale pores is crucial for advancing polymer upcycling reactions via heterogeneous catalysis. Polymer chains infiltrate catalyst pores that are often smaller than the polymers themselves, initiating interactions with catalytic sites.[125] The slow diffusion of polyethylene (PE) in the nanopores of catalysts has been shown to severely limit their conversion into useful products.[125] Conversely, strategic confinement can be exploited to engineer upcycling reactions for high-value-added products. The confinement of PE in mesopores, for example, has been used to modulate the distribution of the products via processive hydrogenolysis.[18,19] Confinement of polymers in well-defined cylindrical mesopores has also been shown to enhance the conversion of PE into high-valued liquid fuels.[126]

The dynamics of confined polymers also play a significant role in the fabrication of nanocomposite films and membranes with extremely high nanoparticle (NP) fractions. Capillary rise infiltration (CaRI) of polymers has emerged as a versatile method for producing nanocomposites with extremely high fractions of NPs (> 50 vol%).[26,41,44,127] Confinement of polymer chains in these nanocomposite films can dramatically enhance their fracture toughness[25] and also can enhance the thermal stability of the polymer chains in these nanocomposites.[54]

While it is well established that nanoscale confinement influences polymer transport, especially when polymer chains are larger than the nanopores,[44,54,128,129] the literature offers contrasting

observations on the specific nature of the impact on polymer dynamics. Some studies indicate accelerated polymer motion under confinement. For example, studies using molecular dynamics simulations and depth profiling using elastic recoil detection found enhanced polymer diffusion along the axis of cylindrical pores in anodized aluminum oxide (AAO) membranes.[130] Likewise, polymers confined within layered clay materials and AAO pores exhibit higher mobility than unconfined chains.[43,131] In contrast, other studies report slower polymer movement under increased confinement. Reduced diffusivity of poly(butadiene) in AAO channels[132] and decreased diffusion coefficients for deuterated poly(methyl methacrylate) (dPMMA) near the solid-polymer interface have been observed.[133] Likewise, slower diffusion rates for deuterated polystyrene (dPS) and dPMMA in crowded composites have been reported. [134,135]

These contrasting results indicate a complex relationship between nanopore confinement and polymer dynamics, necessitating further exploration.[32,33,44,50,136] Furthermore, few studies have focused on the impact of extreme nanoconfinement in which the radius of the pores (R_{pore}) is smaller than 10 nm, a size range particularly relevant for heterogeneous catalysis of polymers and fabrication of highly loaded nanocomposites via CaRI. Moreover, few studies have investigated the translational dynamics of polyethylene (PE), which is by far the most abundant commodity polymer,[137] partly due to challenges in creating sub-20 nm geometries and *in situ* monitoring. The high crystallinity and low solubility of PE in common organic solvents at room temperature also make it challenging to prepare samples to probe the extreme confinement effect on the translational dynamics of PE.

In this study, we explore the effects of extreme nanoconfinement on PE transport by using CaRI in disordered spherical SiO_2 NP packings. By adjusting SiO_2 NP sizes, we cover a broad range of pore radii from approximately 1 to 9 nm, which represents confinement conditions seldom explored. Using decalin as a high-boiling-point solvent, we prepare geometrically well-defined samples and employ *in situ* ellipsometry for real-time monitoring. Our findings reveal an inverse relationship between effective viscosity (η_{eff}) and R_{pore},[32,33,44,128,136,138] irrespective of chemistry of pore surface or polymer chain. These findings underscore the dominant role of physical confinement on polymer dynamics. We refine an existing model to better account for extreme nanoconfinement effects, offering a generalized framework for understanding polymer translational dynamics. Our results have important implications for catalyst support design, advancing polymer upcycling and nanocomposite fabrication.

4.2 Experimental Section

4.2.1 Materials

Two samples of PE were purchased from Polymer Source Inc. The molecular weight and the dispersity index ($Đ$) of each PE was characterized using high-temperature, gel permeation chromatography (HT-GPC) and were found to have weight-average molecular weights (M_w) = 27 kg/mol and $Đ$ = 1.17, and M_w = 50 kg/mol and $Đ$ = 2.04, respectively. Detailed GPC characterization results are in presented in the Supporting Material. Decalin, an equal mixture of cis + trans decahydronaphthalene (anhydrous, ≥99%), was purchased from Sigma-Aldrich Inc. PS was also purchased from Polymer Source Inc. with M_w = 88 kg/mol and $Đ$ = 1.1. The 61 nm-diameter silica NP suspension was generously provided by Nissan Chemical, and the 7, 17, and 25 nm silica NP suspensions were purchased from Sigma-Aldrich Inc. The ALD precursor $TiCl_4$ (99%)was purchased from STREM Chemicals, Inc, while the precursor titanium isopropoxide (TTIP) (97%) was purchased from Sigma-Aldrich Inc.

4.2.2 Preparation of Polymer and NP Layers

PE and NP thin films were separately prepared by spin-coating them onto 10 × 10 mm^2 silicon wafer substrates. Prior to spin coating, the silicon wafers were heated at 170 °C for 2 min. A 2.2

wt.% solution of PE with M_w = 50 kg/mol was prepared by stirring at 170 °C for 2 h and subsequently spin-coating at 170 °C and 5,000 rpm to achieve a film thickness of 135 ± 10 nm. PE samples with M_w = 27 kg/mol were coated using the same technique. All PE films are dried under ambient condition overnight. All NP films were spin-coated from aqueous suspensions to a thickness of 223 ± 8 nm with NPs of different sizes. Owing to their hydrophobic nature, the polymer films were easily delaminated from the substrates and floated at a water-air interface. These free-standing films were then placed onto the NP films to create a well-defined bilayer structure, which was allowed to dry in ambient air overnight. This process, as previously demonstrated in earlier work, [38] ensures the formation of a uniform bilayer structure.

4.2.3 Monitoring the Infiltration Dynamics of PE into SiO_2 NP Layers via Spectroscopic Ellipsometry

As discussed in a previous paper, polymer infiltration into the interstitial pores of NPs packings were monitored using spectroscopic ellipsometry. [38] The bilayer was annealed using a Linkham heating stage, which heats the sample at a rate of 30°C/min from 20°C to 120, 135, 150, 165, and 180°C. During this procedure, measurements of the refractive index as well as the thickness of polymer-infiltrated region of the NP packing and thickness of the top polymer layer, facilitate the

tracking of infiltration dynamics. η_{eff} under various confinement conditions was inferred based on the infiltration data as described in more detail below.

4.2.4 Atomic Layer Deposition (ALD) on NP Layers

ALD was used to deposit TiO_2 on spin-coated SiO_2 NP films, as previously reported in our work.[38] TiO_2 was selected for comparison with SiO_2 because PE interacts differently with these two surfaces, as reported in our previous report. [38] Titanium isopropoxide was chosen as the precursor for films made of NPs with diameters of 7 nm, 17 nm, and 25 nm, and $TiCl_4$ was used for 61 nm-diameter SiO_2 NP films. The reactor was initially purged with the precursor at 90 °C for 60 s, followed by a 30 s evacuation. This purge and evacuation process was repeated thrice, with the final evacuation lasting 90 s. During oxidation, the reactor was purged with saturated water vapor (60 °C, ~12 vol%) to react at 150 °C for 150 s, followed by a 60 s evacuation. This oxidation step was carried out five times to guarantee complete reactions, with the last evacuation in the final oxidation lasting 90 s. Additional TiO_2 ALD cycles could be conducted based on the desired final deposition thickness. After the ALD process, the samples were annealed at 500°C for an additional 10 min to ensure complete dehydration.

4.3. Results

4.3.1 Effective Viscosity (η_{eff}) of Polymers Infiltrating Spherical SiO_2 NP Packings based on the Lucas-Washburn Model

To study the effect of confinement on the dynamics of PE infiltration into nanopores, we prepare a bilayer consisting of a 135 ± 10 nm PE film on top of a 223 ± 8 nm thick SiO_2 NP film as schematically illustrated in Figure 4.1. The bilayer is subsequently heated at a temperature higher than the melting point of PE to induce CaRI of PE into the interstices of the SiO_2 NP film. Previous studies have evaluated the extent of polymer infiltration in the interstitial spaces between NPs by measuring the refractive index changes upon CaRI using ellipsometry. [27,30,41] In the limit of the resolution that ellipsometry provides, polymers fully fill the interstitial voids in the NP packings. [27,30,41] Previous studies have shown that the average pore size of the random close packings of spherical particles is approximately 30% of the particle size, an estimation that has been confirmed in recent work using an ellipsometry porosimeter for SiO_2 NP films.[127] Table 4.1 summarizes R_{pore} of NP packings based on the size of SiO_2 NPs as random packing used in this study.[56] All of the NPs used in this work are spherical in shape. The interstitial pores in these NP packings are interconnected, and thus polymer can infiltrate throughout the entire packing. The shape and size distribution of the interstitial pores have been characterized computationally in a previous publication.[139]

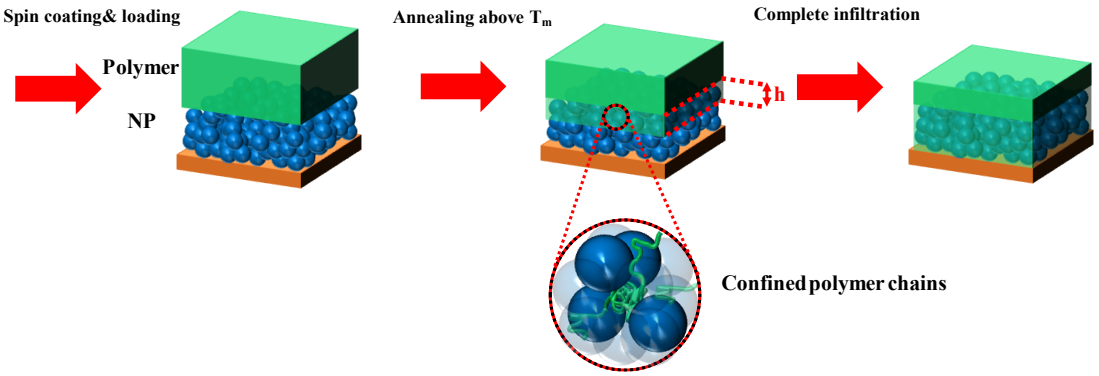

Figure 4.1 Schematic illustration of PE infiltration into random packing of spherical SiO_2 NPs. PE is induced to undergo CaRI by heating the bilayer at temperatures above its melting point.

Table 4.1 Average pore radius ($R_{pore} = 0.289 \times R_{NP}$) of NP packing as a function of NP radius.[56,140]

Average NP radius (R_{NP})/nm	Average pore radius (R_{pore})/nm
3.5±0.6	1.0±0.2
8.5±1.2	2.4±0.3
12.5±2.1	3.6±0.6
30.5±6.0	8.8±1.7

The degree of confinement as defined by the ratio of the radius of gyration (R_g) of PE in its molten state to R_{pore} can be readily adjusted by changing the size of NP or the molecular weight of PE. In this study, by using SiO_2 NPs ranging between 3.5 and 30 nm in radius and two PEs with weight average molecular weight (M_w) = 27 kDa and 50 kDa, we vary the confinement ratio ($\Gamma = \frac{R_g}{R_{pore}}$) from 0.92 to 11.0.

The molecular weight distributions of the polyethylene (PE) samples are determined using HT-GPC (Tosoh HLC-8312GPC/HT). Samples are prepared at 2 mg/mL in mobile phase (1,2,4-trichlorobenzene, HPLC grade, with 500 ppm butylated hydroxytoluene added), and 0.3 mL injections are eluted for 80 min at 140 °C and 0.8 mL/min. Three columns in series (two TSKgel GMHHR-H(20)HT and one TSKgel G2000HHR (20)HT) are utilized in conjunction with a refractive index detector. Molar masses are determined using a calibration curve constructed from runs of nine narrow PS standards (between $6x10^2$ and $2x10^6$ g/mol) and, for PE, corrected for differences in intrinsic viscosity via the Mark-Houwink relationship.[141] The molecular weight averages, the number-average molecular weight (M_n) and weight-average molecular weight (M_w) are calculated by integrating the obtained distributions, and dispersity ($Đ$) of the polymer samples is determined as the ratio of M_w to M_n. The HT-GPC results, presented in Figure 4.2 and Table 4.2, reveal a multimodal distribution in the case of the 50 kDa PE likely due to chain scission during the manufacturing process (*i.e.*, hydrogenation of polybutadiene). In our study, the measured M_w values are primarily used to quantify the bulk viscosity of the samples.

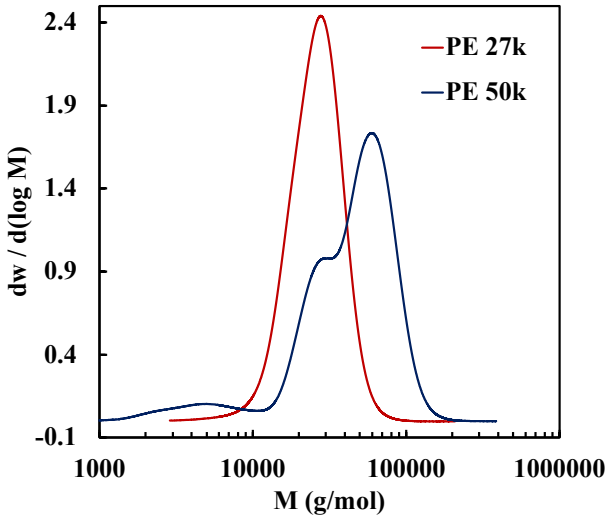

Figure 4.2 The molecular weight distribution of two PEs is characterized using HT-GPC.

Table 4.2 The measured molecular weight characteristics for the PEs used in this work.

PE	M_n **(kg/mol)**	M_w **(kg/mol)**	$Đ$
27 kDa	23.3	27.3	1.17
50 kDa	24.5	50.0	2.04

Building upon recent work,[38] we deduce the infiltration time from the changes observed in the refractive index of the NP film. The dynamic ellipsometry data for amplitude (Ψ) and phase difference (Δ) are fitted using a two-layer Cauchy model, allowing us to obtain the refractive index

of the polymer-infiltrated NP layer. By analyzing the initial and final states and evaluating the refractive index changes, the time (t) to fully infiltrate the NP film can be determined. Additionally, the infiltrated thickness (h) can be obtained by using a three-layer Cauchy model, which results in an infiltration time (t) that is consistent with the one based on the refractive index tracking.

Subsequently, η_{eff} of PE is calculated based on the Lucas-Washburn model for liquid infiltration, as shown in **Eq (22)**:

$$h^2 = \frac{\gamma_{PE} \cdot R_{pore,NP} \cdot cos\theta}{4 \cdot \tau^2 \cdot \eta_{eff}} t \quad (22)$$ [41,76]

wherein the surface tension of PE, γ_{PE}, is calculated based on the prior results at different temperatures from 120 to 165 °C. [94] The contact angle (θ in **Eq (22)**) of PE on silica is taken as 21°.[39] η_{eff} under confinement is calculated by using the time it takes to fully infiltrate the NP film (i.e., infiltration time). Alternatively, η_{eff} can be inferred from the raw data by plotting h^2 as a function of time as shown in Figure 4.3. η_{eff} can be calculated from the slope of such a plot ($\frac{\gamma_{PE} \cdot R_{pore,NP} \cdot cos\theta}{4 \cdot \tau^2 \cdot \mu}$); these two methods yield essentially the same values for η_{eff}. The extensional viscosity of the polymer could potentially influence the transport of polymers through the porous network in these NP packings. Any impact of extensional viscosity as well as the distribution in the pore size within the NP packings would be lumped into η_{eff}.

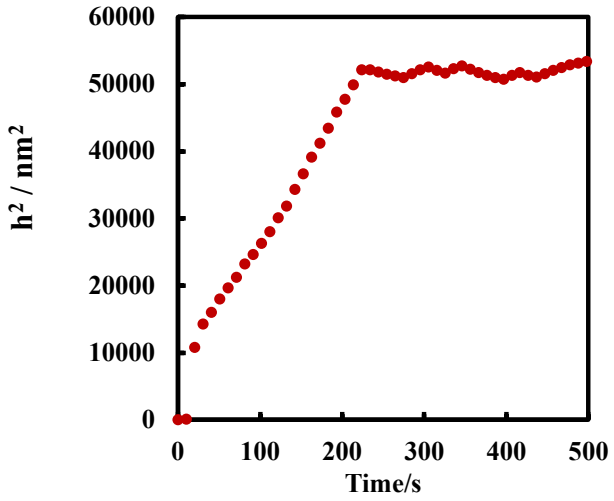

Figure 4.3 Representative data showing the square of PE infiltrated thickness (h^2) as a function of time into a SiO_2 61 nm-NP packing.

By using NP films as the model porous media, we change R_{pore} from 1.0 to 8.8 nm. We investigate the impact of R_{pore} on η_{eff} of PE at different temperatures. A temperature increase of about 15 °C decreases η_{eff} by a factor of $10^{0.25}$ across all pore radii. More importantly, our data reveal that the η_{eff} of PE with M_w = 50 kDa exhibits an inverse relationship with R_{pore}. This trend is clearly illustrated in the log-log plot shown in Figure 4.4, where a slope of -1 indicates the inverse proportionality. To probe the effect of M_w on the observed trend, we determine the η_{eff} of PE with M_w = 27 kDa at 150 °C, which also exhibits the same inverse relationship as shown in Figure 4.4 (b). To the best of our knowledge, this finding is the first report describing such a scaling relationship between η_{eff} of PE and R_{pore} in highly confined systems.[32]

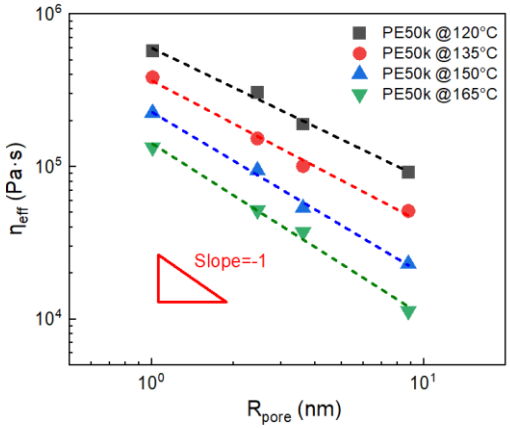

(a)

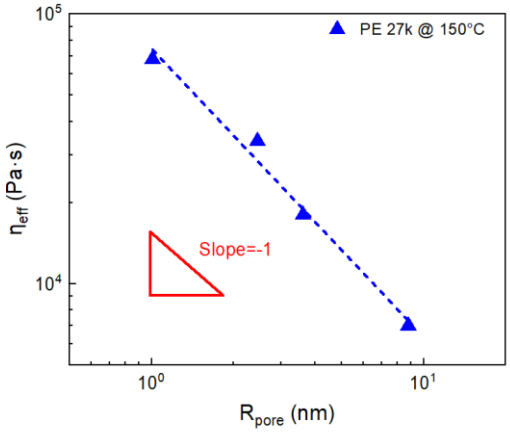

(b)

Figure 4.4 (a) η_{eff} of 50 kDa PE as a function of R_{pore} at different temperatures and (b) η_{eff} of 27 kDa PE as a function of R_{pore} at 150 °C.

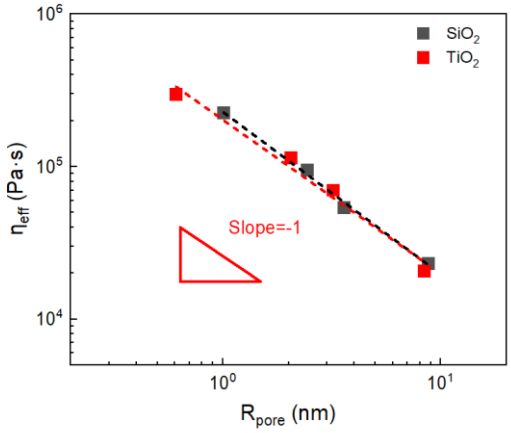

Figure 4.5 η_{eff} of PE at 150 °C as a function of R_{pore} before and after TiO_2 modification using ALD. The contact angle of PS on TiO_2 is taken to be 85° based on our prior work.

To study how the surface chemistry of the pore may impact the relationship between η_{eff} and R_{pore}, we measure the η_{eff} of PE in TiO_2-coated nanopores. Our previous work has shown that PE's interaction with SiO_2 is much stronger than that with TiO_2 as represented by interfacial energy. The interfacial energy between PE and SiO_2 and between PE and TiO_2 are 42.7 and 68.3 mJ/m^2 [39], respectively, indicating that PE has more favorable interactions with SiO_2 than with TiO_2. SiO_2 NP films are modified with a 0.4 nm thick TiO_2 coating prepared via ALD. This thickness ensures that the TiO_2 completely covers the surface of SiO_2 NPs while the structure and the size of the pores are minimally impacted. As illustrated in Figure 4.5, the η_{eff} of PE in both cases overlap, indicating that surface composition or surface-polymer interactions have little impact on the dependence of η_{eff} on R_{pore}.

To test whether this inverse relationship between η_{eff} and R_{pore} also applies to other polymers, we examine the η_{eff} of confined polystyrene (PS, M_w = 88 kDa), a widely studied amorphous commodity polymer, infiltrating SiO_2 NP films. We find that both PE and PS show the same relationship with a slope of -1 between η_{eff} and R_{pore} As shown in Figure 4.6. These results highlight the potential universality of this inverse relationship.

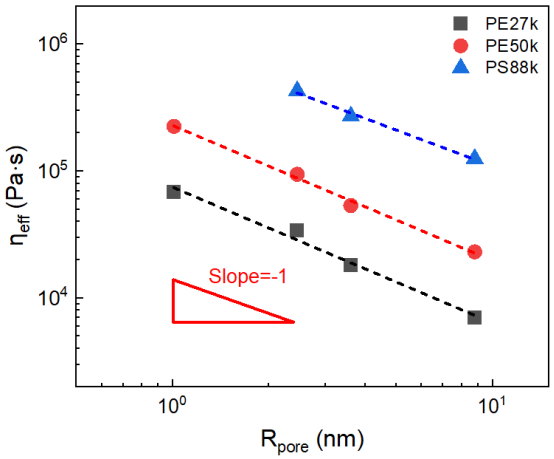

Figure 4.6 . η_{eff} of PE and PS as a function of R_{pore} measured at 150 °C.

4.4. Discussion

Our results convincingly show that η_{eff} of both PE and PS is inversely proportional to R_{pore} for polymers that are infiltrating the interstitial pores in the random packings of NPs. To understand this inverse proportionality, we use the modeling approach proposed in Ref 32, which provides a relationship between the ratio of η_{eff} to bulk viscosity (η_0) and R_{pore}:

$$\frac{\eta_{eff}}{\eta_0} = \left[\left(\frac{R_{eff}}{R_{pore}}\right)^4 + \phi\frac{8N_e^{\alpha}b^3\eta_0}{3\zeta N{R_{pore}}^2}\right]^{-1} = \left[\left(1-\frac{\Delta R}{R_{pore}}\right)^4 + \phi\frac{8N_e^{\alpha}b^3\eta_0}{3\zeta N{R_{pore}}^2}\right]^{-1} \quad (23)$$

wherein N is the number of Kuhn segments, N_e is the entanglement segment number, and α is the exponent chosen to be 1.5; R_{eff} is the effective pore radius while ΔR is the thickness of adsorbed layer of polymer on the pore surface (i.e., $R_{eff} = R_{pore} - \Delta R$); b is the Kuhn monomer length; ζ is the friction constant for a single Kuhn segment; ϕ is fraction of polymeric chains that are undergoing reptation and is regarded as 1 in our system because both of the PE samples used in this study are entangled (i.e., $M_w > M_e$ (entanglement molecular weight)). The M_e for PE, PS, and PEO are 1k, 17k, and 2kDa respectively.[55]

This generalized model was developed to describe the η_{eff} of confined polymers undergoing CaRI in a cylindrical pore by calculating the translational velocity of a polymer chain along the reptation tube under a pressure gradient that is produced by capillary forces. Based on η_{eff} of poly(ethylene oxide) (PEO) undergoing capillary rise in AAO, this model showed a qualitative agreement with experimental results when R_{pore} was varied from 12.5 nm to 200 nm, and the molecular weight was varied between 50 kDa and 1 MDa. The first term inside the bracket accounts for the influence of adsorbed polymer chains on the pore surface. These chains effectively reduce R_{pore} to an effective radius (R_{eff}), thereby creating a "dead zone" within the pore. The second term represents the reptation of free polymer chains, driven by a pressure gradient within the polymer melt. In scenarios where R_{pore} is significantly larger than ΔR, the first term becomes dominant, leading to an increase in normalized effective viscosity. Conversely, when $R_{pore} < R_g$, the second term gains prominence, resulting in a reduction of the normalized effective viscosity.

However, the expected trends based on this model (dashed lines in Figure 4.7), do not agree well with our experimental results as shown as in Figure 4.7. While our data indicate that η_{eff} increases with decreasing pore radius, the model predicts the opposite trend. Upon close inspection, the data presented in Ref 32 and 142 also show that the η_{eff} increases when the pore radius becomes smaller than 17.5 nm.[32,142] Another recent study[143] has reported that the time for infiltration of PS into mesoporous silica increases when R_{pore} decreased from 2.4 to 1.7 nm; however, no quantitative relationship between R_{pore} and η_{eff} was presented.

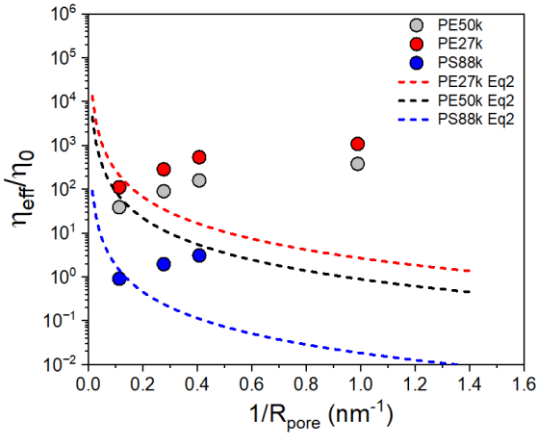

Figure 4.7. η_{eff}/η_0 of PE and PS based on global fitting using Eq(23).

The inverse scaling between η_{eff} and R_{pore} hints at a possible refinement to **Eq(23)**, particularly the second term on the right hand side.[32] In its original derivation, the cross-section of the reptation tube was chosen as the cross-section of the moving path of a polymer chain, which would be a reasonable choice for entangled polymers that are not highly confined. However, for a highly confined chain (i.e., $R_g < R_{pore}$) the conformation of the chain and its entanglement

length are likely to be influenced by R_{pore}.[130,144,145] Alternatively, we choose the cross-sectional area of the pore (R_{pore}^2) as the cross-section area of the moving path of the chain. Moreover, we consider the effect of extreme confinement on ζ, the dimension of the chain along the moving direction $<R_x>$ and the primitive path contour length of the polymer chain (L) (see Supporting Information for detailed derivation). These refinements to the second term of **Eq(23)** yield the following equation for the normalized effective viscosity:

$$\frac{\eta_{eff}}{\eta_0} = \frac{3\sqrt{6}\cdot\zeta_0\cdot {N_{e,0}}^{-0.5}}{32\varphi\tau^2\cdot R_{pore}}\cdot\frac{1}{B\cdot N^{1.9}},\ \text{when } R_g > R_{pore} \qquad (24)$$

wherein ζ_0 and $N_{e,0}$ are the friction coefficient and the number of entanglement segments for bulk polymer, respectively, and B is a prefix indicating the dependence of η_0 on the number of segments, following $\eta_0 = B\cdot N^{3.4}$. **Eq (24)** provides the scaling relationship between R_{pore} and η_{eff} observed in our work. Moreover, the normalized viscosity of PEO confined in pores smaller than 20 nm in Ref 32 and 142 show good agreement with the -1 scaling as shown in Figure 4.8.

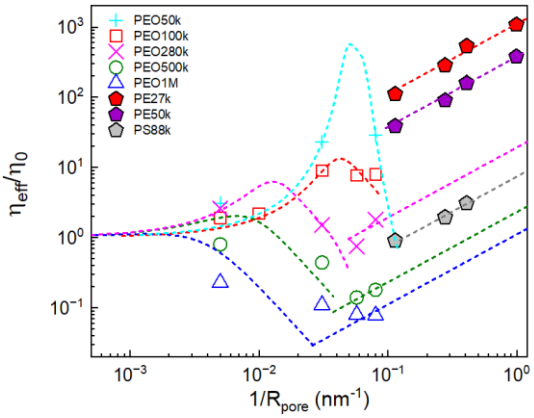

Figure 4.8 η_{eff}/η_0 of PE (experimental results from the current work) and PEO (from Ref 32) obtained experimentally and predicted based on the refined model as a log-log plot. The dotted curves are based on **Eq (36)** and **Eq (37)** which are derived in the following paragraphs.

We refine the generalized theory proposed by Ref 32 to better understand the impact of pore size on polymer infiltration. Here, we summarize the derivation of the original model and then discuss modifications we introduce. The theory aims to describe how pore size influences the ratio of effective viscosity to bulk viscosity as given by **Eq(25)**:

$$\frac{\eta_{eff}}{\eta_0} = \left[\left(\frac{R_{eff}}{R_{pore}}\right)^4 + \phi\frac{8N_e^{\alpha}b^3\eta_0}{3\zeta NR^2}\right]^{-1} = \left[\left(1-\frac{\Delta R}{R}\right)^4 + \phi\frac{8N_e^{\alpha}b^3\eta_0}{3\zeta NR^2}\right]^{-1} \quad (25)$$

The first term inside the bracket accounts for the influence of adsorbed polymer chains on the pore surface. These chains effectively reduce the pore radius (R_{pore}) to an effective radius (R_{eff}), thereby creating a "dead zone" within the pore. The second term represents the reptation of free polymer chains, driven by a pressure gradient within a network. For scenarios in which the pore size (R_{pore}) is significantly larger than the dead zone (ΔR), the first term becomes dominant, leading to an increase in normalized effective viscosity. Conversely, when $R_{pore} < \Delta R$, the second term gains prominence, resulting in a reduction of the normalized effective viscosity.

In our current study, we focus on a range of pore sizes (R_{pore} = 1 – 9 nm) that predominantly fall within the regime wherein the second term in Eq S1 is the dominant factor. Accordingly, we refine the derivation of this term, accounting for the effects of extreme nanoconfinement. The

motion of a polymer chain along the direction of the pressure gradient can be described as follows:

$$[-p(x + R_x) + p(x)] \cdot l^2 = -l^2 R_x \frac{\partial p}{\partial x} \quad (26)$$

in which l^2 is the cross-section of the moving path, and R_x is the x-component end-to-end vector.

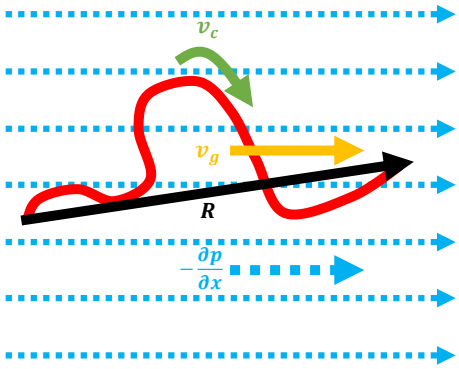

Figure 4.9 Schematic representation of the reptation motion of a polymer chain under a pressure gradient reproduced from Ref 32.

As illustrated in Figure 4.9, the velocity of a polymer chain along its reptation tube under a pressure gradient[32], v_c, and the friction of the free chain, $N\zeta v_c$ (wherein ζ is friction coefficient), is related to the number of segments, N. Balancing the pressure gradient and frictional force results in:

$$N\zeta v_c = -l^2 R_x \frac{\partial p}{\partial x} \quad (27)$$

and thus, v_c can be expressed as:

$$v_c = -\frac{l^2}{N\zeta} R_x \frac{\partial p}{\partial x} \tag{28}$$

The average velocity of the center of mass of the polymer chain, denoted as v_g, is related to the entanglement length, N_e:

$$\langle v_g \rangle = \left\langle \frac{\overrightarrow{R_x}}{L} \cdot v_c \right\rangle = \frac{l^2}{\zeta NL} \cdot \left\langle \overrightarrow{R_x}^2 \right\rangle \cdot \left\langle \overrightarrow{\left(-\frac{\partial p}{\partial x}\right)} \right\rangle. \tag{29}$$

By averaging the pressure gradient along the entire polymer melt (i.e., $-\frac{\partial p}{\partial x} = \frac{2\gamma cos\theta}{hR_{pore}}$), the speed of capillary filling can be expressed by

$$\frac{dh}{dt} = \varphi \langle v_g \rangle = \varphi \frac{l^2 a_t}{3\zeta N} \frac{2\gamma \cos(\theta)}{hR_{pore}} \tag{30}$$

wherein φ represents the fraction of polymer chains involved in the reptation process. The choice of the cross-sectional area l^2 is not trivial. The diameter of the reptation tube was chosen as the cross-section, denoted as ($l^2 = a_t^2$), resulting in,

$$\frac{dh}{dt} = \varphi \frac{{N_e}^{1.5} b^3}{3\zeta N} \frac{2\gamma \cos(\theta)}{hR_{pore}} \tag{31}$$

The exponent for N_e can also be 1 if a different expression for the cross-section is used.[146]

Defining the effective viscosity (η_{eff}) as

$$\frac{dh}{dt} = \frac{\gamma \cos(\theta) R_{pore}}{4\eta_{eff} h} = \varphi \frac{{R_{pore}}^2 b^3}{8\eta_{eff}} \frac{2\gamma \cos(\theta)}{hR_{pore}}. \tag{32}$$

The ratio of the effective viscosity to the bulk viscosity ($\frac{\eta_{eff}}{\eta_0}$) can be expressed as

$$\frac{\eta_{eff}}{\eta_0} = (\varphi \frac{8\, {N_e}^{1.5} b^3 \eta_0}{3\zeta N {R_{pore}}^2})^{-1} \quad . \qquad (33)$$

As highlighted in Figure 4.7, our experimental results starkly contradict the predictions of this model. We believe that this discrepancy arises from the extreme nanoconfinement conditions; the pore radius (R_{pore}) is smaller than the R_g of the polymer. This level of confinement contrasts with the conditions in References [32] and [142], for which R_g is either comparable to or larger than R_{pore}. Under extreme nanoconfinement, the translational motion of a polymer chain is not only constrained by interactions with other chains but is also significantly influenced by the physical boundaries, *i.e.*, the pore surface.

To address this, we refine the model to account for the potential impact of extreme nanoconfinement on certain parameters. We adopt ${R_{pore}}^2$ instead of ${a_t}^2$ as l^2. Furthermore, under extreme confinement conditions, ζ is known to depend on the size of the confining pore, following $\zeta \sim {R_{pore}}^{\frac{-2}{3}}$.[144] The primitive path contour length of the chain under biaxial confinement (L) also exhibits a similar dependency on the pore radius, given by $L \sim {R_{pore}}^{-\frac{2}{3}}$.[145] Another parameter likely influenced by confinement is the x-component of the end-to-end distance ($\langle {R_x}^2 \rangle$). This dependency is inferred from simulations results in Ref 130, which explored the effects of cylindrical biaxial confinement on the chain dimension along the long axis of the pore. The relationship is given as $\langle {R_x}^2 \rangle \sim {R_{pore}}^{-\frac{1}{3}}$.[130]

Incorporating these four parameters to account for the extreme nanoconfinement conditions that a polymer chain would experience during translation motion under a pressure gradient,[15] the second term in **Eq(25)** can be reformulated as follows:

$$\eta_{eff} \approx \frac{3\sqrt{6}\cdot\zeta_0 N^{1.5}\cdot {N_{e,0}}^{-0.5}}{32\varphi\tau^2\cdot R_{pore}} \ . \qquad (34)$$

wherein ζ_0 and $N_{e,0}$ are the friction coefficient and the number segments in an entanglement strand for bulk polymer, respectively. This refined model suggests that the effective viscosity is inversely proportional to R_{pore}, which aligns well with our experimental findings.

Interestingly, if we maintain R_g^2 as l^2 in **Eq(30)**, even in the unconfined case (i.e., $R_{pore} > R_g$), **Eq (23)** in the main text can be reformulated as follows:

$$\frac{\eta_{eff}}{\eta_0} = \left[\left(1-\frac{\Delta R}{R_{pore}}\right)^4 + \frac{4\varphi\cdot b^3\cdot\tau^2}{9\cdot {N_e}^{-0.5}\cdot\zeta\cdot {R_{pore}}^2} B\cdot N^{3.4}\right]^{-1} \qquad (35)$$

for which B is a prefix indicating the dependence of bulk viscosity on the number of segments, following $\eta_0 = B\cdot N^{3.4}$. The reformulated **Eq (35)** shows improved agreement with the experimental results presented in Ref 32, compared to the original generalized equation, as shown in Figure 5 in the main text.

By incorporating these refinements into **Eq (23)**, we offer a generalized formalism that describes the non-monotonic variation in normalized effective viscosity using the following two equations:

$$\frac{\eta_{eff}}{\eta_0} = \frac{3\sqrt{6}\cdot\zeta_0\cdot {N_{e,0}}^{-0.5}}{32\varphi\tau^2\cdot R_{pore}} \cdot \frac{1}{B\cdot N^{1.9}}, \qquad R_{pore} < R_g \quad (36)$$

$$\frac{\eta_{eff}}{\eta_0} = \left[\left(1 - \frac{\Delta R}{R_{pore}}\right)^4 + \frac{4\varphi\cdot b^3\tau^2}{9\cdot {N_e}^{-0.5}\cdot\zeta\cdot {R_{pore}}^2} B\cdot N^{3.4}\right]^{-1} \qquad R_{pore} \geq R_g \quad (37)$$

These two equations offer a new perspective on how the effective viscosity of an entangled polymer varies with pore radius as qualitatively illustrated in the Highlight image.

These results suggest that the dependence of the normalized effective viscosity of polymer undergoing translational motion due to a capillary pressure gradient has at least three different regimes:

These results suggest that the dependence of the normalized effective viscosity of polymer undergoing translational motion due to a capillary pressure gradient has at least three different regimes:

1) a slight increase when the pore is not too small (R_{pore} > ~ 150 nm, or $R_{pore}/R_g >> 1$) due to the so-called dead-zone effect, which effectively decreases R_{pore}, as summarized by the first term in **Eq (23)**;

2) a decrease at an intermediate R_{pore} range (R_{pore} = ~ 20 – ~150 nm, or $1 \leq R_{pore}/R_g$ < ~ 10) due to the confinement enhanced mobility of reptating chains, which is expressed by the second term in **Eq (23)** and

3) a dramatic increase at high degrees of confinement when R_{pore} < ~ 20 nm, or R_{pore}/R_g < 1 (**Eq (24)**).

Additionally, **Eq (24)** predicts that $\eta_{eff} \sim \frac{N^{1.5}}{R_{pore}}$. The dependence of η_{eff} on the chain length ($\eta_{eff} \sim N^{1.5}$) is indeed consistent with the trends observed in prior studies although validating this dependence is not the focus of our current study.[32,43] While the agreement between the experimental results and **Eq (24)** is remarkably good when $R_g < R_{pore}$ as shown in Figure 4.8, the dependence of η_{eff} on R_{pore} clearly warrants further investigation. We believe more detailed computational and theoretical modeling efforts will be necessary to fully understand the molecular origin of the observed trend.

4.5. Conclusions

In this study, we explore the influence of sub-20 nm confinement on η_{eff} of PE undergoing CaRI into random packings of SiO_2 NPs. We use the Lucas-Washburn model to determine η_{eff} of the confined polymer undergoing CaRI. Our findings reveal an inverse relationship between η_{eff} and R_{pore}. This inverse proportionality holds true not only for PE infiltrating TiO_2-coated NP packings but also for PS infiltrating SiO_2 NP packings. These results suggest that physical confinement rather than surface composition and surface-polymer interactions has the dominant impact on the dependence of η_{eff} on R_{pore}. We adopt and refine a previous theory to model the dependence of η_{eff} on R_{pore}. This new generalized formalism provides an insight into the non-monotonic changes in η_{eff} of confined polymer as R_{pore} is reduced. The molecular scale mechanism responsible for the inverse scaling relationship when R_{pore} is smaller than the radius of gyration of the polymer requires future investigation. Our research makes important contributions to our understanding of polymer dynamics in confined environments and provides crucial insights into the impact of R_{pore} and surface chemistry on η_{eff} of infiltrating polymers. These findings have far-reaching implications for various applications involving polymer upcycling reactions utilizing heterogeneous catalysts and the fabrication of polymer nanocomposites via CaRI.

CHAPTER 5. ELUCIDATING THE DECREASE OF MELTING POINT FOR POLYETHYLENE UNDER EXTREME NANOCONFINEMENT

5.1. Introduction

Many widely used commodity polymers as well as specialty polymers such as conducting polymers are semi-crystalline. The arrangement of repeat units in these polymers exhibits a high degree of regularity, enabling the formation of crystalline domains despite their long-chain architecture. Semi-crystalline polymers generally offer enhanced mechanical strength, exceptional resistance to degradation, and superior barrier properties relative to their amorphous counterparts, which can be attributed to the tightly packed chains within the crystalline regions. Unlike small molecules that can achieve 100% crystallinity, polymers seldom reach full crystallinity due to challenges like chain entanglement, structural irregularities, and steric hindrance. These limitations result in materials comprising both crystalline and amorphous domains. The melting of semi-crystalline polymers induces a phase transition, changing the polymer chains from an ordered lattice structure to a disordered, amorphous state. This transition dramatically alters key physical characteristics, including permeability, mechanical strength, and transport properties; thus it is critical to understand how different factors would affect the melting and formation of these crystalline domains.

Confinement of polymers is known to induce fundamental changes to their properties and behavior. For example, the glass transition temperature (T_g), an important thermal transition in glassy polymers, is affected significantly by physical confinement. Both increases and decreases in T_g have been reported depending on the geometry and surface chemistry of confining boundaries. Confinement has also shown to dramatically change the translational dynamics of polymers significantly from their bulk state; again, both increases and decreases in dynamics in confined polymers have been reported. The critical temperature for the miscibility of polymer blends also shifts upward or downward under extreme nanoconfinement.

Several studies have reported a decrease in the melting (T_m) and crystallization (T_c) temperature when polymers are confined within small pores. For example, both the crystallinity and T_m are decreased substantially when PE is confined to cylindrical pores of anodized aluminum oxide (AAO) membranes. The trend suggests that the decline in the melting point is minimal when the pore size is reduced to less than 50 nm.[147–151] The decrease in the crystallinity of confined PE was attributed to the constraints in chain motion and nucleation due to confinement-induced changes in the chain conformation. In addition to physical confinement, the importance of interfacial effects on the T_m of confined semi-crystalline polymers such as PE has also been reported. For example, T_m of a thin PE film decreases with decreasing thickness below 72 nm and the extent of this reduction depends on the strength of interactions between the polymer and

the substrate; stronger interactions result in more significant depression of T_m.[152] Despite these advances in investigating the influence of physical confinement on Tm of PE, most of these studies have focused mainly on physical confinement of 20 nm or larger.[147–151] The limitation in the length scale of confinement is likely due to the difficulty in confining PE into sub-20 nm pores.[147–153] This length is of particular importance as the size of a single crystalline lamellae of PE is reported to be ~ 11 nm. [137,154]

In this work, we investigate the effect of extreme nanoconfinement (< 20 nm) on the melting point of polyethylene. Utilizing capillary rise infiltration, we confine PE into the interstices of randomly packed SiO_2 nanoparticle (NP)s. By controlling the size of NPs, the size of the confining pores is varied from 2 to 18 nm of diameter. The effect of surface chemistry is also explored by coating SiO_2 NP with sub-1 nm TiO_2 and $CaCO_3$ using atomic layer deposition. Our in-situ spectroscopic ellipsometry results revealed two key insights: First, as the pore size diminishes, the melting transition of PE correspondingly decreases; second, this suppression in melting point plateaus when the pore diameter is below ~8 nm. This overall trend is unaffected by the surface chemistry of the pores, indicating the dominating influence of physical confinement on melting transition. The results in the depression of Tm show a strong correlation with the decrease in the crystallinity of PE in the random packings of NP.

5.2 Experimental Section & Method

5.2.1 Materials

The commercial PEs are purchased from Polymer Source Inc.: #P2861-E with a measured Mw=50,000 and PDI=2.01, and #P1984-E with a measured M2=27,000 and PDI=1.17 by high-temperature gel permeation chromatography (HT-GPC). The low-density polyethylene (LDPE) of low density, melt index 25 g/10 min (190°C/2.16kg) is purchased from Sigma Aldrich Inc.

The solvent decalin is decahydronaphthalene, a mixture of cis + trans, and is purchased from Sigma-Aldrich.

The SM, HS, and TM-50 silica NP suspension are purchased from Sigma-Aldrich Inc.

The ST-YL silica (SiO_2) suspension is given by Nissan Chemical.

In the ALD system, all the precursors are purchased from STREM Chemicals, Inc including bis (2,2,6,6-tetramethyl-3,5-heptanedionato), calcium (Ca(TMHD)2), and titanium chloride ($TiCl_4$).

5.2.2 Preparation of the Polymer and NP Layer

In this research, the PE solution is made at 2.2 wt % with decalin and stirred for 2 hours at 170°C. The silicon wafer is cut into $10 \times 10\ mm^2$ substrates and annealed at 170°C for 2 minutes. Then a PE film of $115 \pm 7nm$ is spin-coated onto the 170°C substrates.

All the NP films are spin coated at $223 \pm 8nm$, and then some of them are deposited with TiO_2 and $CaCO_3$. The polymer films are peeled off and floated on the water-air interface because of hydrophobicity. Then the free-standing polymer films are loaded onto the ALD-treated NP. This process can give a well-defined bilayer structure and be dried naturally overnight, which has been demonstrated in our previous paper.[38]

5.2.3 Atomic Layer Deposition on NP Layer

The ALD method deposits TiO_2, and $CaCO_3$ onto both spin-coated NP films and NP pellets as our previous paper showed[38]. In that system, the ALD growth rate is calculated by the weight gain of the pellets and confirmed the same by calculation with the refractive index change of the thin films under an ellipsometer.

5.2.4 Estimation of Melting Points via Spectroscopic Ellipsometer

Capillary rise infiltrations are observed via our ellipsometry as our previous paper discussed. [38] The bilayer is annealed with a Linkham heating plate at a rate of 30°C /min from 20°C to 150°C. Then, extra cooling at 10°C /min to 30°C is added after the infiltration is finished. Another annealing at 30°C /min to 150°C and cooling at 10°C /min to 30°C are added for 2 cycles. During this process, both the refractive index of the nanocomposite layer and the thickness of the polymer layer can help to analyze and determine the melting point. [150]

5.2.5 XRD

The crystalline size of the bulk polymer is checked by Rigaku MiniFlex 600 XRD at the University of Pennsylvania.[155,156] The 2% hot solution in decalin is prepared at 170C and drop-coated on the silicon holder. All the coated samples are dried at 170°C for 1 hour. The diffraction angle ranges from 10 to 90 degrees with a scanning rate of 20 degrees per minute.

LDPE-infiltrated NP pellets are also characterized using XRD. NP and LDPE pellets are compressed into pellet form using pelletizers, utilizing 0.2g of the respective powders. The LDPE pellet is placed on top of the NP pellets, annealed to 200°C, and the infiltration is completed within 2 hours. For XRD of LDPE-infiltrated NP pellets, the infiltrated section is excised, ground into powders using a crucible, affixed to a substrate using a ceramic adhesive, and subsequently analyzed by XRD. The only NP samples and bilayers are directly subjected to XRD analysis.

5.3 Results and Discussion

We study the effect of confinement on the melting point of PE by infiltrating the polymer into the interstices of randomly packed NP film as illustrated in Figure 5.1. The average of pore size of such a packing is approximately 30% of the pore size; thus, the extent of confinement can be readily changed by varying the size of NPs. Moreover, the polymer can be confined to pores that are smaller than 20 nm, a range that has not been explored extensively in prior studies. A bilayer

of PE and SiO_2 NPs is produced by spin coating and loading (see experimental section). The average size of NPs and the pore size of random packings of SiO_2 NPs are summarized in Table 5.1. Linear PEs of two different molecular weights (weight average molecular weight (M_w) = 27 kDa and 50 kDa) and commercial low-density polyethylene (LDPE) are used.

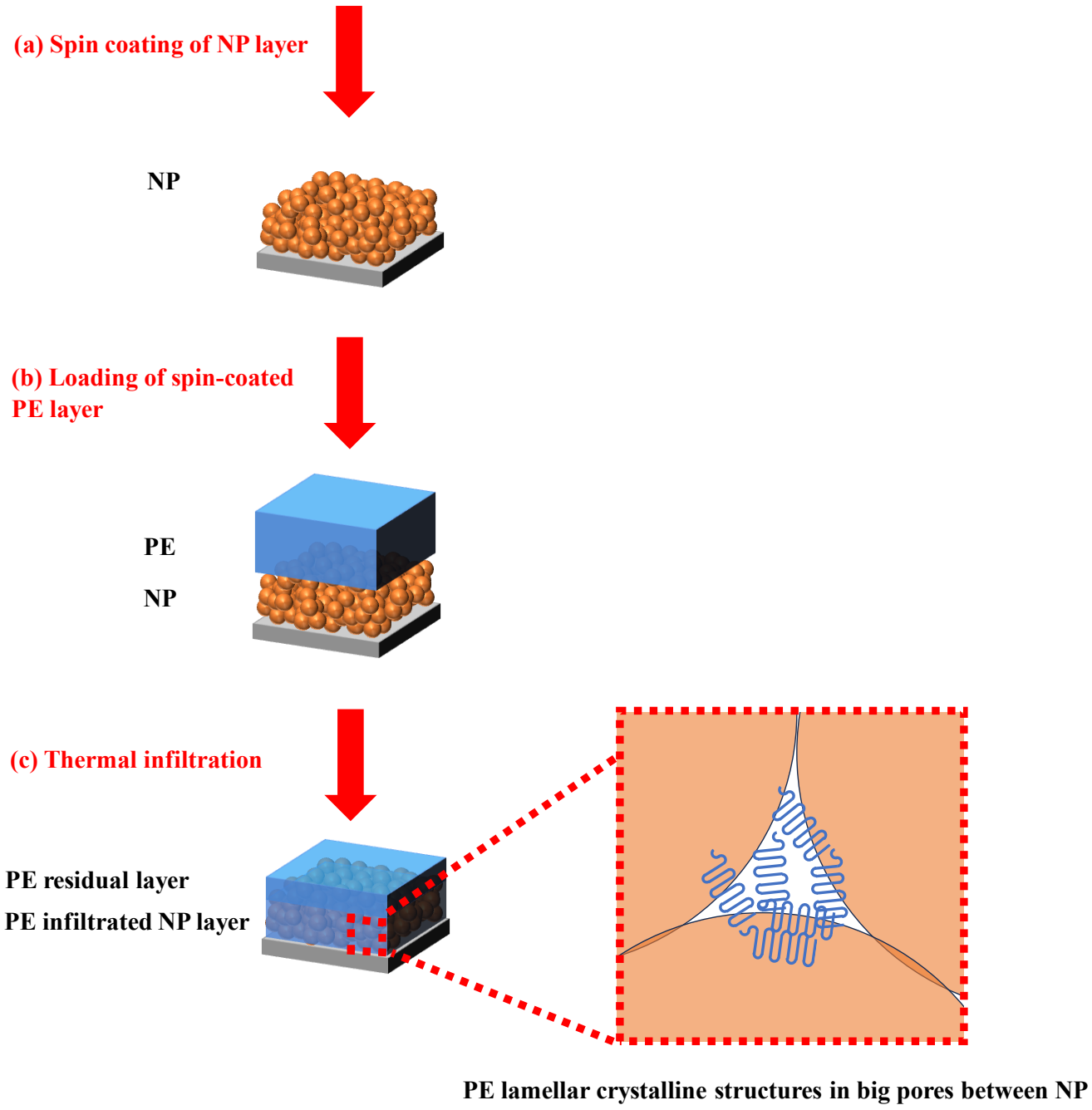

Figure 5.1 Schematic illustration of sample preparation for melting point characterization.

Table 5.1 Average pore size (D_{pore}) based on the random packing of SiO_2 NPs.[56]

D of NP(nm)	D_{pore}(nm)
7	2.0
17	4.9
25	7.2
61	17.6

To determine the melting point of PE confined in these random packings of SiO_2 NPs, we monitor the changes in the refractive index of the PE-infiltrated PE packings using spectroscopic ellipsometry. Spectroscopic ellipsometry has previously been used to determine the melting temperature of various materials including indium, zinc and water with high accuracy.[157] Ellipsometry also has been used to detect the shift in the glass transition of amorphous polymers.[54,78] Thus we test the possibility of using spectroscopic ellipsometry to detect the temperatures of crystallization and melting for PE. As shown in Figure 5.2 (a), abrupt changes in the refractive index of the PE-filled NP packing is observed during cooling and heating. The 115±7nm-thin film of PE has a melting point (T_m) of 112°C and crystallization point (T_c) of

99°C based on these thermograms.[150,158] A heating and cooling temperature scan of a neat SiO_2 NP packing does not show any abrupt transitions as expected.

We subject a PE-filled ~223-nm SiO_2 NP packing to a heating and cooling cycle to determine T_m and T_c. The refractive index decreases as the temperature is increased and exhibits an abrupt change in the slope at 87°C indicating melting of the PE crystalline domains as shown in Figure 5.2 (b). Likewise, an abrupt change, due to crystallization of PE in the NP packing, is observed at 83°C in the cooling process. The same method based on a temperature scan of PE-filled NP packing is performed for NPs of different sizes to determine T_m and T_c of PE under confinement.

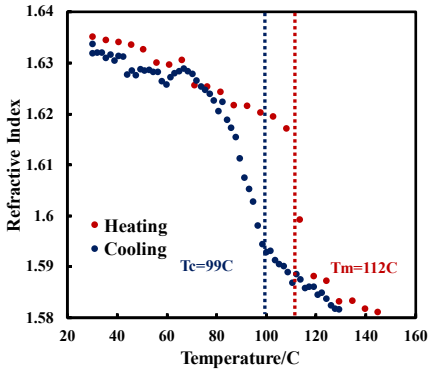

(a)

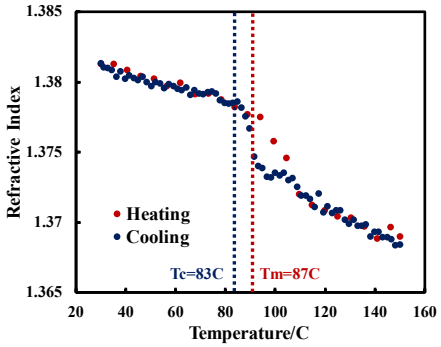
1.385
1.38
1.375
1.37
1.365
Refractive Index
Heating
Cooling
Tc=83C
Tm=87C
20
40
60
80
100
120
140
160
Temperature/C

(b)

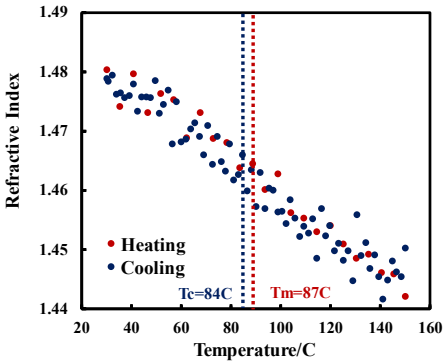
1.49
1.48
1.47
1.46
1.45
1.44
Refractive Index
Heating
Cooling
Tc=84C
Tm=87C
20
40
60
80
100
120
140
160
Temperature/C

(b)

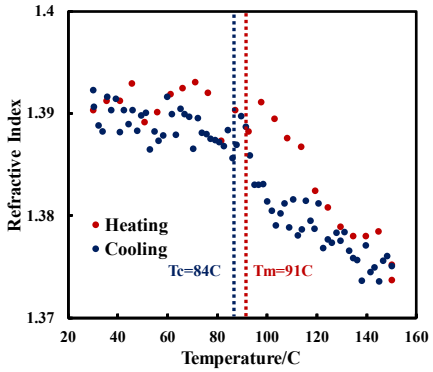

(c)

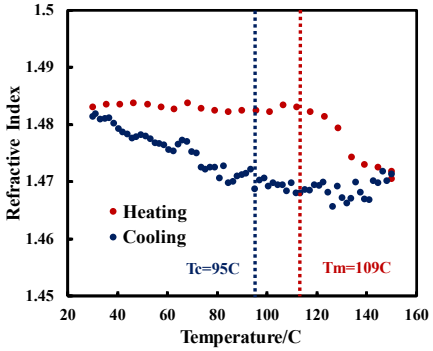

(d)

Figure 5.2 The melting curves of refractive index for 50k PE & (a)7nm, (b)17nm, (c)25nm, and (d) 61nm NP nanocomposite and (e) 50kg/mol PE in cooling &heating cycling.

We also study the effect of surface chemistry by modifying the surface of the NP packings with sub-1 nm layer of TiO_2 and $CaCO_3$ using atomic layer deposition (ALD). ALD is a particularly well-suited method for this study, as the method allows for deposition of ultra-thin layers without changing the structure of porous materials. We have recently shown that sub-1 nm ALD layers

on the surface of NPs can dramatically change the interactions between polymers and NPs. We modify random packings of silica NP with TiO_2 and $CaCO_3$ using ALD. Our results show that PE has because of their various interactions with PE. [38] As our previous chapter shows, the material growth rate is linearly fitted for both pellets from weight gain and thin films from the refractive index. The coating thickness is designed to gain one monolayer coverage which is 0.35 nm for TiO_2[83] and 0.40 nm for $CaCO_3$[85]. The growth rate of the ALD layers is not affected by the size of NPs.

The melting curves for ALD-treated 25nm-NP films with 50kg/mol PE are shown in Figure 5.3. The Figure 5.3 (a) and Figure 5.3 (b) show the melting and crystalline points of PE inside TiO_2-ALD and $CaCO_3$-ALD 25nm-NP nanocomposite, respectively. The observed melting characteristics are notably similar to those in silica NP, suggesting that surface chemistry modifications do not significantly impact these properties.

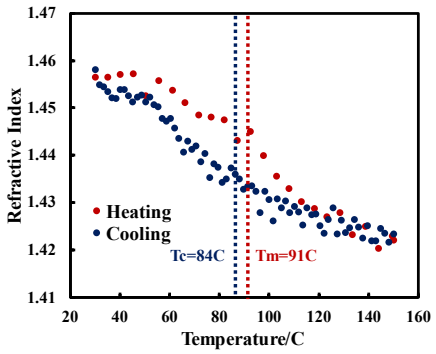

(a)

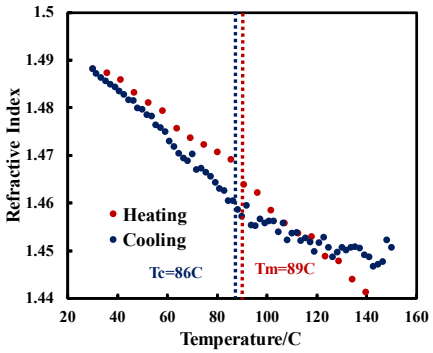

(b)

Figure 5.3 The melting curves of refractive index for 50k PE & 25nm (a)TiO_2-ALD, (b) $CaCO_3$-ALD 25nm-NP nanocomposite in cooling &heating cycling.

The depressions in T_m and T_c are plotted against 1 over the pore size (1/D) for different combinations of PE and NPs as shown in Figure 5.4. The melting point decrease is linearly proportional to 1/D when 1/D is less than 0.16 and 0.10 for T_m and T_c respectively. This trend is because of the decreased crystalline domain size in the decreased pore sizes, which has been observed in lower 1/D situations. [137] After 1/D reaches the turning point at ~6 and 10nm for T_m and T_c respectively, the decrease saturates to a value of 22°C for T_m and 16°C for T_c because of the smaller pore sizes in comparison to the minimum crystalline size, lamellar size. The new observation of the initial rise and subsequent plateau is a unique contribution to the understanding of polymer behavior under confinement.

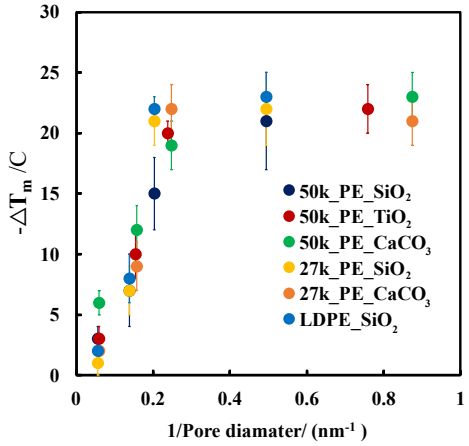

(a)

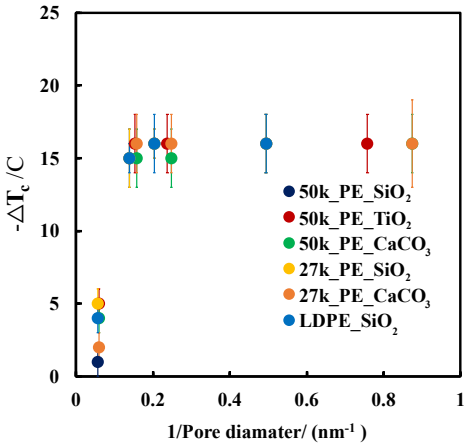

(b)

Figure 5.4 (a) -△T_m, (b) -△T_c of PE in different NP nanocomposite vs 1/Pore diameter.

For different solid surfaces, the decrease of melting points shows the same trend for various PEs including commercial linear ones and low-density polyethylene(LDPE), indicating that the

surface chemistry doesn't affect the melting point nor the crystallinity of polyethylene, even though PE demonstrates different interfacial energies on SiO_2, TiO_2, and $CaCO_3$. [39]

Prior studies have shown that various characterizations including diffraction, scattering, nuclear magnetic resonance, and electron microscopy can characterize PE crystalline structure but XRD is particularly effective for crystal forms due to its precision in distinguishing crystalline arrangements. [147,155,159–164]Thus we perform XRD to probe the size of crystals in PE. As shown in Figure 5.5, the XRD profile of unconfined 50k-PE, 27k-PE, and LDPE show the characteristic peaks at 21.2° and 23.1°, which are indicative of the (110) and (200) planes, representing crystal transitions including the pseudo-hexagonal and the orthorhombic crystal structures.[159] In accordance with the Scherrer equation, the analysis of the experimental data reveals crystal sizes of 18 nm and 11 nm shown in Table 5.2. The crystalline lamellar size (L) is 11nm[153] for 27 and 50kg/mol, and LDPE which is confirmed by the same trend with the PE of different Mw.

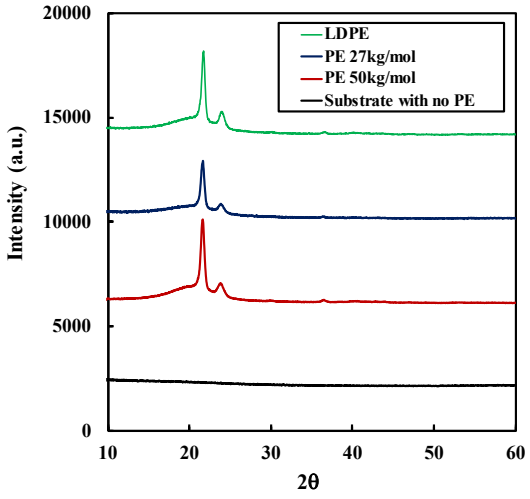

Figure 5.5 XRD of different Pes.

Table 5.2 Analysis of XRD.[159]

PE Sample	2θ	D/ nm
50kg/mol PE	21.57	16.70±0.07
	23.76	10.03±0.09
27kg/mol PE	21.58	17.04±0.16
	23.81	11.19±0.27
LDPE	21.68	18.01±0.15
	23.92	11.88±0.17

To enable reliable XRD of confined PE, we increase the amount of infiltrated PE by inducing infiltration of LDPE into macroscopic pelletized NP packing. LDPE in the 7 and 25nm NP packings with a pore size of 2 and 8nm does not show a clear crystalline peak, whereas the 61nm NP packings with a pore size of 18nm show a crystalline peak at 21° of PE as shown in Figure 5.6. Crystalline peaks are observed for LDPE in the 61 nm packing; however, their intensity is substantially reduced compared to those from the bulk LDPE as shown in Figure 5.6. These results indicate that the PE loses the crystalline structure when the pore size is smaller than the crystalline size.

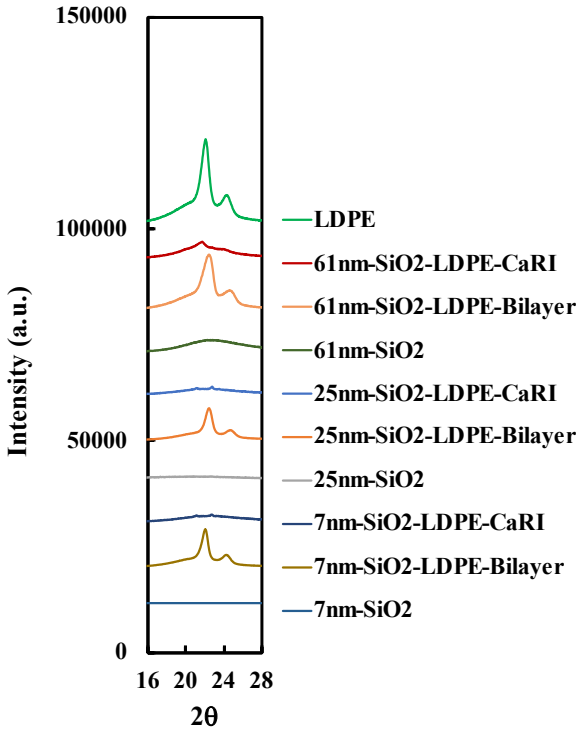

Figure 5.6 XRD of LDPE, LDPE atop NP bilayer, and LDPE infiltrated NP packing.

5.4. Conclusions

We have demonstrated that the melting and crystallization temperature of PE is strongly affected by confinement and that this effect saturates when the pore size becomes equivalent to the size of PE crystals in bulk. The change of melting point in the confined system can be observed with an ellipsometer with annealing and cooling cycles. When the pore size is larger than the lamellar

size, the change of melting point increases because the crystalline domain size is decreased in more confined pores in a linear fitting. When the pore size is smaller than the minimum crystalline domain size as the lamellar size, the change of the melting point leads to a saturation value of 22C while the crystalline point leads to a saturation of 16C.

As pore size reduces to the scale of PE's lamellar size, there's a pronounced alteration in the crystalline domain structure due to spatial confinement. When pore sizes decrease to the scale of PE’s lamellar size, significant changes occur in the crystalline domain structure under confinement. This results in a linear decrease in melting points within larger pores, indicative of diminishing crystalline domain sizes. However, when pores are smaller than PE's lamellar size, a threshold is reached where further size reduction doesn't significantly affect the crystallinity. Here, the melting point stabilizes as a limit to the influence of confinement on the crystalline structure of PE. This behavior can motivate deeper insight into the complex relationship between polymer crystallinity and the confinement effect.

CHAPTER 6. SUMMARY AND OUTLOOK

6.1 Summary

This thesis has comprehensively explored the polymer-solid interactions and the the effective polymer properties change including melting point and crystalline point under extreme nanoconfinement.

The chapter 2 talks about the Interactions between Polymer melt and Porous Solids. Understanding and modulating the interactions between molten polymers and porous solids is important for numerous processes and phenomena including catalytic conversion of polymers and fabrication of nanocomposites and nanostructured materials. Although changing the surface composition of pores would enable modulation of interactions between polymer and nanoporous solids, it is challenging to achieve such a control without inducing significant changes to the size and structure of nanopores. In this work, we demonstrate that the interactions between molten polystyrene (PS) and disordered packings of SiO_2 nanoparticles (NPs) can be modulated by changing the surface composition of the NPs using atomic layer deposition (ALD). A disordered packing of silica NPs is modified with varying surface coverages of TiO_2, WO_3 and $CaCO_3$, with coverages estimated by the mass gain and the refractive index change of NP packings. Based on the time required to fully infiltrate these ALD-modified NP packings via capillarity, the contact angles for PS on different surfaces prepared via ALD are determined. The contact angle gradually changes from that of pure SiO_2 to that of the fully covered surfaces. The contact angles

for PS on SiO_2, TiO_2, WO_3 and $CaCO_3$ are found to be 20°, 62°, 70° and 10°, respectively. Interestingly, the contact angles and interfacial energies between PS and the ALD-modified surfaces do not correlate strongly with the water contact angle of these surfaces; thus, caution must be exercised in predicting how a polymer would wet or interact with porous solids solely based on their hydrophilicity. The method presented in this work can be extended to study the interactions between a wide range of polymers and surfaces in porous media, which will have important implications for designing new catalytic materials for polymer upcycling reactions as well as novel NP-polymer composite films and membranes with enhanced mechanical and transport properties.

The Chapter 3 talks about the understanding polymer-porous solid Interactions via gas. Understanding the interactions between molten polymers and inorganic porous solids is critical for the heterogeneous catalytic conversion of waste polymers into useful chemicals and the fabrication of nanocomposites and nanostructured polymers. Developing experimental and theoretical approaches to quantify and understand polymer-surface interactions would be extremely useful for the design of new catalysts and composites. Here, we demonstrate that the interfacial energy between molten polystyrene (PS) or polyethylene (PE) and various inorganic surfaces prepared via atomic layer deposition (ALD) such as SiO_2, TiO_2, WO_3, and $CaCO_3$ are correlated with the adsorption of small molecules that bear structural similarity to the repeat unit of the two polymers. The interfacial energy inferred from the dynamics of polymer infiltration into ALD-modified porous solids is compared with the heats of adsorption of small molecules on mesoporous silica (SBA-15) modified with ALD. Both our experimental and computational

results suggest a strong correlation between the polymer-solid interfacial energy and the adsorption strengths of their respective small molecules on the same surface. These results highlight that even though there are no specific modes of interaction between the polymers and the inorganic surfaces, their interaction energies vary significantly and are dominated by differences in the enthalpic interactions between each repeat unit and the solid surface. Besides providing a novel method for measuring the polymer-solid interaction, this work bridges the gap between the behavior of macromolecules on solid surfaces and the adsorption properties of small gas molecules. This understanding will have important implications for designing new catalysts for polymer upcycling and composite membranes for gas and potentially polymer separation.

The Chapter 4 talks about the effective viscosity of polyethylene under extreme nanoconfinement, a significant increase in polyethylene's effective viscosity was observed and a generalized formalism was developed to explain this phenomenon. Understanding polymer transport in nanopores is crucial for optimizing heterogeneously catalyzed processes in polymer upcycling and fabricating high-performance nanocomposite films and membranes. Although confined polymer dynamics have been extensively studied, the behavior of polyethylene (PE)—the most widely used commodity polymer—in pores smaller than 20 nm remains largely unexplored. We investigate the effects of extreme nanoconfinement on PE transport using capillary rise infiltration (CaRI) in silica nanoparticle packings with pore radii ranging from ~1 and ~9 nm. Using *in situ* ellipsometry and the Lucas-Washburn model, we discover a previously unknown inverse relationship between effective viscosity (η_{eff}) and pore radius (R_{pore}). Additionally, we determine that PE transport under these extreme conditions is primarily

governed by physical confinement, rather than pore surface chemistry. We refine an existing theory to provide a generalized formalism to describe the polymer transport dynamics over a wide range of pore radii (from 1 nm and larger). Our results offer valuable insights for optimizing catalyst supports in polymer upcycling and improving infiltration processes for nanocomposite fabrication.

The Chapter 5 shows the unfinished work that the confined melting point and crystalline point of polyethylene decrease inside nanocomposite. This decrease linearly correlates with pore size reduction but reaches a saturation point when the pore diameter is approximately 8 nm and 10nm for confined melting point and crystalline point respectively, which is similar to the crystalline lamellar size of PE as 11nm.This phenomenon is consistent across different types of PE and is not affected by the solid surface chemistry. These findings provide valuable insights into the confinement effect on polymer properties, which can benefit the reactor design of polymer-involved reactions from manufacturing to upcycling.

6.2 Outlook 1: Preliminary Study on Hydrogen Solubility of Polyethylene inside Porous Material via Our Custom-Built Quartz Crystal Microbalance (QCM)

6.2.1 Introduction and motivation to study hydrogen solubility of polymer

Hydrogen solubility in polymer melt or solution is a crucial factor in various chemical processes applied to catalytic recycling of polymers. These hydrogen-involved upcycling techniques include thermal pyrolysis[1], catalytic depolymerization[165], hydrocracking[8,9,166], hydrogenolysis[10,14,18,20,61,126,167–169], and dehydrogenation[170] processes, where the existence and diffusion of hydrogen significantly affect the reactivity and selectivity in the transformation of polymers into high-added value chemicals. In hydrogen-involving reactions for thermal pyrolysis[1], catalytic depolymerization[165], hydrocracking[8,9,166], and hydrogenolysis[10,14,18,20,61,126,167–169,171], high hydrogen solubility correlates with increased reactivity. This is because the availability of hydrogen can accelerate reaction kinetics, leading to more efficient breakdown or restructuring of polymer chains. However, for hydrogen-producing reactions such as dehydrogenation[170], high solubility decreases the reactivity because the by-product hydrogen in the polymer melt can impede the removal of hydrogen molecules from the polymer chain, slowing down the dehydrogenation process. Although there has been some research without any additive hydrogen for polymer upcycling[172], most hydrogen-involved reactions need additional hydrogen to tune the experiments. Although some studies focus on how hydrogen pressure impacts various reactions involving polymers, limited information is available on the effect of hydrogen solubility in polymers on the selectivity of polymer upcycling reactions.[171] Indeed, while pressure and solubility are interrelated, the specific effects of solubility on selectivity need more focused investigation in this field. This gap in research motivates us to gain a deeper understanding of how hydrogen solubility influences polymer upcycling.

Understanding and controlling hydrogen solubility in polymer melts is vital for optimizing these recycling processes. However, most existing research focuses primarily on the bulk properties of polymers or their surface interactions.[173–175] Studies exploring the behavior of polymers confined within porous materials, especially regarding hydrogen solubility, are relatively scarce. As the confinement within pores can dramatically alter the interaction dynamics of polymers with hydrogen and affect the efficiency of catalytic recycling processes, it is worthwhile to conduct a model study.

The interaction of hydrogen with polymers, especially within confined spaces, is a topic of significant interest, particularly in fields like energy storage and catalysis. Understanding these interactions at a molecular level can lead to advancements in material design for hydrogen storage technologies. Polyethylene, due to its widespread use and unique properties for polymer recycling, is an ideal candidate for such a study.

6.2.2 Custom-Built QCM to Measure the Gas Solubility in Polymer: Design and Functionality

The quartz crystal microbalance (QCM) is a sensitive instrument capable of detecting minute changes in mass per area from the frequency shift of a quartz crystal sensor at the nanogram level has been used to measure gas solubility including hydrogen.[176] Due to its high sensitivity and reliability, it has been widely applied to measuring the adsorption and desorption of molecules on surfaces. This principle has been used to detect the sorption of gas molecules into

thin films made of polymers and lipids. These sorption curves can be used to determine the gas diffusivity and solubility in a variety of materials such as polymers.

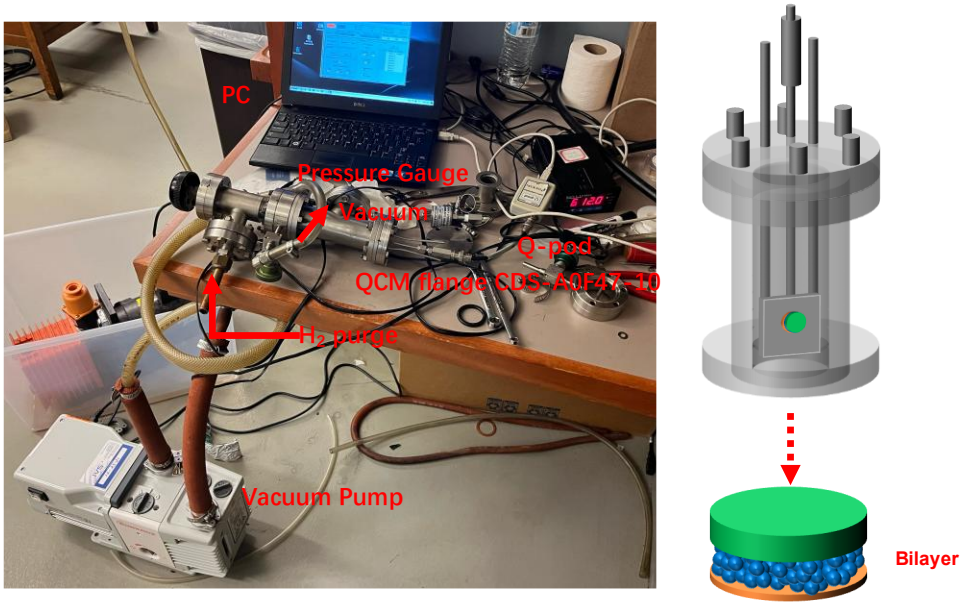

Figure 6.1 Design of the QCM system.

We have set up a custom-built QCM system to determine hydrogen solubility in polyethylene—a common polymer—when subjected to the unique environment of nanoconfinement within porous materials. We have purchased a QCM flange with a CDS-A0F47-47 sensor from *Inficon Inc.* and fabricated a sorption chamber with a parr reactor as shown in Figure 6.1.

To obtain accurate H_2 solubility, it is critical to control the pressure and temperature of the chamber. In the past several months, I have successfully made the high vacuum less than 50 mmtorr (6.7 Pa) and made some preliminary measurements of H_2 solubility in pure PE at room

temperature. This system will enable determination of H2 and other gas solubility in PE confined in nanoparticle packings with different pore sizes. The QCM sorption system can be further improved by incorporating a thermocouple for precise temperature regulation. This setup will need to be rigorously tested and validated across a wide temperature range from 20°C to 200°C, and under varied pressure conditions spanning 1 kPa to 100 MPa.

6.2.3 Experimental Setup of QCM and Methodology Based on Sauerbrey Equation

This section outlines the experimental procedure, including the preparation of polyethylene samples [38,39], and QCM measurement of hydrogen sorption. SiO_2 NP films are spin-coated on O_2-plasma-treated Inficon crystals (008-010-G10, Gold 6MHz) for QCM as same as silicon wafers in the previous papers at ~220nm and ~450nm. Then the spin-coated 130nm-thickness PS and PE films are peeled off from the silicon wafers in water due to their hydrophobicity and then loaded onto the NP films. [38,39] Then the bilayer is annealed above the melting point of PE or glass transition temperature of PS, which can infiltrate the polymer into the NP packing via capillary force as a CaRI procedure to make a nanocomposite. The extra polymer layer is removed by plasma and only a nanocomposite layer on the quartz is left and checked via ellipsometry. As a start, the only polymer coated crystal is also fabricated as a control to validate the solubility measurements.[174,177,178]

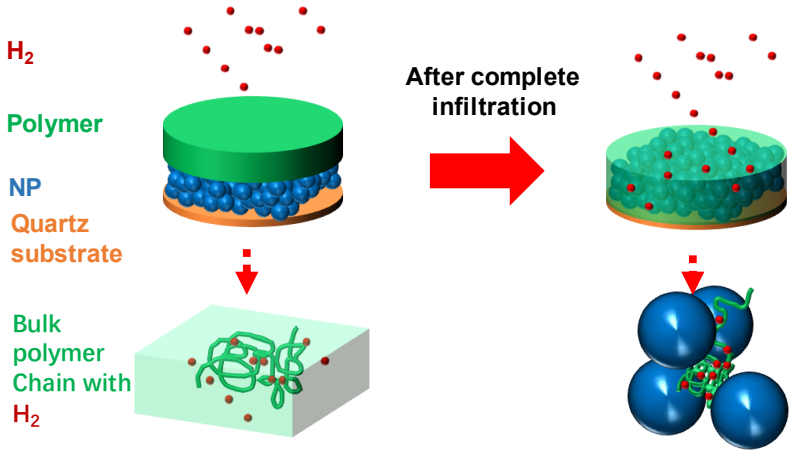

Figure 6.2 Sketch of coating on quartz for QCM.

Then the coated crystal as shown in Figure 6.2 is installed on the QCM flange which is connected to Parr reactor with all the connections as shown in the Figure 6.1. The QCM flange is connected to a PC via a Q-pod panel. The sealed system is evacuated by the oil pump until the limit of 50 mmtorr and then introduced by the hydrogen. The QCM's sensitivity to mass changes enables precise measurements of hydrogen uptake in polymer within the porous structures. The parameters monitored by the QCM, such as frequency shifts Δf [Hz] corresponding to mass changes Δm [g], are analyzed by Sauerbrey equation as **Eq (38)**:

$$\Delta m = \frac{-A \cdot \Delta f \cdot \sqrt{\mu_q \cdot \rho_q}}{2 f_0^{\,2}} \quad (38)$$

where, f_0 is the frequency of the quartz crystal prior to a weight change ($\approx 6.0 \times 10^6$ [Hz]), μ_q is the shear modulus of quartz (2.947×10^{13} [g m^{-1} s^{-2}]), μ_q is the density of quartz (2.648×10^6 [g m^{-3}]), and A is the electrode area (4.9×10^{-5} [m^2]).[179–181] Sauerbrey equation demonstrates a

linear proportional correlation between frequency change and mass change of a crystal with a high intrinsic precise frequency along with a high sensitivity.

6.2.4 Preliminary Qualitative results and Future Work

Initial results from the QCM experiments are not presented this time because we need to repeat more to confirm our results, but we have some qualitative results. We have found some interesting trends that the hydrogen solubility of 50kg/mol polyethylene increases when confined in smaller pores from 20 to 2nm diameter. The observed hydrogen solubility of polyethylene in various porous materials needs further investigation. We aim to examine the relationship between hydrogen solubility, polymer confinement, solid surface chemistry and the characteristics of the porous structures. A comprehensive analysis will be conducted to connect the measured hydrogen solubility under confinement. Possible mechanisms behind the observed phenomena are explored, and the results will be compared with existing literature.

6.2.5 Summary

The integration of custom-built QCM technology in studying hydrogen-polymer interactions within nanoconfined spaces is highlighted as a significant step forward in this research area. The challenges faced during the study, including issues with QCM sensitivity and sample preparation, are discussed. The limitations of the current study are acknowledged, providing a realistic perspective on the findings. Potential areas for future research are identified, such as exploring different types of polymers and porous materials or scaling the experimental setup for larger sample sizes.

We have done paper research about the significance of hydrogen solubility in polymer-involved reactions, highlighting its impact on reactivity and selectivity in polymer upcycling techniques. This outlook details the design and functionality of the innovative QCM system and explains the experimental setup and methodology based on the Sauerbrey equation. Preliminary qualitative results suggest a possible increase in hydrogen solubility in polyethylene confined in smaller pores. This outlook concludes by acknowledging the challenges, the limitations of the current study, and potential directions for future research.

6.3 Outlook 2: Big Picture for Understanding and Controlling Behavior of Polymers in Porous Media

From the past to the future, there are various meaningful directions for understanding and controlling of polymers in porous media. The first challenge is seriously continuing to characterize, understand, and control the solubility of hydrogen or other small molecules such as solvent or other products of low M_w in polymer confined in porous media, which can benefit most reactions in catalytic recycling of polymer because of the wide involvement with small molecules. However, it remains more challenging in our measurement techniques such as QCM for better accuracy and reliability in hydrogen solubility studies. In comparison with different pore structures and surface chemistry, it is believed that some scientific trends correlated to these factors may affect reactivity and selectivity in various ways. The smaller pores may enhance the contact surface area but may decrease the diffusion of small molecules in polymers and increase

the controlling of conformation, which may cause a tradeoff between reactivity and selectivity and needs deeper investigation.

The polymer dynamics needs further exploration into polymer dynamics within various porous structures and polymer mixtures to model and pilot the industrial application, particularly in polymer upcycling reactions.

The generalized model for effective viscosity needs one more step to check the extreme sub-nanometer confinement environment. We are also limited to our system though our pores can be smaller than most of the reference via random packing of monodispersed NP.

Our methodology of polymer physics in nanoporous materials can assist in designing high-throughput and automatic systems to screen polymer-contained porous materials, which opens another door in conventional fields such as reduced-novel-metal catalysis.

In summary, this thesis provides significant advancements in the understanding of polymer-porous solid interactions and effective polymer properties, drawing a big picture for future innovations in polymer physics in porous media and material science and engineering of nanocomposite.

BIBLIOGRAPHY

(1) Geyer, R. Production, Use, and Fate of Synthetic Polymers. In *Plastic Waste and Recycling*; Elsevier, 2020; pp 13–32. https://doi.org/10.1016/B978-0-12-817880-5.00002-5.

(2) Oberoi, G.; Garg, A. *Single-Use Plastics: A Roadmap for Sustainability? (Rev. 2)*; 2021; p 585.

(3) Chen, H.; Wan, K.; Zhang, Y.; Wang, Y. Waste to Wealth: Chemical Recycling and Chemical Upcycling of Waste Plastics for a Great Future. *ChemSusChem* **2021**, 1–15. https://doi.org/10.1002/cssc.202100652.

(4) Ragaert, K.; Delva, L.; Van Geem, K. Mechanical and Chemical Recycling of Solid Plastic Waste. *Waste Manag.* **2017**, *69*, 24–58. https://doi.org/10.1016/j.wasman.2017.07.044.

(5) Martín, A. J.; Mondelli, C.; Jaydev, S. D.; Pérez-Ramírez, J. Catalytic Processing of Plastic Waste on the Rise. *Chem* **2021**, *7* (2020), 1–47. https://doi.org/10.1016/j.chempr.2020.12.006.

(6) Kots, P. A.; Vance, B. C.; Vlachos, D. G. Polyolefin Plastic Waste Hydroconversion to Fuels, Lubricants, and Waxes: A Comparative Study. *React. Chem. Eng.* **2022**, *7* (1), 41–54. https://doi.org/10.1039/d1re00447f.

(7) Zhuo, C.; Levendis, Y. A. Upcycling Waste Plastics into Carbon Nanomaterials: A Review. *J. Appl. Polym. Sci.* **2014**, *131* (4). https://doi.org/10.1002/app.39931.

(8) Liu, S.; Kots, P. A.; Vance, B. C.; Danielson, A.; Vlachos, D. G. Plastic Waste to Fuels by Hydrocracking at Mild Conditions. *Sci. Adv.* **2021**, *7* (17), 1–10. https://doi.org/10.1126/sciadv.abf8283.

(9) Vance, B. C.; Kots, P. A.; Wang, C.; Hinton, Z. R.; Quinn, C. M.; Epps, T. H.; Korley, L. S. T. J.; Vlachos, D. G. Single Pot Catalyst Strategy to Branched Products via Adhesive Isomerization and Hydrocracking of Polyethylene over Platinum Tungstated Zirconia. *Appl. Catal. B Environ.* **2021**, *299*, 120483. https://doi.org/10.1016/j.apcatb.2021.120483.

(10) Wang, C.; Xie, T.; Kots, P. A.; Vance, B. C.; Yu, K.; Kumar, P.; Fu, J.; Liu, S.; Tsilomelekis, G.; Stach, E. A.; Zheng, W.; Vlachos, D. G. Polyethylene Hydrogenolysis at Mild Conditions over Ruthenium on Tungstated Zirconia. *JACS Au* **2021**, *1* (9), 1422–1434. https://doi.org/10.1021/jacsau.1c00200.

(11) Prajapati, R.; Kohli, K.; Maity, S. K. Slurry Phase Hydrocracking of Heavy Oil and Residue to Produce Lighter Fuels: An Experimental Review. *Fuel*. Elsevier March 2021, p 119686. https://doi.org/10.1016/j.fuel.2020.119686.

(12) Botchwey, C.; Dalai, A. K.; Adjaye, J. Product Selectivity during Hydrotreating and Mild Hydrocracking of Bitumen-Derived Gas Oil. *Energy and Fuels* **2003**, *17* (5), 1372–1381. https://doi.org/10.1021/ef020214x.

(13) Suganuma, S.; Katada, N. Innovation of Catalytic Technology for Upgrading of Crude Oil in Petroleum Refinery. *Fuel Processing Technology*. Elsevier November 2020, p 106518. https://doi.org/10.1016/j.fuproc.2020.106518.

(14) Ruppert, A. M.; Weinberg, K.; Palkovits, R. Hydrogenolysis Goes Bio: From Carbohydrates and Sugar Alcohols to Platform Chemicals. *Angewandte Chemie - International Edition*. John Wiley & Sons, Ltd March 2012, pp 2564–2601. https://doi.org/10.1002/anie.201105125.

(15) Brody, A. L. Packaging of Foods. In *Encyclopedia of Food Microbiology: Second Edition*; Elsevier Inc., 2014; pp 1017–1027. https://doi.org/10.1016/B978-0-12-384730-0.00244-5.

(16) Feldman, D. Polyblend Compatibilization. *J. Macromol. Sci. - Pure Appl. Chem.* **2005**, *42 A* (5), 587–605. https://doi.org/10.1081/MA-200056331.

(17) Wu, Y.; Ye, K.; Liu, Z.; Wang, M.; Chee, K. W. A.; Lin, C.-T.; Jiang, N.; Yu, J. Effective Thermal Transport Highway Construction within Dielectric Polymer Composites: Via a Vacuum-Assisted Infiltration Method. *J. Mater. Chem. C* **2018**, *6* (24), 6494–6501. https://doi.org/10.1039/c8tc01464g.

(18) Tennakoon, A.; Wu, X.; Paterson, A. L.; Patnaik, S.; Pei, Y. Catalytic Upcycling of High-Density Polyethylene via a Processive Mechanism. *Nat. Catal.* **2020**, *3* (11), 893–901. https://doi.org/10.1038/s41929-020-00519-4.

(19) Fuentes-Ordóñez, E. G.; Salbidegoitia, J. A.; González-Marcos, M. P.; González-Velasco,

J. R. Transport Phenomena in Catalytic Hydrocracking of Polystyrene in Solution. *Ind. Eng. Chem. Res.* **2013**, *52* (42), 14798–14807. https://doi.org/10.1021/ie401968r.

(20) Kots, P. A.; Liu, S.; Vance, B. C.; Wang, C.; Sheehan, J. D.; Vlachos, D. G.; A. Kots, P.; Liu, S.; C. Vance, B.; Wang, C.; D. Sheehan, J.; G. Vlachos, D. Polypropylene Plastic Waste Conversion to Lubricants over Ru/TiO 2 Catalysts. *ACS Catal.* **2021**, *11* (13), 8104–8115. https://doi.org/10.1021/acscatal.1c00874.

(21) Zhang, J.; Zhang, L. Polystyrene/TiO2 Nanocomposite Coatings to Inhibit Corrosion of Aluminum Alloy 2024-T3. *ACS Appl. Nano Mater.* **2019**, *2* (10), 6368–6377. https://doi.org/10.1021/acsanm.9b01358.

(22) Ulrich, N.; Spende, A.; Burr, L.; Sobel, N.; Schubert, I.; Hess, C.; Trautmann, C.; Toimil-Molares, M. E.; Toimil-molares, M. E. Conical Nanotubes Synthesized by Atomic Layer Deposition of Al2o3, Tio2, and Sio2 in Etched Ion-track Nanochannels. *Nanomaterials* **2021**, *11* (8), 1874. https://doi.org/10.3390/nano11081874.

(23) Azimi, G.; Dhiman, R.; Kwon, H. M.; Paxson, A. T.; Varanasi, K. K. Hydrophobicity of Rare-Earth Oxide Ceramics. *Nat. Mater.* **2013**, *12* (4), 315–320. https://doi.org/10.1038/nmat3545.

(24) Kang, Y.; Li, M.; Cai, Y.; Cargnello, M.; Diaz, R. E.; Gordon, T. R.; Wieder, N. L.; Adzic, R. R.; Gorte, R. J.; Stach, E. A.; Murray, C. B. Heterogeneous Catalysts Need Not Be so “Heterogeneous”: Monodisperse Pt Nanocrystals by Combining Shape-Controlled

Synthesis and Purification by Colloidal Recrystallization. *J. Am. Chem. Soc.* **2013**, *135* (7), 2741–2747. https://doi.org/10.1021/ja3116839.

(25) Qiang, Y.; Turner, K. T.; Lee, D. Role of Polymer-Nanoparticle Interactions on the Fracture Toughness of Polymer-Infiltrated Nanoparticle Films. *Macromolecules* **2023**, *56* (1), 122–135. https://doi.org/10.1021/acs.macromol.2c01567.

(26) Hor, J. L.; Jiang, Y.; Ring, D. J.; Riggleman, R. A.; Turner, K. T.; Lee, D. Nanoporous Polymer-Infiltrated Nanoparticle Films with Uniform or Graded Porosity via Undersaturated Capillary Rise Infiltration. *ACS Nano* **2017**, *11* (3), 3229–3236. https://doi.org/10.1021/acsnano.7b00298.

(27) Hor, J. L.; Wang, H.; Fakhraai, Z.; Lee, D. Effects of Polymer-Nanoparticle Interactions on the Viscosity of Unentangled Polymers under Extreme Nanoconfinement during Capillary Rise Infiltration. *Soft Matter* **2018**, *14* (13), 2438–2446. https://doi.org/10.1039/c7sm02465g.

(28) Venkatesh, R. B.; Han, S. H.; Lee, D. Patterning Polymer-Filled Nanoparticle Films via Leaching-Enabled Capillary Rise Infiltration (LeCaRI). *Nanoscale Horizons* **2019**, *4* (4), 933–939. https://doi.org/10.1039/c9nh00130a.

(29) Manohar, N.; Stebe, K. J.; Lee, D. Solvent-Driven Infiltration of Polymer (SIP) into Nanoparticle Packings. *ACS Macro Lett.* **2017**, *6* (10), 1104–1108. https://doi.org/10.1021/acsmacrolett.7b00392.

(30) Huang, Y. R.; Jiang, Y.; Hor, J. L.; Gupta, R.; Zhang, L.; Stebe, K. J.; Feng, G.; Turner, K. T.; Lee, D. Polymer Nanocomposite Films with Extremely High Nanoparticle Loadings via Capillary Rise Infiltration (CaRI). *Nanoscale* **2015**, *7* (2), 798–805. https://doi.org/10.1039/c4nr05464d.

(31) Venkatesh, R. B.; Zhang, T.; Manohar, N.; Stebe, K. J.; Riggleman, R. A.; Lee, D. Effect of Polymer-Nanoparticle Interactions on Solvent-Driven Infiltration of Polymer (SIP) into Nanoparticle Packings: A Molecular Dynamics Study. *Mol. Syst. Des. Eng.* **2020**, *5* (3), 666–674. https://doi.org/10.1039/c9me00148d.

(32) Yao, Y.; Butt, H. J.; Floudas, G.; Zhou, J.; Doi, M. Theory on Capillary Filling of Polymer Melts in Nanopores. *Macromol. Rapid Commun.* **2018**, *39* (14), 1–5. https://doi.org/10.1002/marc.201800087.

(33) Venkatesh, R. B.; Lee, D. Conflicting Effects of Extreme Nanoconfinement on the Translational and Segmental Motion of Entangled Polymers. *Macromolecules* **2022**, *55* (11), 4492–4501. https://doi.org/10.1021/acs.macromol.2c00145.

(34) Alexandris, S.; Papadopoulos, P.; Sakellariou, G.; Steinhart, M.; Butt, H.-J. J.; Floudas, G. Interfacial Energy and Glass Temperature of Polymers Confined to Nanoporous Alumina. *Macromolecules* **2016**, *49* (19), 7400–7414. https://doi.org/10.1021/acs.macromol.6b01484.

(35) Priks, H.; Butelmann, T.; Illarionov, A.; Johnston, T. G.; Fellin, C.; Tamm, T.; Nelson, A.;

Kumar, R.; Lahtvee, P. J. Physical Confinement Impacts Cellular Phenotypes within Living Materials. *ACS Appl. Bio Mater.* **2020**, *3* (7), 4273–4281. https://doi.org/10.1021/acsabm.0c00335.

(36) Wang, C.; Isaacson, S. G.; Wang, Y.; Lionti, K.; Volksen, W.; Magbitang, T. P.; Chowdhury, M.; Priestley, R. D.; Dubois, G.; Dauskardt, R. H. Surface Chemical Functionalization to Achieve Extreme Levels of Molecular Confinement in Hybrid Nanocomposites. *Adv. Funct. Mater.* **2019**, *29* (33), 1–9. https://doi.org/10.1002/adfm.201903132.

(37) Mateos-Langerak, J.; Bohn, M.; De Leeuw, W.; Giromus, O.; Manders, E. M. M.; Verschure, P. J.; Indemans, M. H. G.; Gierman, H. J.; Heermann, D. W.; Van Driel, R.; Goetze, S. Spatially Confined Folding of Chromatin in the Interphase Nucleus. *Proc. Natl. Acad. Sci. U. S. A.* **2009**, *106* (10), 3812–3817. https://doi.org/10.1073/pnas.0809501106.

(38) Ren, T.; Huang, R.; J. Gorte, R.; Lee, D. Modulating Interactions between Molten Polystyrene and Porous Solids Using Atomic Layer Deposition. *Langmuir* **2021**, *37* (49), 14520–14526. https://doi.org/10.1021/acs.langmuir.1c02604.

(39) Ren, T.; Wang, C. Y.; Huang, R.; Deng, C.; Xu, Y.; Majumder, A.; Ra, J.; Shen, K.; Vohs, J. M.; de Pablo, J. J.; Gorte, R. J.; Lee, D. Understanding Polymer-Porous Solid Interactions Based on Small Gas Molecule Adsorption Behavior. *Chem. Eng. J.* **2023**, *473* (August), 145220. https://doi.org/10.1016/j.cej.2023.145220.

(40) Young, T. An Essay on the Cohesion of Fluids. By Thomas Young. *Philos. Trans. R. Soc. London* **1805**, *95* (1805), 65–87.

(41) Venkatesh, R. B.; Manohar, N.; Qiang, Y.; Wang, H.; Tran, H. H.; Kim, B. Q.; Neuman, A.; Ren, T.; Fakhraai, Z.; Riggleman, R. A.; Stebe, K. J.; Turner, K.; Lee, D. Polymer-Infiltrated Nanoparticle Films Using Capillarity-Based Techniques: Toward Multifunctional Coatings and Membranes. *Annu. Rev. Chem. Biomol. Eng.* **2021**, *12* (1), 411–437. https://doi.org/10.1146/annurev-chembioeng-101220-093836.

(42) Bertei, A.; Nucci, B.; Nicolella, C. Effective Transport Properties in Random Packings of Spheres and Agglomerates. *Chem. Eng. Trans.* **2013**, *32*, 1531–1536. https://doi.org/10.33032/CET1332256.

(43) Shin, K.; Obukhov, S.; Chen, J.-T.; Huh, J.; Hwang, Y.; Mok, S.; Dobriyal, P.; Thiyagarajan, P.; Russell, T. P. Enhanced Mobility of Confined Polymers. *Nat. Mater.* **2007**, *6* (12), 961–965. https://doi.org/10.1038/nmat2031.

(44) Hor, J. L.; Wang, H.; Fakhraai, Z.; Lee, D. Effect of Physical Nanoconfinement on the Viscosity of Unentangled Polymers during Capillary Rise Infiltration. *Macromolecules* **2018**, *51* (14), 5069–5078. https://doi.org/10.1021/acs.macromol.8b00966.

(45) Nyden, M. R.; Gilman, J. Molecular Dynamics Simulations of the Thermal Degradation of Nano-Confined Polypropylene. *Mater. Today* **1998**, *1* (4), 12–14. https://doi.org/10.1016/s1369-7021(98)80019-9.

(46) Nichetti, D.; Manas-Zloczower, I. Viscosity Model for Polydisperse Polymer Melts. *J. Rheol. (N. Y. N. Y).* **1998**, *42* (4), 951–969. https://doi.org/10.1122/1.550908.

(47) Hor, J. L. Capillary Rise Infiltration (Cari) Of Polymer In Nanoparticle Packings Capillary Rise Infiltration (Cari) Of Polymer In Nanoparticle Packings, 2018.

(48) Hor, J. L. Capillary Rise Infiltration (Cari) Of Polymer In Nanoparticle Packings, 2018.

(49) Zohrevand, A.; Ajji, A.; Mighri, F. Microstructure and Properties of Porous Nanocomposite Films: Effects of Composition and Process Parameters. *Polym. Int.* **2014**, *63* (12), 2052–2060. https://doi.org/10.1002/pi.4761.

(50) Vogt, B. D. Mechanical and Viscoelastic Properties of Confined Amorphous Polymers. *J. Polym. Sci. Part B Polym. Phys.* **2018**, *56* (1), 9–30. https://doi.org/10.1002/polb.24529.

(51) Tang, S.; Greene, M. S.; Peng, X. H.; Liu, W. K.; Guo, Z. Y. Chain Confinement Drives the Mechanical Properties of Nanoporous Polymers. *Epl* **2014**, *106* (3), 36002. https://doi.org/10.1209/0295-5075/106/36002.

(52) Olad, A.; Rasouli, H. Enhanced Corrosion Protective Coating Based on Conducting Polyaniline/Zinc Nanocomposite. *J. Appl. Polym. Sci.* **2010**, *115* (4), 2221–2227. https://doi.org/10.1002/app.

(53) Barroso-Bujans, F.; Alegría, A.; Pomposo, J. A.; Colmenero, J. Thermal Stability of Polymers Confined in Graphite Oxide. *Macromolecules* **2013**, *46* (5), 1890–1898. https://doi.org/10.1021/ma302407v.

(54) Wang, H.; Qiang, Y.; Shamsabadi, A. A.; Mazumder, P.; Turner, K. T.; Lee, D.; Fakhraai, Z. Thermal Degradation of Polystyrene under Extreme Nanoconfinement. *ACS Macro Lett.* **2019**, *8* (11), 1413–1418. https://doi.org/10.1021/acsmacrolett.9b00649.

(55) Rubinstein, M.; Colby, R. H. *Polymer Physics*.

(56) Rouault, Y.; Assouline, S. A Probabilistic Approach towards Modeling the Relationships between Particle and Pore Size Distributions: The Multicomponent Packed Sphere Case. *Powder Technol.* **1998**, *96* (1), 33–41. https://doi.org/10.1016/S0032-5910(97)03355-X.

(57) Deka, B. K.; Mandal, M.; Maji, T. K. Effect of Nanoparticles on Flammability, UV Resistance, Biodegradability, and Chemical Resistance of Wood Polymer Nanocomposite. *Ind. Eng. Chem. Res.* **2012**, *51* (37), 11881–11891. https://doi.org/10.1021/ie3003123.

(58) Zhang, Y.; Fuentes, C. A.; Koekoekx, R.; Clasen, C.; Van Vuure, A. W.; De Coninck, J.; Seveno, D. Spreading Dynamics of Molten Polymer Drops on Glass Substrates. *Langmuir* **2017**, *33* (34), 8447–8454. https://doi.org/10.1021/acs.langmuir.7b01500.

(59) Pastore Carbone, M. G.; Tammaro, D.; Manikas, A. C.; Paterakis, G.; Di Maio, E.; Galiotis, C. Wettability of Graphene by Molten Polymers. *Polymer (Guildf).* **2019**, *180*, 121708. https://doi.org/10.1016/j.polymer.2019.121708.

(60) Erbil, H. Y. The Debate on the Dependence of Apparent Contact Angles on Drop Contact Area or Three-Phase Contact Line: A Review. *Surface Science Reports*. North-Holland December 2014, pp 325–365. https://doi.org/10.1016/j.surfrep.2014.09.001.

(61) Celik, G.; Kennedy, R. M.; Hackler, R. A.; Ferrandon, M.; Tennakoon, A.; Patnaik, S.; Lapointe, A. M.; Ammal, S. C.; Heyden, A.; Perras, F. A.; Pruski, M.; Scott, S. L.; Poeppelmeier, K. R.; Sadow, A. D.; Delferro, M. Upcycling Single-Use Polyethylene into High-Quality Liquid Products. *ACS Cent. Sci.* **2019**, *5* (11), 1795–1803. https://doi.org/10.1021/acscentsci.9b00722.

(62) Singh, M. V.; Kumar, S.; Sarker, M. Waste HD-PE Plastic, Deformation into Liquid Hydrocarbon Fuel Using Pyrolysis-Catalytic Cracking with a CuCO 3 Catalyst. *Sustain. Energy Fuels* **2018**, *2* (5), 1057–1068. https://doi.org/10.1039/c8se00040a.

(63) Onn, T. M.; Küngas, R.; Fornasiero, P.; Huang, K.; Gorte, R. J. Atomic Layer Deposition on Porous Materials: Problems with Conventional Approaches to Catalyst and Fuel Cell Electrode Preparation. *Inorganics* **2018**, *6* (1), 34. https://doi.org/10.3390/inorganics6010034.

(64) Zhang, L.; Prosser, J. H.; Feng, G.; Lee, D. Mechanical Properties of Atomic Layer Deposition-Reinforced Nanoparticle Thin Films. *Nanoscale* **2012**, *4* (20), 6543–6552. https://doi.org/10.1039/c2nr32016a.

(65) Dafinone, M. I.; Feng, G.; Brugarolas, T.; Tettey, K. E.; Lee, D.; I. Dafinone, M.; Feng, G.; Brugarolas, T.; E. Tettey, K.; Lee, D. Mechanical Reinforcement of Nanoparticle Thin Films Using Atomic Layer Deposition. *ACS Nano* **2011**, *5* (6), 5078–5087. https://doi.org/10.1021/nn201167j.

(66) Onn, T. M.; Zhang, S.; Arroyo-Ramirez, L.; Chung, Y. C.; Graham, G. W.; Pan, X.; Gorte, R. J. Improved Thermal Stability and Methane-Oxidation Activity of Pd/Al2O3 Catalysts by Atomic Layer Deposition of ZrO2. *ACS Catal.* **2015**, *5* (10), 5696–5701. https://doi.org/10.1021/acscatal.5b01348.

(67) Wang, C.; Mao, X.; Lee, J. D.; Onn, T. M.; Yeh, Y.-H. H.; Murray, C. B.; Gorte, R. J. A Characterization Study of Reactive Sites in Ald-Synthesized Wox/Zro2 Catalysts. *Catalysts* **2018**, *8* (7), 292. https://doi.org/10.3390/catal8070292.

(68) Huang, R.; Kwon, O.; Lin, C.; Gorte, R. J. The Effects of SMSI on M-Cresol Hydrodeoxygenation over Pt/Nb2O5 and Pt/TiO2. *J. Catal.* **2021**, *398*, 102–108. https://doi.org/https://doi.org/10.1016/j.jcat.2021.04.012.

(69) Bryk, P.; Korczeniewski, E.; Szymański, G. S.; Kowalczyk, P.; Terpiłowski, K.; Terzyk, A. P. What Is the Value of Water Contact Angle on Silicon? *Materials (Basel).* **2020**, *13* (7), 1554. https://doi.org/10.3390/ma13071554.

(70) Spencer, R. S.; Dillon, R. E. The Viscous Flow of Molten Polystyrene. II. *J. Colloid Sci.* **1949**, *4* (3), 241–255. https://doi.org/10.1016/0095-8522(49)90007-0.

(71) Owens, D. K.; Wendt, R. C. Estimation of the Surface Free Energy of Polymers. *J. Appl. Polym. Sci.* **1969**, *13* (8), 1741–1747. https://doi.org/https://doi.org/10.1002/app.1969.070130815.

(72) Xia, Z.; Rozyyev, V.; U. Mane, A.; W. Elam, J.; B. Darling, S.; Mane, A. U.; Elam, J. W.;

Darling, S. B. Surface Zeta Potential of ALD-Grown Metal-Oxide Films. *Langmuir* **2021**, *37* (39), 11618–11624. https://doi.org/10.1021/acs.langmuir.1c02028.

(73) Lin, C.; Jang, J. B.; Zhang, L.; Stach, E. A.; Gorte, R. J. Improved Coking Resistance of "Intelligent" Ni Catalysts Prepared by Atomic Layer Deposition. *ACS Catal.* **2018**, *8* (8), 7679–7687. https://doi.org/10.1021/acscatal.8b01598.

(74) Fernández, V.; Khayet, M.; Fernandez, V.; Khayet, M. Evaluation of the Surface Free Energy of Plant Surfaces: Toward Standardizing the Procedure. *Front. Plant Sci.* **2015**, *6* (JULY), 510. https://doi.org/10.3389/fpls.2015.00510.

(75) Cao, T.; Kwon, O.; Lin, C.; Vohs, J. M.; Gorte, R. J. Two-Dimensional Perovskite Crystals Formed by Atomic Layer Deposition of CaTiO3 on γ-Al2O3. *Nanomaterials* **2021**, *11* (9), 2207. https://doi.org/10.1149/1.3485240.

(76) Gardner, W. Note on the Dynamics of Capillary Flow. *Phys. Rev.* **1921**, *18* (3), 206–209. https://doi.org/10.1103/PhysRev.18.206.

(77) Dimitrov, D. I.; Milchev, A.; Binder, K. Molecular Dynamics Simulations of Capillary Rise Experiments in Nanotubes Coated with Polymer Brushes. *Langmuir* **2008**, *24* (4), 1232–1239. https://doi.org/10.1021/la7019445.

(78) Wang, H.; Hor, J. L.; Zhang, Y.; Liu, T.; Lee, D.; Fakhraai, Z. Dramatic Increase in Polymer Glass Transition Temperature under Extreme Nanoconfinement in Weakly Interacting Nanoparticle Films. *ACS Nano* **2018**, *12* (6), 5580–5587.

https://doi.org/10.1021/acsnano.8b01341.

(79) Fries, N.; Dreyer, M. An Analytic Solution of Capillary Rise Restrained by Gravity. *J. Colloid Interface Sci.* **2008**, *320* (1), 259–263. https://doi.org/10.1016/j.jcis.2008.01.009.

(80) Masoodi, R.; Pillai, K. M.; Varanasi, P. P. Darcy's Law-Based Models for Liquid Absorption in Polymer Wicks. *AIChE J.* **2007**, *53* (11), 2769–2782. https://doi.org/10.1002/aic.11322.

(81) Dee, G. T.; Sauer, B. B. The Molecular Weight and Temperature Dependence of Polymer Surface Tension: Comparison of Experiment with Interface Gradient Theory. *J. Colloid Interface Sci.* **1992**, *152* (1), 85–103. https://doi.org/10.1016/0021-9797(92)90010-J.

(82) Kim, H.; Lim, J. H.; Lee, K.; Choi, S. Q. Direct Measurement of Contact Angle Change in Capillary Rise. *Langmuir* **2020**, *36* (48), 14597–14606. https://doi.org/10.1021/acs.langmuir.0c02372.

(83) Srinivasan, S.; Datye, A. K.; Hampden-Smith, M.; Wachs, I. E.; Deo, G.; Jehng, J. M.; Turek, A. M.; Peden, C. H. F. The Formation of Titanium Oxide Monolayer Coatings on Silica Surfaces. *J. Catal.* **1991**, *131* (1), 260–275. https://doi.org/10.1016/0021-9517(91)90343-3.

(84) Zhuiykov, S.; Hai, Z.; Xu, H.; Xue, C. Development of Single Layer of WO3 on Large Spatial Resolution by Atomic Layer Deposition Technique. *19th Int. Conf. Opt. Mater. Adv. Nanomater.* **2017**, *19* (1), 784–787.

(85) National Institute of Standards and Technology. *Igor Levin (2018), NIST Inorganic Crystal Structure Database (ICSD)*. https://doi.org/10.18434/M32147.

(86) Fowkes, F. M.; Riddle, F. L.; Pastore, W. E.; Weber, A. A. Interfacial Interactions between Self-Associated Polar Liquids and Squalane Used to Test Equations for Solid-Liquid Interfacial Interactions. *Colloids and Surfaces* **1990**, *43* (2), 367–387. https://doi.org/10.1016/0166-6622(90)80298-I.

(87) Talik, A.; Tarnacka, M.; Grudzka-Flak, I.; Maksym, P.; Geppert-Rybczynska, M.; Wolnica, K.; Kaminska, E.; Kaminski, K.; Paluch, M. The Role of Interfacial Energy and Specific Interactions on the Behavior of Poly(Propylene Glycol) Derivatives under 2D Confinement. *Macromolecules* **2018**, *51* (13), 4840–4852. https://doi.org/10.1021/acs.macromol.8b00658.

(88) Fowkes, F. M. Attractive Forces At Interfaces. *Ind. Eng. Chem.* **1964**, *56* (12), 40–52. https://doi.org/10.1021/ie50660a008.

(89) KINGERY, W. D. Surface Tension of Some Liquid Oxides and Their Temperature Coefficients. *J. Am. Ceram. Soc.* **1959**, *42* (1), 6–10. https://doi.org/10.1111/j.1151-2916.1959.tb09134.x.

(90) Bockstaller, M. R.; Thomas, E. L.; R. Bockstaller, M.; L. Thomas, E.; Bockstaller, M. R.; Thomas, E. L. Optical Properties of Polymer-Based Photonic Nanocomposite Materials. *J. Phys. Chem. B* **2003**, *107* (37), 10017–10024. https://doi.org/10.1021/jp035286j.

(91) Cai, W.; Xiao, C.; Qian, L.; Cui, S. Detecting van Der Waals Forces between a Single Polymer Repeating Unit and a Solid Surface in High Vacuum. *Nano Res.* **2019**, *12* (1), 57–61. https://doi.org/10.1007/s12274-018-2176-8.

(92) Tirrell, M. Measurement of Interfacial Energy at Solid Polymer Surfaces. *Langmuir* **1996**, *12* (19), 4548–4551. https://doi.org/10.1021/la950894e.

(93) Huang, R.; Chang, J.; Choi, H.; Vohs, J. M.; Gorte, R. J. Furfural Upgrading by Aldol Condensation with Ketones over Solid-Base Catalysts. *Catal. Letters* **2022**, *152* (12), 3833–3842. https://doi.org/10.1007/s10562-022-03960-1.

(94) Starkweather, H. W. The Surface Tension of Polyethylene. *Polym. Eng. Sci.* **1965**, *5* (1), 5–6. https://doi.org/10.1002/pen.760050102.

(95) Stöber, W.; Fink, A.; Bohn, E. Controlled Growth of Monodisperse Silica Spheres in the Micron Size Range. *J. Colloid Interface Sci.* **1968**, *26* (1), 62–69. https://doi.org/10.1016/0021-9797(68)90272-5.

(96) McBride, S. P.; Law, B. M. Influence of Line Tension on Spherical Colloidal Particles at Liquid-Vapor Interfaces. *Phys. Rev. Lett.* **2012**, *109* (19), 196101. https://doi.org/10.1103/PhysRevLett.109.196101.

(97) Pagán-Torres, Y. J.; Gallo, J. M. R.; Wang, D.; Pham, H. N.; Libera, J. A.; Marshall, C. L.; Elam, J. W.; Datye, A. K.; Dumesic, J. A. Synthesis of Highly Ordered Hydrothermally Stable Mesoporous Niobia Catalysts by Atomic Layer Deposition. *ACS*

Catal. **2011**, *1* (10), 1234–1245. https://doi.org/10.1021/cs200367t.

(98) Wang, C. Y.; Kwon, O.; Gorte, R. J.; Vohs, J. M. Synthesis of High-Surface Area Tungstated Zirconia by Atomic Layer Deposition on Mesoporous Silica. *Microporous Mesoporous Mater.* **2022**, *335*, 111821. https://doi.org/10.1016/j.micromeso.2022.111821.

(99) Yeh, Y. H.; Gorte, R. J.; Rangarajan, S.; Mavrikakis, M. Adsorption of Small Alkanes on ZSM-5 Zeolites: Influence of Brønsted Sites. *J. Phys. Chem. C* **2016**, *120* (22), 12132–12138. https://doi.org/10.1021/acs.jpcc.6b03855.

(100) Yu, J.; Luo, J.; Zhang, Y.; Cao, J.; Chang, C. C.; Gorte, R. J.; Fan, W. An Examination of Alkali-Exchanged BEA Zeolites as Possible Lewis-Acid Catalysts. *Microporous Mesoporous Mater.* **2016**, *225*, 472–481. https://doi.org/10.1016/j.micromeso.2016.01.039.

(101) Savitz, S.; Siperstein, F.; Gorte, R. J.; Myers, A. L. Calorimetric Study of Adsorption of Alkanes in High-Silica Zeolites. *J. Phys. Chem. B* **1998**, *102* (35), 6865–6872. https://doi.org/10.1021/jp981836f.

(102) Kremer, K.; Grest, G. S. S. Dynamics of Entangled Linear Polymer Melts: A Molecular-Dynamics Simulation. *J. Chem. Phys.* **1990**, *92* (8), 5057–5086. https://doi.org/10.1063/1.458541.

(103) Plimpton, S. Fast Parallel Algorithms for Short-Range Molecular Dynamics. *J. Comput. Phys.* **1995**, *117* (1), 1–19. https://doi.org/10.1006/jcph.1995.1039.

(104) Gloor, G. J.; Jackson, G.; Blas, F. J.; De Miguel, E. Test-Area Simulation Method for the Direct Determination of the Interfacial Tension of Systems with Continuous or Discontinuous Potentials. *J. Chem. Phys.* **2005**, *123* (13), 134703. https://doi.org/10.1063/1.2038827.

(105) Biscay, F.; Ghoufi, A.; Lachet, V.; Malfreyt, P. Calculation of the Surface Tension of Cyclic and Aromatic Hydrocarbons from Monte Carlo Simulations Using an Anisotropic United Atom Model (AUA). *Phys. Chem. Chem. Phys.* **2009**, *11* (29), 6132–6147. https://doi.org/10.1039/b823295d.

(106) Comas-Vives, A. Amorphous SiO2 Surface Models: Energetics of the Dehydroxylation Process, Strain, Ab Initio Atomistic Thermodynamics and IR Spectroscopic Signatures. *Phys. Chem. Chem. Phys.* **2016**, *18* (10), 7475–7482. https://doi.org/10.1039/c6cp00602g.

(107) Floryan, L.; Borosy, A. P.; Núñez-Zarur, F.; Comas-Vives, A.; Copéret, C. Strain Effect and Dual Initiation Pathway in CrIII/SiO2polymerization Catalysts from Amorphous Periodic Models. *J. Catal.* **2017**, *346*, 50–56. https://doi.org/10.1016/j.jcat.2016.11.037.

(108) Xu, Y.; Libretto, N. J.; Zhang, G.; Miller, J. T.; Greeley, J. First-Principles Analysis of Ethylene Oligomerization on Single-Site Ga3+Catalysts Supported on Amorphous Silica. *ACS Catal.* **2022**, *12* (9), 5416–5424. https://doi.org/10.1021/acscatal.1c05936.

(109) LiBretto, N. J.; Xu, Y.; Quigley, A.; Edwards, E.; Nargund, R.; Vega-Vila, J. C.; Caulkins, R.; Saxena, A.; Gounder, R.; Greeley, J.; Zhang, G.; Miller, J. T. Olefin

Oligomerization by Main Group Ga3+ and Zn2+ Single Site Catalysts on SiO2. *Nat. Commun.* **2021**, *12* (1), 1–9. https://doi.org/10.1038/s41467-021-22512-6.

(110) Kresse, G.; Furthmüller, J. Efficient Iterative Schemes for Ab Initio Total-Energy Calculations Using a Plane-Wave Basis Set. *Phys. Rev. B - Condens. Matter Mater. Phys.* **1996**, *54* (16), 11169–11186. https://doi.org/10.1103/PhysRevB.54.11169.

(111) Kresse, G.; Furthmüller, J. Efficiency of Ab-Initio Total Energy Calculations for Metals and Semiconductors Using a Plane-Wave Basis Set. *Comput. Mater. Sci.* **1996**, *6* (1), 15–50. https://doi.org/10.1016/0927-0256(96)00008-0.

(112) Kresse, G.; Hafner, J. Ab Initio Molecular Dynamics for Liquid Metals. *Phys. Rev. B* **1993**, *47* (1), 558–561. https://doi.org/10.1103/PhysRevB.47.558.

(113) Kresse, G.; Hafner, J. Ab Initio Molecular-Dynamics Simulation of the Liquid-Metalamorphous- Semiconductor Transition in Germanium. *Phys. Rev. B* **1994**, *49* (20), 14251–14269. https://doi.org/10.1103/PhysRevB.49.14251.

(114) Wellendorff, J.; Lundgaard, K. T.; Møgelhøj, A.; Petzold, V.; Landis, D. D.; Nørskov, J. K.; Bligaard, T.; Jacobsen, K. W. Density Functionals for Surface Science: Exchange-Correlation Model Development with Bayesian Error Estimation. *Phys. Rev. B - Condens. Matter Mater. Phys.* **2012**, *85* (23), 235149. https://doi.org/10.1103/PhysRevB.85.235149.

(115) Blöchl, P. E. Projector Augmented-Wave Method. *Phys. Rev. B* **1994**, *50* (24), 17953–17979. https://doi.org/10.1103/PhysRevB.50.17953.

(116) Joubert, D. From Ultrasoft Pseudopotentials to the Projector Augmented-Wave Method. *Phys. Rev. B - Condens. Matter Mater. Phys.* **1999**, *59* (3), 1758–1775. https://doi.org/10.1103/PhysRevB.59.1758.

(117) Igor Levin. *NIST Inorganic Crystal Structure Database (ICSD)*. National Institute of Standards and Technology. https://doi.org/https://doi.org/10.18434/M32147.

(118) Seitz, O.; Fernandes, P. G.; Tian, R.; Karnik, N.; Wen, H. C.; Stiegler, H.; Chapman, R. A.; Vogel, E. M.; Chabal, Y. J. Control and Stability of Self-Assembled Monolayers under Biosensing Conditions. *J. Mater. Chem.* **2011**, *21* (12), 4384–4392. https://doi.org/10.1039/c1jm10132c.

(119) Ke, W.; Liu, Y.; Wang, X.; Qin, X.; Chen, L.; Palomino, R. M.; Simonovis, J. P.; Lee, I.; Waluyo, I.; Rodriguez, J. A.; Frenkel, A. I.; Liu, P.; Zaera, F. Nucleation and Initial Stages of Growth during the Atomic Layer Deposition of Titanium Oxide on Mesoporous Silica. *Nano Lett.* **2020**, *20* (9), 6884–6890. https://doi.org/10.1021/acs.nanolett.0c02990.

(120) Gorte, R. J.; White, D. Measuring Sorption Effects at Zeolite Acid Sites: Pursuing Ideas from W.O. Haag. *Microporous Mesoporous Mater.* **2000**, *35–36*, 447–455. https://doi.org/10.1016/S1387-1811(99)00241-3.

(121) Zhang, Y.; Yu, J. Y.; Yeh, Y. H.; Gorte, R. J.; Rangarajan, S.; Mavrikakis, M. An Adsorption Study of CH4 on ZSM-5, MOR, and ZSM-12 Zeolites. *J. Phys. Chem. C* **2015**, *119* (52), 28970–28978. https://doi.org/10.1021/acs.jpcc.5b09571.

(122) Kremer, K.; Grest, G. S. Dynamics of Entangled Linear Polymer Melts: A Molecular-dynamics Simulation. *J. Chem. Phys.* **1990**, *92* (8), 5057–5086. https://doi.org/10.1063/1.458541.

(123) Galliero, G. Surface Tension of Short Flexible Lennard-Jones Chains: Corresponding States Behavior. *J. Chem. Phys.* **2010**, *133* (7), 074705. https://doi.org/10.1063/1.3469860.

(124) Blas, F. J.; Bravo, A. I. M. V.; Algaba, J.; Martínez-Ruiz, F. J.; Macdowell, L. G. Effect of Molecular Flexibility of Lennard-Jones Chains on Vapor-Liquid Interfacial Properties. *J. Chem. Phys.* **2014**, *140* (11), 114705. https://doi.org/10.1063/1.4868100.

(125) Bin Jumah, A.; Malekshahian, M.; Tedstone, A. A.; Garforth, A. A. Kinetic Modeling of Hydrocracking of Low-Density Polyethylene in a Batch Reactor. *ACS Sustain. Chem. Eng.* **2021**, *9* (49), 16757–16769. https://doi.org/10.1021/acssuschemeng.1c06231.

(126) Kang, Q.; Chu, M.; Xu, P.; Wang, X.; Wang, S.; Cao, M.; Ivasenko, O.; Sham, T.-K.; Zhang, Q.; Sun, Q.; Chen, J. Entropy Confinement Promotes Hydrogenolysis Activity for Polyethylene Upcycling. *Angew. Chemie Int. Ed.* **2023**, *n/a* (n/a), e202313174. https://doi.org/https://doi.org/10.1002/anie.202313174.

(127) Kim, B. Q.; Füredi, M.; Venkatesh, R. B.; Guldin, S.; Lee, D. Water-Induced Separation of Polymers from High Nanoparticle-Content Nanocomposite Films. *Small* **2023**, *2302676*, 1–8. https://doi.org/10.1002/smll.202302676.

(128) Tu, C. H.; Steinhart, M.; Berger, R.; Kappl, M.; Butt, H. J.; Floudas, G. When Crystals Flow. *Sci. Adv.* **2023**, *9* (19), eadg8865. https://doi.org/10.1126/sciadv.adg8865.

(129) Kimmich, R.; Fatkullin, N.; Mattea, C.; Fischer, E. Polymer Chain Dynamics under Nanoscopic Confinements. *Magn. Reson. Imaging* **2005**, *23* (2 SPEC. IS), 191–196. https://doi.org/10.1016/j.mri.2004.11.050.

(130) Tung, W. S.; Composto, R. J.; Riggleman, R. A.; Winey, K. I. Local Polymer Dynamics and Diffusion in Cylindrical Nanoconfinement. *Macromolecules* **2015**, *48* (7), 2324–2332. https://doi.org/10.1021/acs.macromol.5b00085.

(131) Zax, D. B.; Yang, D. K.; Santos, R. A.; Hegemann, H.; Giannelis, E. P.; Manias, E. Dynamical Heterogeneity in Nanoconfined Poly(Styrene) Chains. *J. Chem. Phys.* **2000**, *112* (6), 2945–2951. https://doi.org/10.1063/1.480867.

(132) Lange, F.; Judeinstein, P.; Franz, C.; Hartmann-Azanza, B.; Ok, S.; Steinhart, M.; Saalwächter, K. Large-Scale Diffusion of Entangled Polymers along Nanochannels. *ACS Macro Lett.* **2015**, *4* (5), 561–565. https://doi.org/10.1021/acsmacrolett.5b00213.

(133) Lin, E. K.; Kolb, R.; Satija, S. K.; Wu, W. L. Reduced Polymer Mobility near the Polymer/Solid Interface as Measured by Neutron Reflectivity. *Macromolecules* **1999**, *32* (11), 3753–3757. https://doi.org/10.1021/ma9814604.

(134) Gam, S.; Meth, J. S.; Zane, S. G.; Chi, C.; Wood, B. A.; Seitz, M. E.; Winey, K. I.; Clarke, N.; Composto, R. J. Macromolecular Diffusion in a Crowded Polymer

Nanocomposite. *Macromolecules* **2011**, *44* (9), 3494–3501. https://doi.org/10.1021/ma102463q.

(135) Lin, C.-C.; Gam, S.; Meth, J. S.; Clarke, N.; Winey, K. I.; Composto, R. J. Do Attractive Polymer-Nanoparticle Interactions Retard Polymer Diffusion in Nanocomposites? *Macromolecules* **2013**, *46* (11), 4502–4509. https://doi.org/10.1021/ma4000557.

(136) Jin, S.; McKenna, G. B. Effect of Nanoconfinement on Polymer Chain Dynamics. *Macromolecules* **2020**, *53* (22), 10212–10216. https://doi.org/10.1021/acs.macromol.0c00365.

(137) Tian, F.; Zhang, S.; Zhai, M.; Sui, J.; Lan, X.; Gao, J. Thermal Properties of Nano-Sized Polyethylene Glycol Confined in Silica Gels for Latent Heat Storage. *Thermochim. Acta* **2017**, *655* (November 2016), 211–218. https://doi.org/10.1016/j.tca.2017.05.006.

(138) Tu, C.-H.; Steinhart, M.; Butt, H.-J.; Floudas, G. In Situ Monitoring of the Imbibition of Poly(n-Butyl Methacrylates) in Nanoporous Alumina by Dielectric Spectroscopy. *Macromolecules* **2019**, *52* (21), 8167–8176. https://doi.org/10.1021/acs.macromol.9b01383.

(139) Roozbahani, M. M.; Borela, R.; Frost, J. D. Pore Size Distribution in Granular Material Microstructure. *Materials (Basel).* **2017**, *10* (11), 1–21. https://doi.org/10.3390/ma10111237.

(140) Pertoft, H.; Laurent, T. C.; Låås, T.; Kågedal, L. Density Gradients Prepared from

Colloidal Silica Particles Coated by Polyvinylpyrrolidone (Percoll). *Anal. Biochem.* **1978**, *88* (1), 271–282. https://doi.org/10.1016/0003-2697(78)90419-0.

(141) Hinton, Z. R.; Kots, P. A.; Soukaseum, M.; Vance, B. C.; Vlachos, D. G.; Epps, T. H.; Korley, L. S. T. J. Antioxidant-Induced Transformations of a Metal-Acid Hydrocracking Catalyst in the Deconstruction of Polyethylene Waste. *Green Chem.* **2022**, *24* (19), 7332–7339. https://doi.org/10.1039/d2gc02503e.

(142) Yao, Y.; Alexandris, S.; Henrich, F.; Auernhammer, G.; Steinhart, M.; Butt, H.-J.; Floudas, G. Complex Dynamics of Capillary Imbibition of Poly(Ethylene Oxide) Melts in Nanoporous Alumina. *J. Chem. Phys.* **2017**, *146* (20), 203320. https://doi.org/10.1063/1.4978298.

(143) Lyu, X.; Meirow, M.; Wu, X.; Zhou, X.; Liu, Y.; Huang, W.; Li, T.; Lee, B. Molecular-Weight-Dependent Infiltration and Adsorption of Polymers into Nanochannels. *ACS Appl. Mater. Interfaces* **2023**, *15* (22), 27369–27379. https://doi.org/10.1021/acsami.3c04152.

(144) Brochard, F.; de Gennes, P. G. Dynamics of Confined Polymer Chains. *P.G. Gennes' Impact Sci. Soft Matter Biophys.* **2009**, *2* (1977), 96–100. https://doi.org/10.1142/9789814280648_0009.

(145) Dai, L.; Doyle, P. S. Comparisons of a Polymer in Confinement versus Applied Force. *Macromolecules* **2013**, *46* (15), 6336–6344. https://doi.org/10.1021/ma400674q.

(146) Johner, A.; Shin, K.; Obukhov, S. Nanofluidity of a Polymer Melt: Breakdown of

Poiseuille's Flow Model. *EPL (Europhysics Lett.* **2010**, *91* (3), 38002. https://doi.org/10.1209/0295-5075/91/38002.

(147) Shin, K.; Woo, E.; Jeong, Y. G.; Kim, C.; Huh, J.; Kim, K. W. Crystalline Structures, Melting, and Crystallization of Linear Polyethylene in Cylindrical Nanopores. *Macromolecules* **2007**, *40* (18), 6617–6623. https://doi.org/10.1021/ma070994e.

(148) Mandelkern, L. A Re-Examination of the Relation between the Melting Temperature and the Crystallization Temperature: Linear Polyethylene. *Macromolecules* **1995**, *28*, 3205–3213.

(149) Michell, R. M.; Müller, A. J. Confined Crystallization of Polymeric Materials. *Prog. Polym. Sci.* **2016**, *54–55*, 183–213. https://doi.org/10.1016/j.progpolymsci.2015.10.007.

(150) Kim, J. H.; Jang, J.; Zin, W. C. Thickness Dependence of the Melting Temperature of Thin Polymer Films. *Macromol. Rapid Commun.* **2001**, *22* (6), 386–389. https://doi.org/10.1002/1521-3927(20010301)22:6<386::AID-MARC386>3.0.CO;2-S.

(151) Michell, R. M.; Blaszczyk-Lezak, I.; Mijangos, C.; Müller, A. J. Confined Crystallization of Polymers within Anodic Aluminum Oxide Templates. *J. Polym. Sci. Part B Polym. Phys.* **2014**, *52* (18), 1179–1194. https://doi.org/10.1002/polb.23553.

(152) Wang, Y.; Rafailovich, M.; Sokolov, J.; Gersappe, D.; Araki, T.; Zou, Y.; Kilcoyne, A. D. L.; Ade, H.; Marom, G.; Lustiger, A. Substrate Effect on the Melting Temperature of Thin Polyethylene Films. *Phys. Rev. Lett.* **2006**, *96* (2), 1–4.

https://doi.org/10.1103/PhysRevLett.96.028303.

(153) Mandelkern, L.; Alamo, R. G.; Kennedy, M. A. Interphase Thickness of Linear Polyethylene. *Macromolecules*. 1990, pp 4721–4723. https://doi.org/10.1021/ma00223a034.

(154) Ming, Y.; Zhou, Z.; Hao, T.; Nie, Y. Molecular Simulation of Polymer Crystallization under Chain and Space Confinement. *Phys. Chem. Chem. Phys.* **2021**, *23* (32), 17382–17391. https://doi.org/10.1039/d1cp01799c.

(155) Tashiro, K.; Yamamoto, H. Structural Evolution Mechanism of Crystalline Polymers in the Isothermal Melt-Crystallization Process: A Proposition Based on Simultaneous WAXD/SAXS/FTIR Measurements. *Polymers*. 2019. https://doi.org/10.3390/polym11081316.

(156) Schmidt, A. G. *XRD Investigation of Three Types of Polyethylene Films with ARL EQUINOX 100 X-Ray Diffractometer*; 2017.

(157) Kappert, E. J.; Raaijmakers, M. J. T.; Ogieglo, W.; Nijmeijer, A.; Huiskes, C.; Benes, N. E. Temperature Calibration Procedure for Thin Film Substrates for Thermo-Ellipsometric Analysis Using Melting Point Standards. *Thermochim. Acta* **2015**, *601*, 29–32. https://doi.org/10.1016/j.tca.2014.12.017.

(158) Carvalho, J. L.; Massa, M. V.; Dalnoki-Veress, K. Ellipsometry as a Probe of Crystallization Kinetics in Thin Diblock Copolymer Films. *J. Polym. Sci. Part B Polym.*

Phys. **2006**, *44* (24), 3448–3452. https://doi.org/10.1002/polb.21006.

(159) Haider, T.; Suraeva, O.; O'Duill, M. L.; Mars, J.; Mezger, M.; Lieberwirth, I.; Wurm, F. R. Controlling the Crystal Structure of Precisely Spaced Polyethylene-like Polyphosphoesters. *Polym. Chem.* **2020**, *11* (20), 3404–3415. https://doi.org/10.1039/d0py00272k.

(160) Henry, C. K.; Sandoz-Rosado, E.; Roenbeck, M. R.; Magagnosc, D. J.; Palmese, G. R.; Strawhecker, K. E.; Alvarez, N. J. Direct Measure of Crystalline Domain Size, Distribution, and Orientation in Polyethylene Fibers. *Polymer (Guildf).* **2020**, *202*, 122589. https://doi.org/10.1016/J.POLYMER.2020.122589.

(161) Sasaki, S.; Masunaga, H.; Tajiri, H.; Inoue, K.; Okuda, H.; Noma, H.; Honda, K.; Takahara, A.; Takata, M. In Situ Investigation of Annealing Effect on Lamellar Stacking Structure of Polyethylene Thin Films by Synchrotron Grazing-Incidence Small-Angle and Wide-Angle X-Ray Scattering. *J. Appl. Crystallogr.* **2007**, *40* (SUPPL. 1), 642–644. https://doi.org/10.1107/S002188980700578X.

(162) Cheung, T. T. P.; Gerstein, B. C. 1H Nuclear Magnetic Resonance Studies of Domain Structures in Polymers. *J. Appl. Phys.* **1981**, *52* (9), 5517–5528. https://doi.org/10.1063/1.329534.

(163) Fontana, L.; Vinh, D. Q.; Santoro, M.; Scandolo, S.; Gorelli, F. A.; Bini, R.; Hanfland, M. High-Pressure Crystalline Polyethylene Studied by x-Ray Diffraction and Ab Initio

Simulations. *Phys. Rev. B - Condens. Matter Mater. Phys.* **2007**, *75* (17), 1–11. https://doi.org/10.1103/PHYSREVB.75.174112/FIGURES/9/MEDIUM.

(164) Men, Y.; Rieger, J.; Lindner, P.; Enderle, H. F.; Lilge, D.; Kristen, M. O.; Mihan, S.; Jiang, S. Confined Intra-Molecular Clustering in Orientated Polyethylene after Annealing. *Polymer (Guildf).* **2007**, *48* (9), 2464–2469. https://doi.org/10.1016/j.polymer.2007.02.039.

(165) Ge, J.; Peters, B. Mass Transfer in Catalytic Depolymerization: External Effectiveness Factors and Serendipitous Processivity in Stagnant and Stirred Melts. *Chem. Eng. J.* **2023**, *466*, 143251. https://doi.org/10.1016/j.cej.2023.143251.

(166) Jaydev, S. D.; Martín, A. J.; Pérez-Ramírez, J.; Pérez-Ramírez, J. Direct Conversion of Polypropylene into Liquid Hydrocarbons on Carbon-Supported Platinum Catalysts. *ChemSusChem* **2021**, *n/a* (n/a), 1–8. https://doi.org/10.1002/cssc.202101999.

(167) Ismael, M.; Sun, M.; Zhu, L.; Liu, W.; Zhao, X.; Zhang, Y.; Luo, H.; Miao, G.; Li, S.; Yin, S.; Kong, L. Efficient Upgrading of Polyolefin Plastics into C5–C12 Gasoline Alkanes over a Pt/W/Beta Catalyst. *Sustain. Energy Fuels* **2022**, *43* (24), 9596–9605. https://doi.org/10.1039/D1SE01778K.

(168) Jia, C.; Xie, S.; Zhang, W.; Intan, N. N.; Sampath, J.; Pfaendtner, J.; Lin, H. Deconstruction of High-Density Polyethylene into Liquid Hydrocarbon Fuels and Lubricants by Hydrogenolysis over Ru Catalyst. *Chem Catal.* **2021**, *1* (4), 1–19.

https://doi.org/10.1016/j.checat.2021.04.002.

(169) Zhang, F.; Zeng, M.; Yappert, R. D.; Sun, J.; Lee, Y. H.; LaPointe, A. M.; Peters, B.; Abu-Omar, M. M.; Scott, S. L. Polyethylene Upcycling to Long-Chain Alkylaromatics by Tandem Hydrogenolysis/Aromatization. *Science (80-.).* **2020**, *370* (6515), 437–441. https://doi.org/10.1126/science.abc5441.

(170) Ellis, L. D.; Orski, S. V.; Kenlaw, G. A.; Norman, A. G.; Beers, K. L.; Román-Leshkov, Y.; Beckham, G. T. Tandem Heterogeneous Catalysis for Polyethylene Depolymerization via an Olefin-Intermediate Process. *ACS Sustain. Chem. Eng.* **2021**, *9* (2), 623–628. https://doi.org/10.1021/acssuschemeng.0c07612.

(171) Lee, S.; Shen, K.; Wang, C. Y.; Vohs, J. M.; Gorte, R. J. Hydrogenolysis of N-Eicosane over Ru-Based Catalysts in a Continuous Flow Reactor. *Chem. Eng. J.* **2023**, *456* (October 2022), 141030. https://doi.org/10.1016/j.cej.2022.141030.

(172) Chen, Z.; Xu, L.; Zhang, X. Upgrading of Polyethylene to Hydrocarbon Fuels over the Fe-Modified Pt/Al2O3 Catalysts at a Mild Condition without External H2. *Chem. Eng. J.* **2022**, *446* (P2), 136213. https://doi.org/10.1016/j.cej.2022.136213.

(173) Efimchenko, V. S.; Fedotov, V. K.; Kuzovnikov, M. A.; Zhuravlev, A. S.; Bulychev, B. M. Hydrogen Solubility in Amorphous Silica at Pressures up to 75 Kbar. *J. Phys. Chem. B* **2013**, *117* (1), 422–425. https://doi.org/10.1021/jp309991x.

(174) Deas, T. M.; Hofer, H. H.; Dole, M. Solubility of Hydrogen in Polyethylene by a

Semimicro Method. *Macromolecules* **1972**, *5* (2), 223–226. https://doi.org/10.1021/ma60026a023.

(175) Matteucci, S.; Kusuma, V. A.; Swinnea, S.; Freeman, B. D. Gas Permeability, Solubility and Diffusivity in 1,2-Polybutadiene Containing Brookite Nanoparticles. *Polymer (Guildf).* **2008**, *49* (3), 757–773. https://doi.org/10.1016/j.polymer.2007.12.011.

(176) Aoki, Y.; Hashizume, M.; Onoue, S.; Kunitake, T. Determination of Surface Area and Porosity of Small, Nanometer-Thick Films by Quartz Crystal Microbalance Measurement of Gas Adsorption. *J. Phys. Chem. B* **2008**, *112* (46), 14578–14582. https://doi.org/10.1021/jp801919h.

(177) Mieczkowski, R. The Determination of the Solubility Parameter Components of Polystyrene. *Eur. Polym. J.* **1989**, *25* (10), 1055–1057. https://doi.org/10.1016/0014-3057(89)90136-5.

(178) Mieczkowski, R. The Determination of the Solubility Parameter Components of Polystyrene by Partial Specific Volume Measurements. *Eur. Polym. J.* **1988**, *24* (12), 1185–1189. https://doi.org/10.1016/0014-3057(88)90109-7.

(179) Manginell, R. P.; Moorman, M. W.; Anderson, J. M.; Burns, G. R.; Achyuthan, K. E.; Wheeler, D. R.; Schwindt, P. D. D. In Situ Dissolution or Deposition of Ytterbium (Yb) Metal in Microhotplate Wells for a Miniaturized Atomic Clock. *Opt. Express* **2012**, *20* (22), 24650. https://doi.org/10.1364/oe.20.024650.

(180) Sakti, S. P.; Masruroh; Istiroyah; Kamasi, D. D.; Zafirah, T. N. Ultra Thick Polystyrene Coating on Quartz Crystal Microbalance Sensor. In *Materials Today: Proceedings*; Elsevier, 2020; Vol. 44, pp 3217–3220. https://doi.org/10.1016/j.matpr.2020.11.441.

(181) Daiko, Y.; Iwamoto, Y. Hydrogen Adsorption and Electronic Structural Calculation of a Polymer-Derived SiCH Membrane with a Unique Affinity for Molecular Hydrogen. *J. Sol-Gel Sci. Technol.* **2022**, *104* (3), 449–455. https://doi.org/10.1007/s10971-022-05876-z.